INSTITUT FÜR PHYSIK

JOHANNES GUTENBERG–UNIVERSITÄT

MAINZ

Measurement of Z Boson Parameters at LEP

Günter Quast

Institut für Physik
Johannes Gutenberg-Universität
55099 Mainz, Germany

HABILITATIONSSCHRIFT
zur Erlangung der *venia legendi*

Mainz, im Januar 1998

Abstract

Recent results from the four experiments ALEPH, DELPHI, L3 and OPAL at the large electron-positron collider, LEP at CERN, are reviewed. Analyses from an integrated luminosity of about 150 pb^{-1} per experiment, taken at different centre-of-mass energies within ± 3 GeV around the peak of the Z resonance during the years 1989 to 1995, are available now. Repeated accurate calibrations of the energy scale of LEP lead to precise measurements of the mass and of the total width of the Z boson. Here, the main emphasis is put on the relevance of these measurements for precision tests of the Standard Model of the electroweak interaction.

Contents

1 Introduction

The history of our understanding of the weak interaction is closely linked to the study and discovery of the Z boson, mediating the weak neutral current. Virtual Z exchange was first realised in neutrino scattering experiments at the CERN proton synchrotron [1] in 1973, where muon neutrino reactions without muon production in the final state were correctly identified as weak neutral current interactions. The ratio of reactions with and without muons in the final state provided a measurement of the charged to neutral current ratio. In the gauge theory of the electroweak interaction, the "Standard Model" [2], this ratio depends on the mixing between the original gauge boson from a U(1) gauge symmetry ("B") and the neutral partner ("W^0") of the $W^\pm$ bosons, which result from a SU(2) gauge symmetry. The physical particles are the massless photon, γ, and the Z; these are given by

$$\begin{aligned} \gamma &= W^0 \sin\theta_W + B \cos\theta_W \\ Z &= W^0 \cos\theta_W - B \sin\theta_W , \end{aligned} \tag{1.1}$$

where θ_W is the weak mixing or "Weinberg" angle. The ratios of the masses of the weak gauge bosons and of the electromagnetic weak coupling constants, e and g, respectively, are also determined by the weak mixing angle:

$$\begin{aligned} \cos\theta_W &= m_W/m_Z \\ \sin\theta_W &= e/g . \end{aligned} \tag{1.2}$$

The weak coupling g is related to the muon decay or "Fermi" constant, G_F, by $G_F/\sqrt{2} = g^2/(8m_W^2)$.

Indirect evidence for the contribution of the Z boson in addition to the photon was seen in inelastic scattering of longitudinally polarised electrons from deuterium at the Stanford Linear Accelerator [3] and in e^+e^- annihilation processes in storage rings, PETRA at DESY [4] and PEP at Stanford [5]. Finally, the $W^\pm$ and Z bosons were discovered as real particles at the CERN Super-Proton-Synchrotron (SPS) [6] in 1983.

Dedicated accelerators to produce large amounts of Z bosons in a clean environment were planned and built and started operating in the late eighties: the Linear Collider at Stanford ("SLC") [7] and the Large Electron Positron collider ("LEP") at CERN [8]. These electron-positron colliders operated at centre-of-mass energies close to the Z resonance and provided precision measurements of its parameters, serving as important tests at the level of quantum corrections to tree level results calculated from electroweak theory.

LEP has provided a wealth of results since the first collisions were observed in 1989. By the end of 1995 the four general purpose detectors ALEPH, DELPHI, L3 and OPAL [9, 10, 11, 12] had recorded and analysed a total of almost 15 million Z decays into hadrons and about 1.6 million leptonic decays at centre-of-mass energies within ± 3 GeV around the peak of the Z resonance. A nearly complete set of results based on analyses of these data is now available.

The SLD detector at SLC complements the LEP measurements by studies of Z production with longitudinally polarised electron beams, thereby compensating the lower Z production rate at the SLC and allowing a precise determination of the weak mixing angle from Z couplings to electrons.

The properties of the Z boson were measured with high accuracy, and high precision tests of the Standard Model of the electroweak interaction were performed. The top quark manifests itself through virtual corrections to lowest-order values of the electroweak parameters, allowing its mass to be constrained from the precise measurements at LEP before its discovery at the Tevatron collider at Fermilab [13]. Direct searches for the as yet elusive Higgs boson, an indispensable part of the Standard Model, all proved negative. However, the electroweak precision data in combination with the value of the top quark mass allow to place an upper limit on its mass, provided nothing else is relevant at the energy scale around $\sim$100 GeV beyond the "minimal" version of the Standard Model, i. e. with only one Higgs boson. Hints at new physics via the production of new particles or unexpected decay modes of the Z have been searched for, all with negative results. The huge number of multihadronic decays also provides a testing ground for many aspects of Quantum-Chromo-Dynamics (QCD), the theory of the strong interaction.

This review highlights only a few of the many topics studied at LEP, with emphasis on precision tests of the electroweak theory. An introduction to the Standard Model and the aspects of it that can be tested at LEP is followed by a description of the LEP accelerator. Here, the precise determination of the centre-of-mass energy of the colliding particle beams in LEP is of special importance to the determination of Z resonance parameters. After a presentation of the four large experiments at LEP and of their most prominent features various electroweak observables accessible in experiments operating at a centre-of-mass energy corresponding to the Z mass will be discussed. This is followed by a description of the main experimental techniques used in the measurements and individual as well as combined results of the experiments are presented. Next, a the status of important input parameters to the Standard Model not obtainable from measurements around the Z resonance is briefly reviewed. The results obtained by the four LEP experiments are then combined with other precision electroweak measurements and set into perspective with predictions of the Standard Model. This provides insight into the level of consistency among all measurements and also begins to constrain the last missing parameter of the model, the mass of the Higgs boson.

2 Electroweak Theory

The Standard Model of particle physics describes the interactions between the basic constituents of matter. The particles comprise the three neutrinos ν_e, ν_μ and ν_τ, the charged leptons e, μ and τ, and the six quarks up (u), down (d), charm (c), strange (s), top (t) and bottom (b). The top quark is very heavy and has only recently been observed experimentally as a real particle. The interactions are mediated by spin-1 bosons, the photon for the electromagnetic, the $W^\pm$ and Z bosons for the weak and eight gluons for the strong interaction. Electromagnetic and weak interactions are described in the common framework of the "electroweak" interaction. This is based on the gauge symmetry $U(1)\times SU(2)_L$, where the index L indicates that only left-handed helicity states of fermions are grouped into doublets with respect to the SU(2) symmetry or the "weak iso-spin". In addition to vector bosons and fermions, a third kind of particle is required to make the electroweak theory mathematically consistent, the Higgs boson. Through the process of spontaneous SU(2) symmetry breaking three of the four degrees of freedom introduced via a SU(2) Higgs doublet provide mass terms to the weak bosons, and the remaining degree of freedom gives rise to a spin-0 Higgs boson as an observable particle of the theory. At least one Higgs doublet is needed in the minimal version of the theory, although a more complicated structure of the Higgs sector would also be possible. Yukawa couplings of the Higgs boson to fermions, different for each fermion species, are believed to give the fermions their masses. Strong interacting particles appear in three different charges, so-called "colours", obeying a $SU(3)_{\rm colour}$ symmetry, which leads to eight gauge bosons, the gluons.

The particle content of the minimal Standard Model is illustrated below:

left-handed fermions:

$$\begin{pmatrix} \nu_e \\ e \end{pmatrix}_L \quad \begin{pmatrix} \nu_\mu \\ \mu \end{pmatrix}_L \quad \begin{pmatrix} \nu_\tau \\ \tau \end{pmatrix}_L$$

$$\begin{pmatrix} u \\ d \end{pmatrix}_L \quad \begin{pmatrix} c \\ s \end{pmatrix}_L \quad \begin{pmatrix} t \\ b \end{pmatrix}_L \quad \left\{ \begin{array}{c} \text{in 3} \\ \text{colours} \end{array} \right.$$

right-handed fermions: *

$\nu_{e,R}(?)$, e_R, $\nu_{\mu,R}(?)$, μ_R , $\nu_{\tau,R}(?)$, τ_R

u_R, d_R, c_R, s_R, t_R, b_R in 3 colours

vector gauge bosons: $W^\pm$ Z γ

one Higgs boson: H

*Right-handed components of neutrinos exist if neutrinos are not massless.

Within the framework of the Standard Model observables can be calculated from a limited set of input parameters. These are the U(1), $SU(2)_L$ and $SU(3)_{\rm colour}$ coupling constants, g_1, g and α_s, the vacuum expectation value of the Higgs boson, $\langle v \rangle$, the Higgs boson mass, $m_{\rm H}$, and all fermion masses and mixing angles. Conveniently, g_1, g and $\langle v \rangle$ are replaced by a set of parameters which are related to the most precisely measured quantities, namely the coupling constant of the electromagnetic interaction, α, the muon decay constant, $G_{\rm F}$, and the weak mixing angle, $\sin\theta_{\rm W}$, or the mass of the Z boson, $m_{\rm Z}$. The most precise values at present are [14]:

$1/\alpha$	=	137.035 989 5(61)
$G_{\rm F}$	=	$1.166\,39(2)\cdot 10^{-5}$ GeV^{-2}
α_s	=	0.118(3)
fermion masses		
esp. $m_{\rm t}$	=	175.6±5.5 GeV [15]
$m_{\rm Z}$	=	91.187(7) GeV
$m_{\rm H}$		unknown

The masses of the weak gauge bosons, $W^\pm$ and Z, the weak mixing angle, $\theta_{\rm W}$, and the electromagnetic and weak coupling constants are related in lowest order perturbation theory by

$$\sin^2\theta_{\rm W}\cos^2\theta_{\rm W} = \frac{\pi\alpha}{\sqrt{2}G_{\rm F}}\frac{1}{\rho m_{\rm Z}^2}\,. \tag{2.1}$$

The Veltman parameter ρ, measuring the relative strength of neutral and charged current contributions, is determined by the Higgs structure; it is unity in lowest order in the Standard Model which contains Higgs doublets only.

Higher order corrections in perturbation theory modify the cross-sections predicted from tree level diagrams. Virtual particle loops modifying the propagator, vertex corrections and gluon radiation from final state or virtual quarks introduce a dependence of all predictions of the Standard Model on α_s, $m_{\rm H}$ and the fermion masses. Effects from the top quark mass, $m_{\rm t}$, are of dominant importance because of the large mass difference between the top quark and its weak iso-spin partner, the bottom quark.

The only parameter which is still experimentally unknown is $m_{\rm H}$.

Of primary interest at LEP are the genuine electroweak corrections, which probe the quantum structure of the electroweak theory and are as important as *e. g.* the g-2 experiments to Quantum-Electro-Dynamics, QED.

In order to confront theory with experiment, precision calculations including reliable estimates of uncertainties originating from neglected higher orders have to be performed. An enormous theoretical effort, during the preparations for LEP and accompanying its operation, was necessary to achieve this goal [16, 17].

2.1 Tree-level diagrams

The basic process at LEP I is fermion pair production via the creation of a Z boson with a small photon contribution, as shown in the Feynman diagram below.

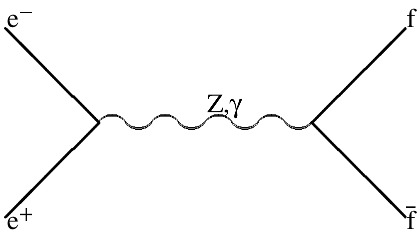

If the final state is e^+e^-, additional t-channel diagrams have to be taken into account. The t-channel contribution is dominated by single photon exchange between the incoming electrons and positrons, with a very large cross-section in the forward direction.

The Lagrangian for Z interactions with fermion pairs, $f\bar{f}$, is

$$\mathcal{L}_{Z\mathrm{f}\bar{\mathrm{f}}} = -\frac{ig}{2\cos\theta_W} Z_\mu \sum_f \bar{f}\gamma^\mu [g_v + g_a \gamma_5] f\,,$$

where g_v and g_a are the vector and axial-vector couplings of the Z to fermions.

These couplings depend on the weak isospin, I_3^f, and charges, Q^f, of the fermions, which are $(I_3^f, Q^f) = (+\frac{1}{2}, 0)$ for the neutrinos ν_e, ν_μ and ν_τ, $(-\frac{1}{2}, -1)$ for the charged leptons e, μ and τ, $(+\frac{1}{2}, +\frac{2}{3})$ for the up, charm and top quarks and $(-\frac{1}{2}, -\frac{1}{3})$ for the down, strange and bottom quarks. The couplings also depend on the weak mixing angle, $\sin\theta_W$, and the Veltman parameter, ρ, and are given by

$$\begin{aligned} g_v^f &= \sqrt{\rho}(I_3^f - 2Q^f \sin^2\theta_W) \\ g_a^f &= \sqrt{\rho} I_3^f\,. \end{aligned} \qquad (2.2)$$

This can also be expressed as separate couplings to the left-handed and right-handed helicity states. Written in terms of left-handed and right-handed couplings, with $g_l = (g_v + g_a)/2$ and $g_r = (g_v - g_a)/2$, the above relations become

$$\begin{aligned} g_l^f &= \sqrt{\rho}(I_3^f - Q^f \sin^2\theta_W) \\ g_r^f &= -\sqrt{\rho} Q^f \sin^2\theta_W\,. \end{aligned} \qquad (2.3)$$

To obtain the physical cross-sections for fermion production at centre-of-mass energies close to the mass of the Z boson, numerous corrections must be applied to these basic diagrams, as is shown in the following sections.

2.2 Photonic corrections

Radiation of photons from the initial or final state fermions or photon exchange between them, so-called "Photonic" corrections, are large and, furthermore, depend on experimental cuts. The lowest order diagrams involving one real or virtual photon are shown below.

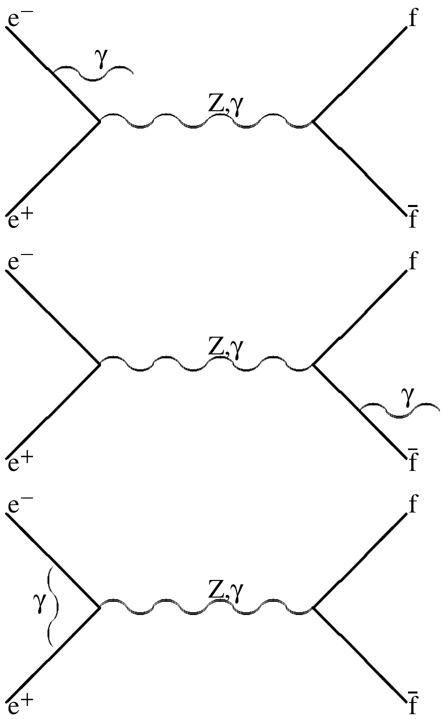

• • •

The corrections are known to $O(\alpha^2)$ with soft real and virtual contributions taken into account to all orders by exponentiation; this is indicated by the dots in the above figure.

The dominant diagram is bremsstrahlung from the initial state, which leads to an effective reduction of the centre-of-mass energy for the e^+e^- annihilation process. Photonic corrections are taken into account by convoluting the cross-section for the hard scattering process with a "radiator function", H(s,s'), readily calculable from QED [18]. H(s,s') describes the probability for the effective centre-of-mass energy being reduced from s to s' due to photon radiation. The convolution integral is

$$\sigma(s) = \int_0^s \sigma_{ew}(s') H(s,s') ds'\,, \qquad (2.4)$$

where σ_{ew} denotes the electroweak cross-section before photonic corrections.

These corrections are large (about 30 % of the total cross-section at the peak of the Z resonance), but known to very high accuracy. The theoretical uncertainty on these corrections is estimated to be less than 0.1 %.

2.3 QCD corrections

If the final state fermions are quarks, then QCD corrections have to be taken into account, *i. e.* radiation of gluons from or exchange of gluons between the final state quarks. The Feynman graphs below show the lowest order contributions involving one real or virtual gluon; the dots indicate higher order contributions.

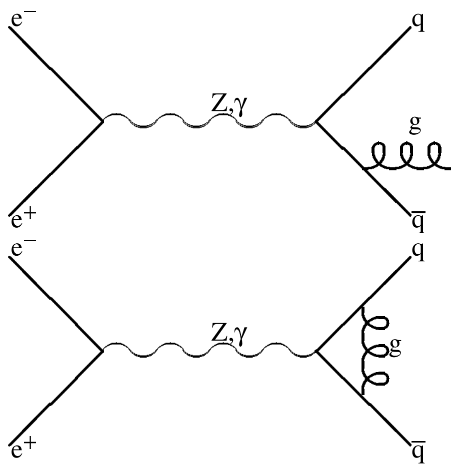

These corrections are known to third order in the strong coupling constant, α_s. An effective parametrisation of the multiplicative correction factor, δ_{QCD}, for the production of hadronic final states, including quark mass corrections, is given by [19]

$$\begin{aligned} \delta_{QCD} &= 1.060 \cdot \frac{\alpha_s(m_Z)}{\pi} + 0.90 \cdot \left(\frac{\alpha_s(m_Z)}{\pi}\right)^2 \\ &\quad -15 \cdot \left(\frac{\alpha_s(m_Z)}{\pi}\right)^3 . \end{aligned} \tag{2.5}$$

The size of the uncertainties is estimated to be equivalent to a systematic error of 0.003 on $\alpha_s(m_Z)$.

2.4 Electroweak corrections

The interesting diagrams at LEP are the genuine electroweak vertex and propagator loops as depicted by the set of diagrams shown below †. It is through processes represented by these diagrams that LEP observables become sensitive to heavy particles like the top quark, the yet undiscovered Higgs boson or even particles outside the scope of the present Standard Model.

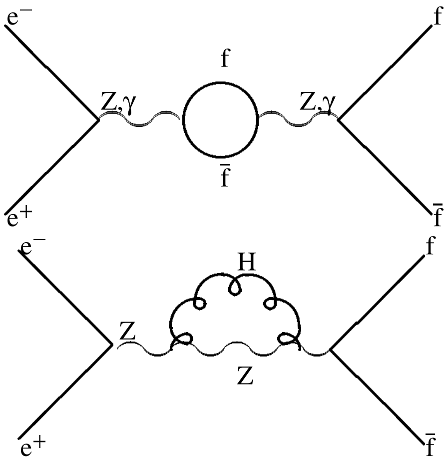

† The separation of electroweak from QED and QCD corrections is true only approximately; at the present level of precision required non-factorisable corrections become also important [20].

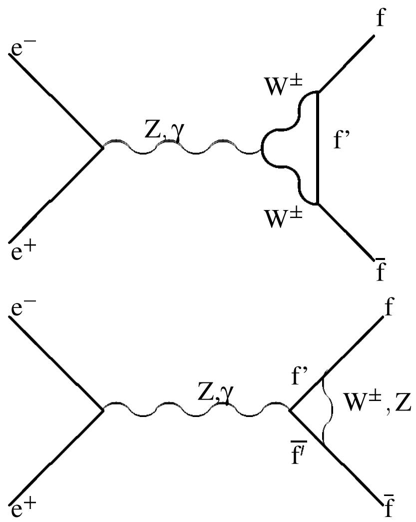

For the interpretation of experimental results and their comparison with theoretical predictions it is convenient to retain the structure of the simple Born-level relations and to include the dominant effects of higher order corrections in the parametrisation of the cross-section by replacing the Born-level couplings as given in equations 2.2 and 2.3, by "effective" couplings ("improved Born approximation" [21]):

$$\begin{aligned} g_v &\to \hat{g}_v = \sqrt{\rho^{\mathrm{eff}}}(I_3^{\mathrm{f}} - 2Q^{\mathrm{f}} \sin^2\theta_{\mathrm{W}}^{\mathrm{eff}}) \\ g_a &\to \hat{g}_a = \sqrt{\rho^{\mathrm{eff}}} I_3^{\mathrm{f}} , \end{aligned} \tag{2.6}$$

thereby introducing an effective ρ parameter, ρ^{eff}, and an effective weak mixing angle, $\theta_{\mathrm{W}}^{\mathrm{eff}}$.

The sine of the effective weak mixing may be written as

$$\sin\theta_{\mathrm{W}}^{\mathrm{eff}} = (1+\Delta\kappa)(\sin\theta_{\mathrm{W}})^0 \tag{2.7}$$

$$\text{with } (\sin^2\theta_{\mathrm{W}})^0 (\cos^2\theta_{\mathrm{W}})^0 = \frac{\pi\alpha(m_{\mathrm{Z}})}{\sqrt{2}G_{\mathrm{F}} m_{\mathrm{Z}}^2} .$$

$(\sin\theta_{\mathrm{W}})^0$ is a purely QED-corrected quantity, where QED effects have been absorbed into the value of the running electromagnetic coupling constant, $\alpha(m_{\mathrm{Z}}) \equiv \bar{\alpha} = \alpha/(1-\Delta\alpha)$ at centre-of-mass energy $\sqrt{s} = m_{\mathrm{Z}}$ ‡. The parameter $\Delta\kappa$ contains all of the genuine electroweak corrections.

The value of the electromagnetic coupling constant at the scale of the Z mass is different from the one measured at lower energies due to vacuum polarisation effects, and a value of $1/\alpha(m_{\mathrm{Z}}) = 128.896 \pm 0.09$ [22] is taken here.

The effects from electroweak corrections also modify the basic tree level relation between the gauge boson masses and the couplings, which now becomes

$$\begin{aligned} \sin^2\theta_{\mathrm{W}} \cos^2\theta_{\mathrm{W}} &\equiv \left(1 - \frac{m_{\mathrm{W}}^2}{m_{\mathrm{Z}}^2}\right) \frac{m_{\mathrm{W}}^2}{m_{\mathrm{Z}}^2} \\ &= \frac{\pi\alpha}{\sqrt{2}G_{\mathrm{F}} m_{\mathrm{Z}}^2} \frac{1}{1-\Delta r} , \end{aligned} \tag{2.8}$$

‡ The speed of light, c, is taken to be equal to one throughout this report.

where Δr absorbs all electroweak corrections. It is common to split Δr into parts arising from contributions of vacuum polarisation diagrams to the photon propagator, $\Delta\alpha$, and pure weak corrections, Δr_w, by

$$\frac{1}{1-\Delta r} = \frac{1}{1-\Delta\alpha}\,\frac{1}{1-\Delta r_w}\,.$$

The $b\overline{b}$ final state is a special case due to the dominant couplings of the b to the top quark via the $W^{\pm}$. Usually, vertex corrections such as shown in the last two Feynman diagrams above are small; however, in the case f'=t and f=b, the strong coupling of the b quark to the t quark leads to a significant correction depending on the top quark mass. This almost cancels the contribution from the top quark in the propagator. It is convenient to introduce a fourth parameter, δ_b, which modifies the b quark couplings through corrections to the effective ρ parameter and weak mixing angle, which become for b quarks

$$\begin{aligned} \rho^{\mathrm{eff,b}} &= \rho^{\mathrm{eff}}(1+\delta_b) \\ \sin^2\theta_W^{\mathrm{eff,b}} &= \sin^2\theta_W^{\mathrm{eff}}(1-\tfrac{1}{2}\delta_b)\,. \end{aligned} \tag{2.9}$$

The quantities $\Delta\rho$, $\Delta\kappa$ and δ_b represent radiative corrections measurable at LEP at $\sqrt{s} \simeq m_Z$ from the couplings of the Z to fermions, whereas measurements of m_W are sensitive to Δr_w. These corrections are all calculable within the Standard Model. Full one-loop calculations with leading $O(\alpha^2 m_t^4)$ and $O(\alpha\alpha_s)$ are available [23, 24, 25]. They use m_Z, m_t, m_H, $\alpha(m_Z)$ and α_s as input parameters and calculate QED and QCD corrected observables. In leading order, the dependence on the top quark mass, m_t, is quadratic, whereas the dependence on the Higgs boson mass, m_H, is only logarithmic.

The agreement of electroweak observables with expectations is an important test of the Standard Model, both of its correctness as a renormalisable quantum theory and of its completeness at the energy scale of interest.

3 The Large Electron-Positron collider

The large electron-positron collider, LEP, at CERN is an e^+e^- storage ring with a circumference of almost 27 km built under the Swiss-French border between Lake Geneva and the Jura mountains. It was designed to operate at centre-of-mass energies $\sqrt{s} \simeq m_Z \simeq 91$ GeV ("LEP I") and later on at energies beyond 160 GeV up to a planned 200 GeV ("LEP II"). Electrons and positrons collide at four places in large caverns under ground, where four omni-purpose detectors, ALEPH, DELPHI, L3 and OPAL, are located. The CERN accelerator complex and the positions of the experiments are depicted in Figure 3.1 .

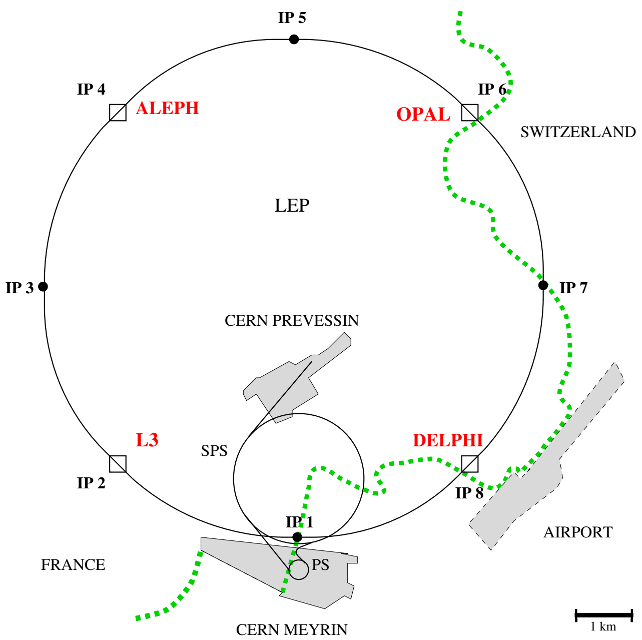

Figure 3.1: *Map of the CERN accelerators PS, SPS and LEP under the Swiss-French border.*

The first Z bosons were produced and observed by the experiments in summer 1989. Since then, the operation of the machine and its performance could be steadily improved. At the end of data taking around the Z resonance the peak luminosity had reached nearly twice its design value. This was well matched by improvements made to the detectors, in particular their trigger and data acquisition systems, over the years of operation. The energy of the beams in LEP could be determined with high precision, and all experiments improved on their initial measurements of the luminosity of the colliding beams. These improvements were crucial to benefit from the large statistics which had accumulated to some 16 million Z decays detected in total by the four experiments.

The following sections describe the important features of the accelerator and give an overview of the beam energy calibration.

3.1 The LEP accelerator

The main emphasis of the description in this section is on those aspects immediately important to electroweak precision physics; more details than can be given in this section are described in the literature [8]. The main properties of the accelerator are summarised in Table 3.1 .

LEP is composed of eight sections equipped with bending magnets ("octants") and eight straight sections. An octant is formed by 31 standard cells, each 79.11 m in length and consisting of a defocusing quadrupole, a vertical orbit corrector, a group of six bending dipoles, a focusing sextupole, a focusing quadrupole, a horizontal orbit corrector, a second group of six bending dipoles and finally a defocusing sextupole. Encounters of electron and positron bunches occur in the straight sections. Unwanted collision during set-up or at places without experiments are avoided by electrostatic separators. The four experiments are located in the centre of the straight sections two, four, six and eight. The straight sections also house the radio frequency cavities.

The dipole field was chosen quite low, only $\sim$0.05 T at 45 GeV beam energy, permitting a novel and cheap magnet design. The dipoles consist of steel plates of 1.5 mm thickness with 4 mm wide gaps between them, which are filled with mortar. The quadrupoles produce magnetic fields with alternating polarity providing "strong focusing". The sextupoles serve to compensate the dependence of the focusing strength on the beam energy. While groups of quadrupoles and sextupoles and all of the dipole magnets are powered in series, the corrector dipoles are powered individually to correct deviations of the dipole fields and to steer the beams through the centre of LEP.

On either side of each experiment strong superconducting quadrupoles are placed to reduce the transverse beam dimensions at the interaction point ("IP") to about 5 μm and 200 μm in the vertical and horizontal planes, respectively. Additional rotated quadrupoles compensate the coupling from the horizontal to the vertical plane which would otherwise increase the vertical beam size.

The current exciting the LEP magnets is controlled by 750 precisely stabilised power supplies with output power ranging from less than 1 kW to 7 MW. The current for an energy corresponding to the mass of the Z is about 2000 A.

The energy loss of about 125 MeV per turn of electrons and positrons due to synchrotron radiation is compensated by the acceleration in the radio frequency ("RF") cavities.

parameter		value
circumference	C	26 658.88 m
magnetic radius	ρ	3096 m
revolution frequency	f_{rev}	11.2455 kHz
RF frequency f_{av}	Cu cavities	352.254170 MHz
RF wavelength	$\lambda_{RF} = c/f_{av}$	0.85107 m
harmonic number	h_{av}	31324
RF frequency f_1	SC cavities	352.209188 MHz
RF wavelength	$\lambda_{RF} = c/f_1$	0.85118 m
harmonic number	h_1	31320
injection energy	≤1995	20 GeV
	≥1996	22 GeV
peak luminosity, LEP I		$23 \cdot 10^{30}$ cm^{-2}s^{-1}
		60 nb^{-1}/h over 5 h
number of bunches per beam	≤1992	4
	1993–94	8, pretzel mode
	1995	12, bunch train mode
	≥1996	8, bunch train mode
current/bunch		∼0.3 mA

Table 3.1: *LEP Parameters, see text for explanations*

The original RF system consisted of 128 copper cavities powered by 16 klystrons, located around the L3 (straight section 2) and OPAL (straight section 8) interaction points. For LEP II, this was upgraded by the addition of high-gradient, superconducting cavities around all four experiments.

Substantial savings in power consumption were achieved due to the coupling of the accelerating cavities to spherical low-loss cavities, in which the micro wave energy can be stored between the passage of particles. The accelerating cavities run at a frequency of f_1=352.209 MHz, while the storage cavities have a resonance frequency, f_2, of 352.299 MHz. Thus the energy oscillates between the two cavities with the beating frequency $f_2 - f_1$, which is eight times the revolution frequency, and the average frequency seen by the beams is $f_{av} = (f_2 + f_1)/2$. However, the alignment of the cavities was done in multiples of $\lambda^1_{RF} = c/f_1$, so that the cavities appear to be placed too far away from the interaction point for a system running at f_{av} with $\lambda^{av}_{RF} = c/f_{av}$. This results in a substantial correction on the centre-of-mass energy for collisions occurring between straight sections equipped with copper cavities.

Under stable operating conditions, the total orbit length is an integer multiple, the so-called harmonic number, of the RF wavelength. Therefore the orbit length depends directly on the RF frequency which must be chosen such that the particles pass on average through the centre of the quadrupoles and sextupoles, *i. e.* to put the beam on the "central orbit".

Deviations ΔR of the average beam position from the central orbit lead to contributions of the quadrupole fields to the bending of the particles and hence to substantial changes in beam energy, which are given by

$$\frac{\Delta R}{R_{LEP}} = \alpha_c \frac{\Delta E}{E_{\mathrm{beam}}} , \tag{3.1}$$

where α_c (=$1.86 \cdot 10^{-4}$ during most of the LEP I running) is the "momentum compaction factor". Therefore the beam energy is very sensitive to such displacements relative to the centre of the quadrupoles, which can be caused either by changes in the RF frequency or by deformations of the ring geometry due to geological effects.

For this and other reasons, equipment to measure the beam position relative to the centre of the quadrupoles is vital. 504 Beam Observation Monitors ("BOM"s), consisting of four electrostatic pick-up plates each, are mounted at the front ends of the quadrupoles. This system was upgraded before the 1993 running period, achieving a precision of about 20 μm thereafter.

Electrons and positrons from the CERN accelerator complex are injected into LEP at 20 GeV beam energy, where they are accelerated to the final energy, stored and brought into collision at four interaction points. The beam intensity steadily decreases, and after typically eight to twelve hours in collision both beams are finally dumped and the machine is refilled. The period between filling the electrons and positrons into LEP and the time of dumping them is referred to as a "fill".

After the first collisions had been observed in 1989, the machine has undergone many changes to improve the luminosity and to increase its energy, until in 1996 the threshold for W pair production was first crossed. The number of bunches was increased from the initial four to eight during the years 1993 and 1994 and finally to twelve bunches in 1995, whereby electrostatic separators suppressed unwanted

year	beam energy [GeV]	integrated luminosity [pb^{-1}]
1989	45.6±1.5	1.4
1990	45.6±1.5	7.6
1991	45.6±1.5	17.3
1992	45.6	28.6
1993	45.6±1.	40.0
1994	45.6	64.5
1995	45.6±1.	39.8
fall 1995	130,136	6.2
1996	161, 172	23.4
1997	183	73.3

Table 3.2: *Beam energies and integrated luminosities delivered per experiment. In 1990 and 1991, a total of about 7 pb^{-1} was taken at off-peak energies, and 20 pb^{-1} per year in 1993 and in 1995. The total luminosity used by the experiments in the analyses was smaller by 10-15 % due to data taking inefficiencies, caused largely by bad background conditions preventing some detector components from being operated, and by read-out dead times.*

collisions. In eight-bunch mode, equally spaced bunches travelled on "pretzel" orbits. In twelve-bunch mode, four equally spaced "trains" with three bunches each, spaced 74 m apart, were used, since this is compatible with multi-bunch operation at LEP II ("bunch train mode"). The original radio frequency system was gradually upgraded by superconducting cavities to prepare for the energy increase at LEP II. Particularly in 1995 commissioning of new superconducting cavities went on in parallel with data taking for physics. However, most of the running around the Z resonance was done with almost all of the total RF power delivered by the copper RF system.

Over the years, a steady increase was achieved in luminosity delivered to the experiments; Table 3.2 summarises the data taking periods, the approximate centre-of-mass energies and the delivered integrated luminosities.

3.2 Determination of the centre-of-mass energy

The energy of the particles colliding at the interaction points and the associated uncertainties are an important input to the determination of the Z parameters, because the cross-section close to the resonance, at $\sqrt{s} \simeq m_Z$, is a rapidly varying function of energy. A precise determination of the mass and the width of the Z was achieved by changing the centre-of-mass energies from fill to fill during certain periods of LEP I data taking, so-called "energy scans". Scans around the pole of the Z resonance were performed at seven different energy points spaced about one GeV apart in 1990 and 1991, and at 3 different energy points, close to the peak and about two GeV below and above, in 1993 and 1995. These points will be called "peak", "peak-2" and "peak+2", respectively. Data taking in 1992 and 1994 was exclusively at the peak.

The uncertainty in the absolute energy scale, *i. e.* uncertainties correlated between the energy points, directly affect the mass, whereas the Z width is only influenced by the error in the difference in energy between energy points. The determination of the mass and width are completely dominated by the high-statistics scans taken at the peak±2 points in 1993 and 1995 and the errors are therefore approximately given by

$$\begin{aligned} \Delta m_Z &\approx 0.5\,\Delta(E_{+2}+E_{-2}) \\ \Delta\Gamma_Z &\approx \frac{\Gamma_Z}{E_{+2}-E_{-2}}\Delta(E_{+2}-E_{-2})\,. \end{aligned} \tag{3.2}$$

In order to fully exploit the statistics accumulated by the experiments, a precision of $O(10\text{ ppm})$ on the energy is desirable.

Another energy related effect is also important: the energy of the particles in a bunch is not equal to the average beam energy, but oscillates about this mean with a width of about 50–60 MeV. In addition, the average beam energy of different data sets summed up under one energy point varies slightly. This variation has to be added in quadrature to the spread in centre-of-mass energy. Measurements of observables are commonly quoted at a sharp centre-of-mass energy, and therefore a significant correction due to the energy spread has to be applied.

A brief summary of the energy calibration procedure is given below, many more details can be found in the various reports by the working group on LEP energy determination [26, 27].

3.2.1 Overview of the energy calibration

The very accurate determination of the average energy of the beams in LEP was based on the technique of resonant spin depolarisation [28], which became available in 1991, after transverse polarisation of the electron beam in LEP had first been observed in 1990 [29] with a Compton polarimeter [30]. This method offers a very high precision of ±0.2 MeV on the beam energy at the time of the measurement. However, such measurements were only possible outside normal data taking with separated beams, typically at the end of fills. Therefore, other techniques had to be employed to trace back the very precise energy determination to earlier times in a fill and to those fills where no calibrations by resonant depolarisation could be made.

The average momentum of particles circulating in a storage ring is proportional to the magnetic bending field integrated over the path of the particles. For particles on central orbit this is given by the field produced by the bending dipoles and corrector magnets and by small contributions from the Earths magnetic field or from remnant fields in the beam pipe. Contributions from the quadrupoles and sextupoles also have to be considered for non-central orbits according to equation 3.1 . In order to obtain the energy of the particles colliding at an interaction point, additional effects from the RF system and from a possible energy-dependence of the distribution of particle positions in a bunch, so-called "dispersion effects", have to be considered.

The energy calibration proceeds in four steps:

1. Determination of the beam energy, and hence the integral over the magnetic field along the path of the circulating particles, at certain points in time, usually the end of (some) fills. This was achieved by resonant spin depolarisation measurements.

2. Measurements of the magnetic field and correction of the energy for any difference in magnetic field compared to the reference point. Several devices were available for this purpose:

   (a) a wire loop threading all the dipoles ("flux loop"), which measured the time integrated voltage induced during ramping up the dipoles;

   (b) measurements of the dipole current;

   (c) measurement by means of an nuclear magnetic resonance probe ("NMR") of the magnetic field in a reference dipole, which was powered in series with the ring dipoles in the LEP tunnel but installed in a building at the surface;

   (d) two NMR probes installed in 1995 in two of the tunnel dipoles which measured the magnetic field directly above the beam pipe.

3. Correction for changes in the orbit position, with an analytical formula for daily deformations originating from tidal forces of the moon and the sun, and using the BOM system for long-term changes of the LEP geometry.

4. Application of corrections specific to each interaction point depending on RF parameters and the local dispersion.

The final precision on m_Z and Γ_Z is entirely dominated by the large off-peak statistics collected in 1993 and 1995. The discussion below concentrates on the description of the energy determination for these years; the assigned systematic errors are summarised in Table 3.4 in subsection 3.2.10 . The earlier results are described in references [31] and, *e. g.*, [32].

3.2.2 Resonant spin depolarisation

The spin-flip probability during the emission of synchrotron radiation in a storage ring has a large asymmetry in favour of orienting the magnetic moments of the beam particles along the direction of the bending field. Thus, "transverse polarisation" * builds up naturally in an ideal storage ring reaching an asymptotic value of 92.4 % with a typical rise time τ_p depending strongly on the beam energy, E_{beam}, and the radius of the accelerator [33]. In practice, depolarising resonances from radial field distortions, *i. e.* magnetic field imperfections affecting the vertical orbit position, and the fields of the experimental solenoids reduce polarisation to an unobservable level. Careful adjustment of the vertical orbit and compensation of the experimental solenoids by application of vertical bumps in the arcs close to the straight sections on either side of each experiment were needed to achieve noticeable polarisation levels in LEP. Up to 55 % and typically between 10 % and 20 % were observed during special running conditions outside physics data taking. Polarisation during collisions was seen under special conditions only, but never became a tool for routine operation, since random orbit kicks from beam-beam interactions could not be compensated.

The spin vector of polarised electrons precesses about the direction of the bending field where the number of precessions per turn, the "spin tune", is given by $\nu_s = \frac{1}{2}(g_e - 2)\gamma$; here $\frac{1}{2}(g_e - 2)$ is the electron magnetic moment anomaly, $\gamma = E/(m_e c^2)$ is the Lorentz factor of electrons with energy E and mass m_e, and c is the speed of light. Measuring ν_s therefore determines the beam energy according to

$$\begin{aligned} E_{\text{beam}} &= \nu_s \cdot m_e c^2 / \tfrac{1}{2}(g_e - 2) \\ &\equiv \nu_s \cdot 0.4406486(1)\ \text{GeV}. \end{aligned} \tag{3.3}$$

An energy of 45.6 GeV corresponds to a spin tune of 103.5 .

The spin tune is measured by creating an artificial depolarising resonance. This is done by exciting a weak, oscillating magnetic field in radial direction. Under the influence of this field, the polarisation vector is slightly rotated away from the vertical axis at each turn, and depolarisation after about 10^4 turns occurs if the depolarising field is in phase with the spin precession, *i. e.* if its frequency, f_{dep}, is equal to the fractional part of the spin tune multiplied by the revolution frequency,

$$f_{dep} = (\nu_s - \text{int}(\nu_s)) \cdot f_{rev}. \tag{3.4}$$

The measurement of the spin tune is performed by slowly varying with time the frequency of the depolarising field ("frequency sweep"). The time at which depolarisation occurs can then be associated with the depolarising frequency, f_{dep}, and with the fractional part of the spin tune according to equation 3.4 . The integer part of the spin tune has to be inferred from the strength of the magnetic bending field and is known with sufficient precision of about ± 20 MeV , whereas one unit in spin tune corresponds to about 440 MeV .

The polarisation level itself is determined by measuring the position distribution of circularly polarised laser light

* The polarisation vector is defined as the average over all electron spins in the bunch.

scattered back from the electron beam in a compact high-density tungsten calorimeter with silicon strip readout giving good position resolution. The laser light of 532 nm wavelength is generated by a high-power frequency-doubled NdYAG laser, pulsed at 30-100 Hz. After circular polarisation by means of a rotating $\lambda/4$ plate the laser light is steered onto the electron beam by a system of mirrors. A second mirror system and calorimeter were installed in 1993 and served to measure the polarisation of the positron beam. The quantity of interest is the vertical shift in the position of the centre-of-gravity of the backscattered photons, ΔY, upon reversal of the circular polarisation of the laser light, which depends on the transverse polarisation, P, of the electrons,

$$\Delta Y = \kappa \xi P. \tag{3.5}$$

κ is the analysing power of the polarimeter set-up, estimated to be (500 ± 30) μm, and ξ is the level of circular polarisation of the laser light.

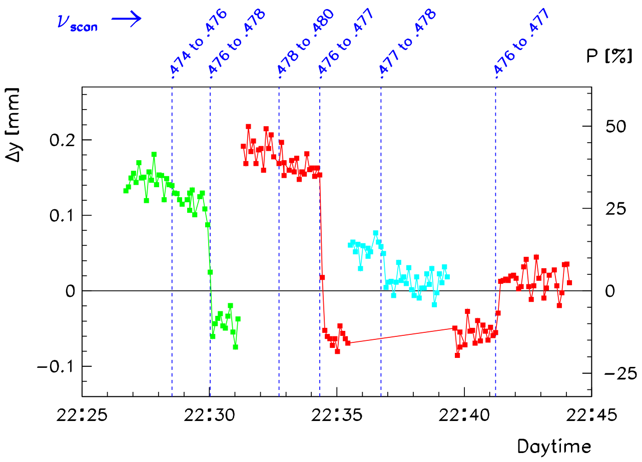

Figure 3.2: *Example of an energy calibration by resonant depolarisation performed on several bunches in turn. The dotted lines indicate the frequency sweeps of the radial oscillating field. Negative polarisation levels occurred due to partial spin flips, which were verified by another depolarisation.*

To unambiguously determine the average beam energy, more than one depolarisation measurement is necessary. If depolarisation occurs at $\nu_{dep} = f_{dep}/f_{rev}$, then $1 - \nu_{dep}$ or $\nu_{dep} \pm Q_s$, where Q_s is the synchrotron tune, also lead to depolarisation. By changing in turn the RF frequency (and hence the beam energy) and the synchrotron tune one can resolve these ambiguities.

The total systematic error on a single measurement of the beam energy was estimated to be only ± 0.2 MeV and is supported by the excellent reproducibility and short-term stability of the measured beam energy.

Long-term changes of the beam energy are caused by drifts of the magnetic fields in the dipoles due to aging, current spikes or temperature effects, or by gradual deformations of the accelerator geometry due to geological effects. The typical variation with time of the beam energy was found to be $\sim$1 MeV /h. It is therefore important to have many precise calibrations spaced equally over the time of an energy scan.

In 1993, 24 fills, corresponding to 40 % of the total integrated luminosity taken at the peak$\pm$2 points, could be calibrated, and in 1995 calibration succeeded for 27 longer fills, corresponding to two thirds of the integrated luminosity taken off-peak. In addition, six fills could be calibrated before physics data taking started. These measurements were particularly useful for the understanding of the changes in beam energy during fills.

3.2.3 The magnetic dipole field

The extrapolation of the well-known values of the beam energy at the end of fills to earlier times required a modelling of the dependence of the magnetic field of the bending dipole magnets on current and temperature. The new NMR probes installed in two dipoles in the LEP tunnel in 1995 revealed a typical behaviour of the magnetic field as is shown in Figure 3.3 . A steep rise at the beginning of the fill - when most of the luminosity was taken - is followed by a slower rise towards the end of the fill - when the calibration was performed.

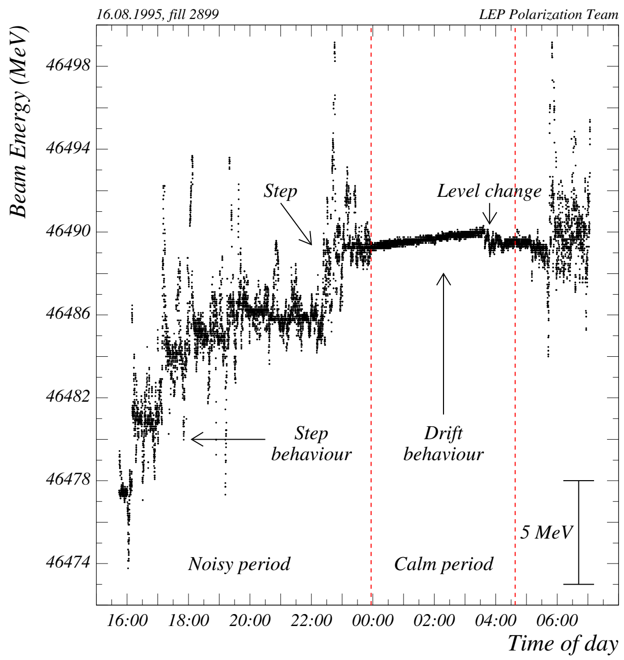

Figure 3.3: *Time evolution of the magnetic field for a typical fill, observed with the NMR probes installed in two dipoles.*

The rise of the magnetic field with time was found to be much larger than had been inferred from measurements of the dipole current or of the magnetic field in the reference magnet. The rise was confirmed by the six fills which had been calibrated with resonant depolarisation at the beginning and end. Since most fills were calibrated at the end only, the understanding of the time dependence of the dipole field is crucial. The origin of the field changes is a combination of effects from temperature, from spikes in the dipole currents and from vagabonding currents flowing through the LEP beam pipe, which are caused by electrical trains in the Geneva area. The calm period between midnight and 4:00 in the morning seen in Figure 3.3 reflects the fact that no trains were moving at this time.

Temperature dependence

The detailed behaviour of the magnetic field was studied in a test set-up consisting of spare dipole magnets equipped with current bars, beam pipe, NMRs, cooling water system and temperature probes. By changing the cooling water temperature the dipole temperature could be controlled and the response of the magnetic field was measured. A rather complex behaviour was found, as is shown in Figure 3.4 .

An empirical model was derived from these measurements which relates the magnetic field B at a temperature T of the dipole cores to five parameters reflecting the history of the magnet since the last demagnetisation cycle. These parameters are the initial core temperature T_i, the maximum and minimum temperatures, T_{min} and T_{max}, since the last demagnetisation cycle, a reference temperature T_0, and the cooling water temperature T_w describing the effects of temperature gradients across the magnet. The B field is parameterised by

$$\begin{aligned} B &= B_0[\,1+C_{T_i}(T_i-T_0)+C_T(T-T_i) \\ &\quad +C_{T_{min}}(T_{min}-T_i)+C_{T_{max}}(T_{max}-T_i) \\ &\quad +C_{T_{grad}}(T-T_w)\,]\;. \end{aligned} \tag{3.6}$$

The temperature coefficients C_{T_x} were determined from studies with the test set-up and have typical values between $1{\cdot}10^{-5}$ to $10{\cdot}10^{-5}\,\mathrm{K}^{-1}$; the quality of the description achieved is shown by the flat line on the top plot of Figure 3.4 .

Under data taking conditions, the profile of the average ring temperature is simpler than the scenario shown in Figure 3.4 . In 1993, the temperature constantly went up during the course of a fill. In 1995, due to a modification to the cooling system, it went up during the initial part of a fill and then went down towards the end, but never fell below the initial temperature, and therefore $C_{T_{min}}$ is unimportant. Other temperature differences were usually small, and therefore the dominant temperature dependence can be described by an effective temperature coefficient, defined as

$$C_{eff} = \begin{cases} C_{T_{max}} + C_T & \text{if } \frac{dT}{dt} > 0\,, \\ C_T & \text{if } \frac{dT}{dt} < 0\,. \end{cases} \tag{3.7}$$

Clearly, the coefficients measured for only *one* magnet are not representative of the average over the ~ 3400 dipoles in LEP or of the two dipoles equipped with NMR probes in 1995. 16 magnets in total were equipped with temperature and NMR probes for the 1996 run, and dedicated temperature experiments performed. This allowed a better sampling of the average ring behaviour. As expected from the test set-up, the magnetic field showed a constant rise throughout the fill even if the temperature decreased towards the end. C_{eff} was determined for the average over the LEP dipoles and for the two magnets with NMRs in 1995, with errors of 30 % and 60 %, respectively, during periods with a rise in average dipole temperature, and with an uncertainty of 50 % on both coefficients for decreasing temperature.

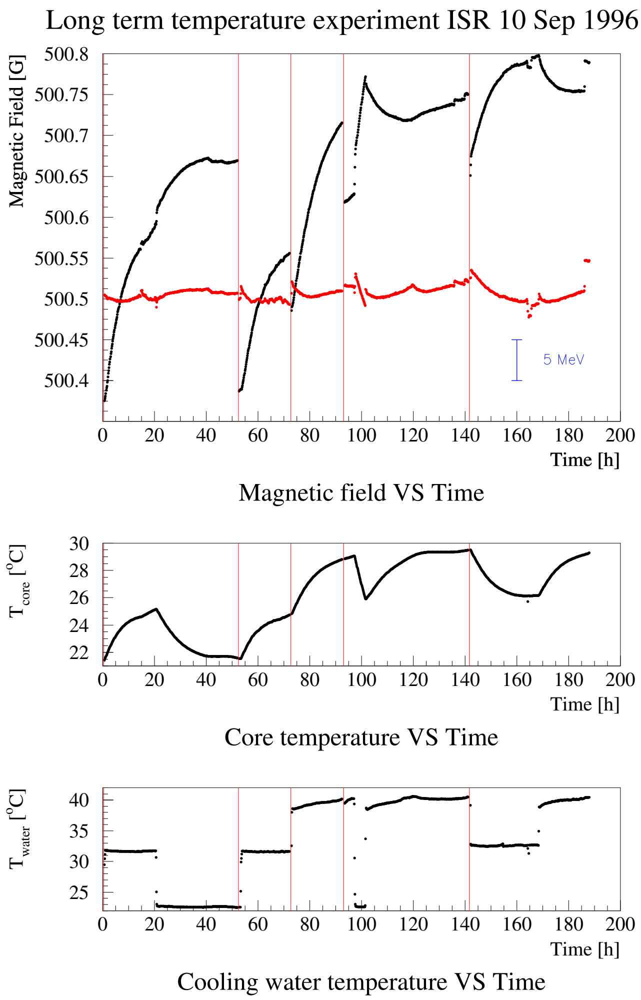

Figure 3.4: *Time evolution of the magnetic field measured in a test set-up. The bottom diagram shows the cooling water temperature, the middle one shows the dipole temperature, and the top figure shows the magnetic field. The second curve on the top figure shows the magnetic field after correction with the temperature model developed from such measurements.*

Dependence on parasitic currents

The effect of parasitic currents on the LEP beam pipe was also investigated with the test set-up. Such parasitic currents are caused by leakage currents from electrical trains moving in the Geneva area. Current spikes of about 1 A were measured on the beam pipe, entering near IP1 and IP6. Such current spikes always lead to an increase of the magnetic dipole field due to hysteresis effects: after a short increase of the magnetic field and an additional magnetisation of the iron in the dipoles the magnetisation does not go back to its original value, but stays higher.

Playing back the current recorded during one day of LEP operation onto the beam pipe in the test set-up resulted in the same change in magnetic field in the test dipole as had been measured by the NMRs in the tunnel at that day.

Bending modulations

In order to reduce hysteresis effects a new technique was tried in the later parts of the 1995 energy scan. The magnets were subjected to a series of current spikes at the beginning of fills, so-called “bending modulations”. These led to jumps in the magnetic field at the time of the bending modulations and also, as intended, to a reduced sensitivity of the magnetic field to current spikes occurring thereafter.

Modelling of the energy rise during a fill

Since NMR information was not available in 1993 and 1995, the model to describe the average rise of the magnetic field during fills must be independent of the NMRs. The temperature model is used as described above, and the rise effects from parasitic currents are parameterised as a function of the time elapsed since the demagnetisation of the magnets (the start of fill), t_{fill}, and the time-of-day, t_{day}, using the 1995 NMR measurements. The dependence on t_{day} reflects the train schedule, and t_{fill} is needed to describe the saturation behaviour of the magnets.

The approximate validity of the independence of effects from temperature and parasitic currents assumed in the above model was checked with a more deterministic rise model. This model uses the parasitic currents recorded during one week as representative of any week of LEP operation, and the combined effects of temperature and parasitic currents were derived from the measurements with the test set-up.

By using the two different models or by direct use of the 1995 NMR data the systematic errors could be controlled. In addition, the six fills with calibrations at the beginning and end could be compared with the model prediction; this is shown in Figure 3.5 . Note that these measurements were not used to determine any parameters of the rise model. The r.m.s. spread of 0.4 MeV is smaller than the error expected from the uncertainties assigned to the model parameters, which amounts to 1.2 MeV.

The error on the mean beam energy due to the modelling of the energy rise in 1995 is estimated to be 0.6 MeV . Since more cross-checks and constraints exist for 1995, the error in previous years is larger, amounting to about 3 MeV. The error correlation coefficients between peak-2 and peak+2 were estimated to be 0.86 in 1993 and 0.47 in 1995.

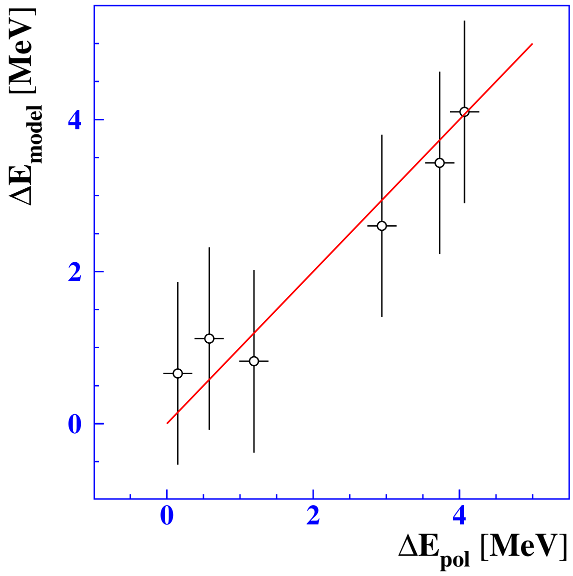

Figure 3.5: *The beam energy rise in a fill predicted by the model compared to the 6 fills in 1995 with resonant depolarisation calibrations at the beginning and end. The r.m.s. of the difference is only 0.4 MeV ; this is smaller than expected from the uncertainties in the model, which is indicated by the vertical error bars.*

3.2.4 Orbit position

The influence of changes of the ring geometry is, to first order, given by equation 3.1 . The orbit length is fixed by the RF frequency, and therefore changes in the ring geometry lead to radial displacements of the orbit. The most impressing example of this is certainly the dependence of the orbit position on gravitational forces of the Moon and the Sun [34].

These tidal forces lead to time-dependent deformation of the Earth and affect the LEP geometry at a level of $O(10^{-8})$, *i. e.* the radius of LEP changes by ∼0.1 mm. This translates into energy changes of ∼7 MeV. The first long-term experiment is shown in Figure 3.6, several others were made during the following years and improved the quantitative understanding of the effect. The relative displacement of the beam as a result of tidal forces was also observed both by direct observation with the BOM system and by determination of the “central frequency”, *i. e.* the RF frequency at which the beam is at the central orbit.

Tides are the origin of the fastest changes of the average orbit position, but there are also long-term drifts of the average beam position. These are caused by the distribution of weight of geological objects in the Geneva area. A clear correlation with the water level in Lake Geneva was seen, as well as a dependence on strong rain fall in the Jura Mountains. Such changes in orbit position of $O(300\ \mu\mathrm{m})$ led to quite substantial changes in beam energy over the course of

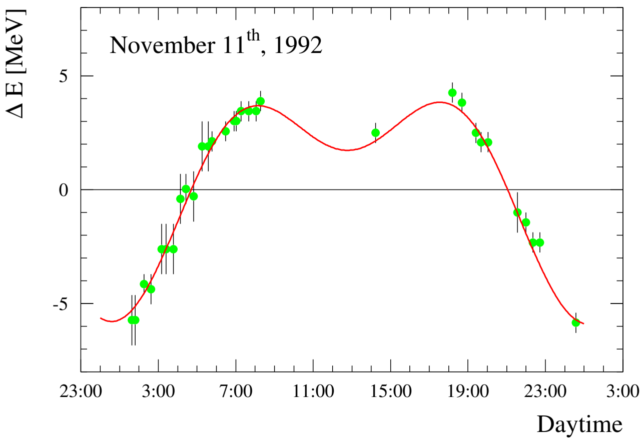

Figure 3.6: *The first long-term observation of the beam energy in LEP with resonant depolarisation. The overlayed curve shows the predicted time dependence of the gravitational force in the Geneva area, obtained from the position of the Moon and the Sun, with only one free parameter, the relation between local strain and gravity change.*

a year of $O(20\text{ MeV})$ and could be tracked with the BOM system.

3.2.5 Energy differences between bunches

Imperfections of the LEP lattice, combined with the energy variation around the LEP ring and with pretzel orbits, could lead to small energy differences between the electron and positron bunches. After the first measurement in 1993 of the positron energy with resonant depolarisation had given an indication of such a difference, other studies of this kind were repeated during 1994 and 1995 and lead to a much smaller effect, $\Delta E_{+,-} \lesssim (0.3 \pm 0.3)$ MeV.

The energy differences between bunches in bunch train mode in 1995 was also investigated during special studies with resonant depolarisation and found to be $\Delta E_{A,C} = (-0.1 \pm 0.1)$ MeV.

3.2.6 Corrector dipoles

The approximately 260 horizontal and 320 vertical corrector dipoles in LEP can have an effect on the beam energy depending on their settings. The horizontal correctors can lead to additional bending and increase the effective dipole field, and both the horizontal and vertical correctors lead to a lengthening of the orbit. To avoid double counting of the correction, two separate models were developed taking into account only the first or only the second effect, and good agreement was seen. The predicted energy changes could be confirmed by beam energy measurements with resonant depolarisation before and after deliberately changing the corrector settings. Differences between the two approaches of at most 0.5 MeV were conservatively assigned as the systematic error.

3.2.7 Static magnetic fields

Static magnetic fields also affect the beam energy. One such source is the Earth's magnetic field which changes the beam energy by -0.9 MeV.

The focusing (QF) and defocusing (QD) quadrupoles in LEP were operated at different currents to achieve a phase advance of 60° per lattice cell in the horizontal and of 90° in the vertical plane. The field from the current in the quadrupole power bars led to a stray field of about 7 μT at the position of the beam. This was compensated by a special compensation current loop in 1993, which was no longer operated in 1995.

Such additional fields do not need special correction procedures, since they are naturally taken into account by the resonant depolarisation measurements.

3.2.8 Local effects at the interaction points

So far, the average energy of electrons and positrons in the parts of the machine equipped with bending magnets was considered, which is not equal to the energy of the particles at the collision point.

RF correction

One substantial correction arises from the positioning of the copper RF cavities. This is illustrated in Figure 3.7, which shows the deviation from the average beam energy at different positions around LEP.

Ideally, if the positioning of the RF units had matched well the frequency at which they were operated and in the absence of alignment errors, the sum of the energies of the electron and positron beams would have been constant round the whole ring. However, since the copper cavities were placed too far from the interaction point, particles arrive too early at an interaction point with respect to the RF phase and receive too much energy in the cavities. On the contrary, particles leaving the interaction point are late and hence get less energy by about the same amount. As a result, the energy at the interaction point of both beams is higher by about 10 MeV than the average beam energy in the LEP arcs. If the copper system was run at its maximum power, the centre-of-mass energy was therefore higher by about 20 MeV at interaction points located in straight sections equipped with copper cavities, *i. e.* L3 and OPAL. The two other IPs, *i. e.* ALEPH and DELPHI, remained nearly unaffected, unless the powering of the RF units was asymmetrically distributed or if there had been a difference in path length for particles going from IP2 to IP6 via IP4 or via IP8.

Modelling of RF induced shifts in centre-of-mass energy needs as the most important input the energy gains in each RF section and the excitation currents of special wiggler magnets, which were used during operation to control the bunch length and also increased the energy loss per

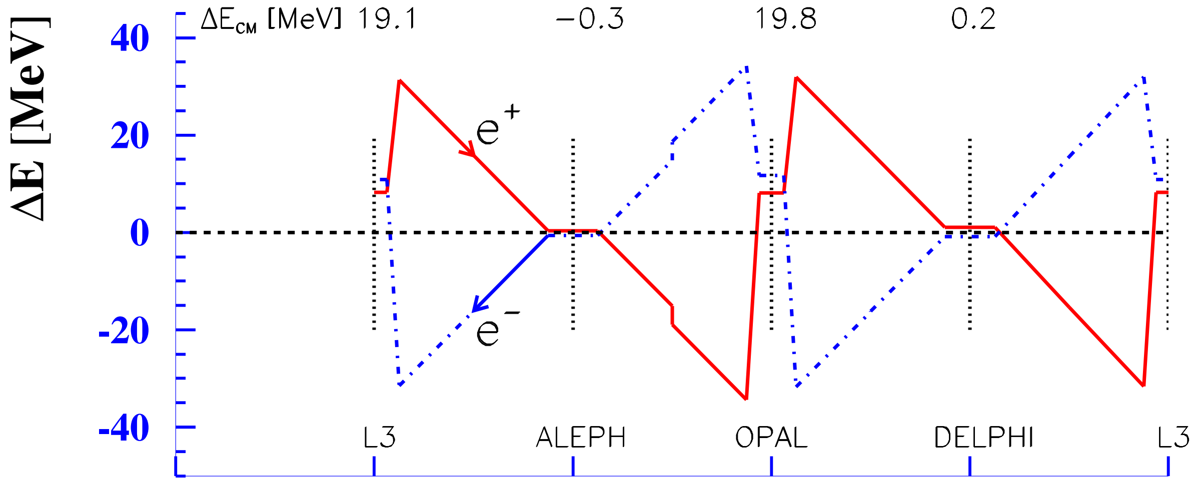

Figure 3.7: *Deviation from the average beam energy as a function of position in LEP. Synchrotron radiation in the bending dipoles or in the wiggler magnets, as well as wake fields of the particle bunches in unused cavities or at discontinuities of the beam pipe lead to energy losses, which are compensated in the RF cavities. The situation shown here corresponds to the average running conditions in 1993.*

turn. There also is a small dependence on beam currents, which results from energy extraction by the bunches from the RF cavities; this was particularly important in bunch train mode.

An asymmetric distribution of power over the RF units also led to shifts in the longitudinal position of the interaction point, Δz, which were measured by the experiments and could be used as a cross-check on the modelling of the RF-related effects. Another by-product of the RF model is a calculation of the synchrotron tune, Q_s, which could be compared with measurements. The difference between the calculated and measured Q_s served as a continuous monitoring tool during operation and ensured the approximate correctness of the accelerating voltages and their phases being input to the RF model.

Although the correction is quite large, about 20 MeV when all copper cavities were operated like in 1993 and partly in 1995, its uncertainty is rather small, ~ 1 MeV for L3 and OPAL and much less in ALEPH and DELPHI, since most of the effect is of purely geometrical origin.

The typical average size of the RF correction on the centre-of-mass was +13 MeV in 1990–1992, +20 MeV in 1993 and 1994 and +5 MeV or +15 MeV at the OPAL respectively L3 interaction points, and below 0.5 MeV at the ALEPH and DELPHI interaction points.

Unlike-sign dispersion at the IP

The average centre-of-mass energy depends on how the bunches collide if the energy of a particle depends on its position in the bunch. The bumps generated by electrostatic separators in bunch train mode introduced vertical dispersion at the interaction point, which had opposite sign for electrons and positrons. This was only important for running in 1995 and later. Figure 3.8 illustrates how the average centre-of-mass energy is affected by unlike-sign dispersion.

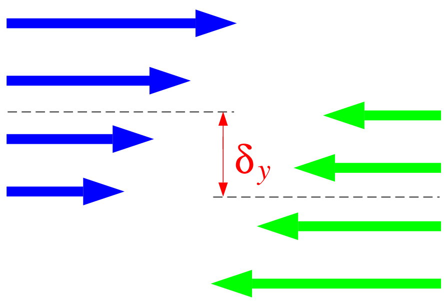

Figure 3.8: *Illustration of the effect of unlike-sign dispersion at the IP. The length of the arrows indicates the magnitude of the particle energy. Any offset between the colliding bunches leads to a shift in centre-of-mass energy and also changes the energy spread.*

The energy shift is given by

$$\Delta E_{cm} = -\frac{1}{2} \cdot \frac{\delta y}{\sigma_y^2} \cdot \frac{\sigma_E^2}{E} \cdot \Delta D_y^* \,, \qquad (3.8)$$

where σ_y is the beam size, σ_E is the energy spread, and $\Delta D_y^* = D_{e^+}^* - D_{e^-}^*$ is the difference in vertical dispersion between the electrons and positrons. Good control of the collision offset, δy, is essential to keep these effects small. This was achieved by small vertical movements of the beams and adjusting them such that the luminosity was maximised. Two such adjustments per fill, at the beginning and in the middle, were performed routinely during data taking. Any residual differences in collision offset lead to a correction which relies on the parameters in equation 3.8 being known. An evaluation of the parameters involved led to sensitivities of the centre-of-mass energy to the collision offsets of -2.3, 1.3, -1.4 and 1.6 MeV/μm for IPs two, four, six and eight, respectively. Typical average collision offsets were about or less than 0.5 μm, leading to small corrections with systematic uncertainties of only $\sim$0.5 MeV.

3.2.9 Spread of the beam energy

The energy of a given particle in a bunch oscillates around the mean energy with a frequency which is given by the synchrotron tune of the accelerator multiplied with the revolution frequency. Therefore, the colliding particles are not exactly at the mean energy described above. The energy spread δE is readily calculable from machine parameters and can be checked using the longitudinal size of the bunches, measured from the longitudinal size of the luminous region at the interaction points. The values of the centre-of-mass energy spread are shown in Table 3.3 .

	energy spread [MeV]		
year	peak$-$2	peak	peak+2
1990		46.	
1991		46.	
1992		51.	
1993	54.6	55.4	55.6
1994		54.9	
1995	55.5	56.1	56.5

Table 3.3: *Centre-of-mass energy spread. The uncertainties on the energy spread are ±5 MeV in 1992 and before, ±1.1 MeV in 1993 and 1994 and slightly larger, 1.3 MeV, in 1995 due to dispersion at the interaction points. The values for 1995 differ slightly among the IPs; given are the averages over all four IPs.*

Due to the energy spread, observables are not measured at a sharp energy, E^0_{cm}, but instead their values are averaged over a range in energies $E^0_{cm} \pm \delta E_{cm}$. With the assumption of a Gaussian shape of the energy distribution, an energy dependent observable O receives a correction given in lowest order Taylor expansion by

$$\delta O(E^0_{cm}) \simeq -\frac{1}{2}\left|\frac{d^2O(E)}{dE^2}\right|_{E=E^0_{cm}} \cdot \delta {E_{cm}}^2 \,. \tag{3.9}$$

Note that the calculation of this correction needs theoretical knowledge of the energy dependence, $O(E)$, of the observable in question.

3.2.10 Calibration results

The mean beam energy was determined as a function of time, as summarised by the following formula:

$$\begin{aligned} E_{\mathrm{beam}}(t) = \;& C_{norm}(fill)\cdot E(t=0) \\ & \cdot(1+C_{tide}(t))\cdot(1+C_{orbit}(fill)) \\ & \cdot(1+C_{T-dipole}(t)) \\ & \cdot(1+C_{rise}(t_{day},t_{fill})) \\ & \cdot(1+C_{hcorr}(t)) \end{aligned} \tag{3.10}$$

- $E(t=0)\cdot C_{norm}$ is a term ensuring that the beam energy equals the one determined by resonant depolarisation at the time of calibration for calibrated fills. For uncalibrated fills C_{norm} is taken to be the average of the calibrated fills, while the value of $E(t=0)$ depends on peculiarities of the year of running: it is taken to be the average of the calibrated fills in 1995; it follows the dipole current in 1994 (due to a drifting power supply); and it follows the magnetic field in the reference magnet in 1993 (due to frequent flux loop calibrations).
- C_{tide} is the correction for tidal effects.
- C_{orbit} is the correction for long-term drifts of the average orbit position.
- $C_{T-dipole}$ accounts for the influence of the average dipole temperature.
- C_{rise} parametrises the effect of the energy rise from parasitic currents on the beam pipe.
- C_{hcorr} takes into account the effect from the use of the horizontal corrector magnets.

Error on the mean beam energy for uncalibrated fills
The overall energy scale of fills not calibrated with resonant depolarisation is set to the average of all calibrated fills. However, this average has a statistical error depending on the residual r.m.s spread of the calibrated fills after applying all known model corrections, σ_{cal}, and by the number of calibrated fills, N_{cal}, and is therefore given by $\sigma_{cal}/\sqrt{N_{cal}}$. Taking the difference between the energy predicted by the model and the energy actually measured by resonant depolarisation allows to determine σ_{cal} for the different energy points as the r.m.s. of the resulting distribution, as shown in Figure 3.9 . In addition, if we assume that the uncalibrated fills show the same scatter as calibrated ones, the mean energy of uncalibrated fills also has an error of $\sigma_{cal}/\sqrt{N_{uncal}}$, were N_{uncal} is the number of uncalibrated fills. Hence, the extra contribution to the error on the average energy of all fills arising from the uncalibrated fills is given by

$$\begin{aligned} \sigma_{uncal} &= \frac{N_{uncal}}{N_{tot}}\left(\frac{\sigma_{cal}}{\sqrt{N_{cal}}} \oplus \frac{\sigma_{cal}}{\sqrt{N_{uncal}}}\right) \\ &= \frac{\sigma_{cal}\sqrt{N_{uncal}}}{\sqrt{N_{tot}}\sqrt{N_{cal}}} \,. \end{aligned} \tag{3.11}$$

Note that this formula serves for illustration only since it neglects weighting by integrated luminosity.

σ_{uncal} is largest for the peak points and is labelled “mean fill energy” in Table 3.4 .

Source	P−2 '93	P '93	P+2 '93	P '94	P−2 '95	P '95	P+2 '95	Energy correl.	Year correl.
	errors on the mean beam energy								
Energy Measurement	0.50	0.50	0.50	0.50	0.50	0.50	0.50	0.04	0.04
B rise, scatter+model	2.80	3.00	2.50	3.30	0.62	0.62	0.62	[0.47,0.86]	0.50
B rise, NMR T-coeff.	0.60	0.32	0.60	0.51	1.04	1.04	1.08	0.75	0.75
Ring Temperature	0.14	0.38	0.40	0.22	0.38	0.30	0.42	0.75	0.75
Bending modulation	0.	0.	0.	0.	0.04	1.36	0.28	0.75	0.
Tide Amplitude	0.02	-0.34	0.20	-0.12	-0.05	-0.03	-0.03	$\pm$1.	1.
Tide Phase	0.02	0.04	-0.08	0.13	-0.16	-0.03	0.05	$\pm$1.	0.50
e^+ energy	0.30	0.30	0.30	0.30	0.25	0.25	0.25	0.50	[0.,0.50]
Horizontal correctors	0.04	0.36	-0.40	0.22	-0.24	-0.54	-0.18	$\pm$0.75	$\pm$0.75
QFQD Correction	0.24	0.20	0.20	0.04	0.0	0.0	0.0	0.75	[0.,0.75]
Mean fill energy	1.73	5.90	0.87	1.10	0.83	4.96	0.45	0.	0.
	errors on IP-dependent corrections, averages over IPs								
RF	0.53	0.53	0.53	0.57	0.69	0.69	0.69	[0.63,0.96]	[0.18,0.70]
Dispersion	0.40	0.40	0.40	0.70	0.35	0.35	0.35	[0.50,0.75]	[0.,0.50]

Table 3.4: *Breakdown of errors, in MeV , on the centre-of-mass energy, for illustrative purpose only (from [26]). The last two columns give the correlation coefficient between energy points and between years of running, respectively. Whenever the year to year or the energy point to energy point correlation coefficient is not the same the range is indicated. The sign of the correlation coefficient is given by the relative sign of the errors.*

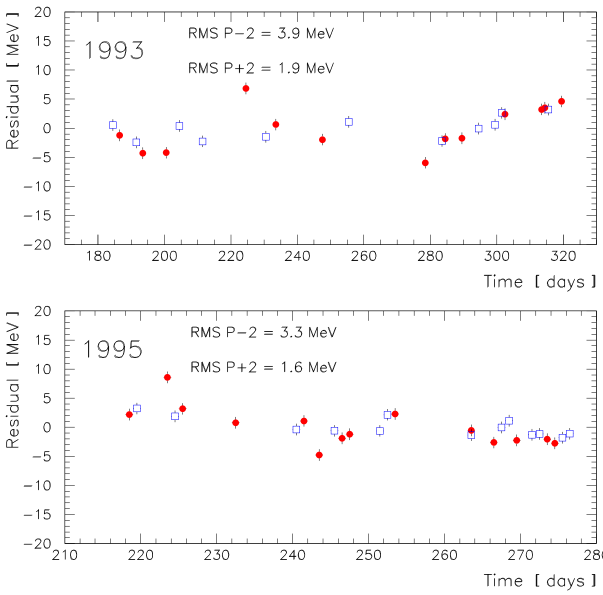

Figure 3.9: *Difference between centre-of-mass energies measured by resonant depolarisation and from the model for calibrated off-peak fills. The closed circles are for peak-2 and the open squares for peak+2 energy points. The error bars have a size of $\pm$1 MeV .*

Summary of uncertainties

An overview of all systematic errors from the energy calibration and typical correlations between energy points and years is shown in Table 3.4 . The dominant systematic error at the off-peak points originates from the magnetic field rise during fills and is largest for the off-peak points in 1993. To ensure proper propagation of the energy errors to m_Z or Γ_Z, which are not affected by anti-correlated or correlated parts of the errors on the off-peak points, respectively, a full correlation matrix is needed. This is given in Table 3.5, which takes into account correlations between the interaction points and is therefore valid only for combined results of all four experiments.

'93 p-2	'93 p	'93 p+2	'94 p	'95 p-2	'95 p	'95 p+2
3.42^2	2.76^2	2.59^2	2.25^2	1.29^2	1.19^2	1.20^2
	6.69^2	2.64^2	2.38^2	1.14^2	1.20^2	1.15^2
		2.95^2	2.16^2	1.23^2	1.25^2	1.33^2
			3.62^2	1.23^2	1.30^2	1.24^2
				1.78^2	1.24^2	1.22^2
					5.39^2	1.34^2
						1.68^2

Table 3.5: *Covariance matrix elements, $(\mathcal{V}^E)$, in MeV ^{2}, from the determination of the centre-of-mass energies for the scan points in 1993–1995.*

Energy values were produced for 15 min time intervals of running. These were used in the analyses by the experiments to compute luminosity-weighted average centre-of-mass energies and their spread at each energy point. These central values in combination with the full energy error matrix were then used in the fitting procedures to extract the Z resonance parameters. Compared to other errors, energy related uncertainties affect significantly only the mass and the width of the Z. The effect of the energy related uncertainties on parameters extracted from the measurements is discussed in section 6.4 and is summarised in Table 6.5 .

4 The detectors at LEP

The detectors ALEPH, DELPHI, L3 and OPAL are located at the interaction points four, eight, two and six in LEP, respectively. They provide precise measurements of the energy and the momentum vectors of charged and neutral particles over nearly the full solid angle*. The design of the detectors was guided by the requirement to detect all types of interactions occurring in e^+e^- collisions around the Z resonance and beyond the threshold for $W^\pm$ pair production and to allow an unambiguous classification of the resulting events to be made. Beyond the main goal, the precise determination of the Z couplings to electron, muon, tau and quark pairs, investigations of the properties of τ leptons and of heavy quarks and QCD studies are also important and are reflected in good double-track resolution and particle identification capabilities of the detectors.

Although the detectors are quite different in detail, they share some common design criteria. All detectors consist of a cylindrical section, called "barrel", typically covering the range $40° < \theta < 140°$, and two "endcap" sections, covering the forward regions down to $\sim$25 mrad from the beam direction. The main components are

- a silicon strip vertex detector to precisely measure the position of charged tracks very close to the interaction point (implemented during the first years of operation);
- tracking detectors immersed in a magnetic field to measure charged track directions and the specific ionisation loss;
- an electromagnetic calorimeter in the barrel and endcap parts to absorb and measure the energy of electrons and photons;
- a hadron calorimeter in the barrel and endcap parts to measure the energy deposit of strong interacting particles together with the electromagnetic calorimeter and to act as a muon filter;
- muon detectors in the barrel and endcap parts to measure the position of muons leaving the hadron calorimeter
- and two forward detector systems placed at small angles w.r.t. the beam line at each end of the detector to measure the Bhabha scattering cross-section which serves as the reference reaction to determine the luminosity of the colliding beams.

A summary of the most important performance parameters is given in Table 4.1 . More details and comments on the specialities of each detector are given in the following sections.

The data acquisition systems, in conjunction with the trigger systems of the detectors, are capable of recording all genuine Z and $W^\pm$ pair event, except, of course, $Z \to \nu\overline{\nu}$. The trigger systems use signals from essentially all detector components, making them highly redundant. This leads to trigger efficiencies close to 100 % for the standard reactions of interest and to good control of the efficiencies.

All four collaborations developed very detailed Monte Carlo simulations of their detectors [35]. By modelling in detail the response of the detector components to traversing particles [36], acceptances and efficiencies for the various reactions of interest are determined and detector effects can be unfolded to study the underlying physics. Numerous event generators [37], common to all experiments, for $q\overline{q}$, $\mu^+\mu^-$, $\tau^+\tau^-$ final states and for e^+e^- final states at small and large angles and for two-photon reactions provide the physics input to these detector simulations. Dedicated generators are used in searches for Higgs bosons or new particles. The generated particles and their energies and momenta serve as the input to the detailed detector simulations, which produce output in the same format as the real detector readout systems. The simulated data are subsequently processed by the same reconstruction and analysis programs as are used on the real data.

4.1 The ALEPH experiment

The general layout of ALEPH [9], "A detector for LEP PHysics", is shown in Figure 4.1 .

The central tracking detector is a large, cylindrical time projection chamber ("TPC"), 4.4 m in length and 3.6 m in diameter, which provides 21 precise three-dimensional coordinates along charged tracks produced by particles traversing the full radial range. 338 samples of ionisation measurements permit the determination of the specific ionisation loss, dE/dx, which contributes to particle identification. The small inner tracking chamber ("ITC") with axial wires at radii between 13 cm and 29 cm provides up to eight coordinates per track in the plane perpendicular to the magnetic field and aids in triggering on charged particles originating from the interaction point. Two layers of silicon strips, placed at radii of 6.5 cm and 11.5 cm, provide precise measurements of the z and ϕ coordinates of tracks very close to the interaction point. This system was first operated in 1991 and upgraded for the high energy running in 1995 by a new detector, which improved the acceptance in θ from $|\cos\theta| < 0.85$ to $|\cos\theta| < 0.95$. The whole tracking system is situated inside a superconducting solenoid producing a strong magnetic field of 1.5 T in the z direction.

*In the following, a right-handed coordinate system is used for each of the detectors with the z axis pointing in the direction of the e^- beam and the x axis pointing towards the centre of LEP; in polar representation, the polar angle, θ, is measured from the z axis, and the azimuthal angle, ϕ, from the x axis about the z axis.

		ALEPH	DELPHI	L3	OPAL
magnet		superconducting	superconducting	normal	normal
field strength		1.5 T	1.23 T	0.5 T	0.435 T
silicon strip vertex detector					
hit resolution	$r\phi$	12 μm	8 μm	7 μm	5 μm
	z	10 μm	9 μm	14 μm	13 μm
vertex detector					
hit resolution	$r\phi$	150 μm	85 μm	–	55 μm
	z	70 mm	–	–	40 mm (ΔT), 0.7 mm (stereo)
central detector		TPC	TPC	TEC	jet chamber
hit resolution	$r\phi$	180 μm	250 μm	50 μm	135 μm
	z	$\sim$1 mm	0.9 mm	–	45 mm
outer chambers					
hit resolution	$r\phi$	–	110 μm	–	15 mm
	z	–	35 mm	320 μm	300 μm
momentum resolution ($\cos\theta \simeq 0$)	$\sigma(1/P_T)$	$0.6\cdot 10^{-3}$(GeV /c)$^{-1}$	$0.6\cdot 10^{-3}$(GeV /c)$^{-1}$	($0.6\cdot 10^{-3}$(GeV /c)$^{-1}$ for $\mu^{\pm}$ only)	$1.3\cdot 10^{-3}$(GeV /c)$^{-1}$
electromagnetic calorimeter		lead-prop. tubes	“HPC”/lead glass	BGO	lead glass
granularity	barrel	3×3 cm^2	$\sim 2\times 2$ cm^2	2×2 cm^2	10×10 cm^2
	endcap	same as barrel	5×5 cm^2	same as barrel	same as barrel
energy resolution	σ_E/E	$0.18\sqrt{E/\mathrm{GeV}}\oplus 0.01$	$0.32\sqrt{E/\mathrm{GeV}}\oplus 0.04$	$0.02\sqrt{E/\mathrm{GeV}}\oplus 0.01$	$0.06\sqrt{E/\mathrm{GeV}}\oplus 0.02$
hadronic energy resolution		$0.85\sqrt{E/\mathrm{GeV}}$	$1.12\sqrt{E/\mathrm{GeV}}\oplus 0.21$	10 % at 45 GeV	1. (at $<$15 GeV) to $1.2\sqrt{E/\mathrm{GeV}}$
luminosity detector		Si-W sampling & lead sandwich	lead-scintillating tiles & mask	BGO & Si $r\phi$ strips	Si-W sampling & lead sandwich
fiducial acceptance	inner // outer radius	6.1 cm // 14.5 cm	6.5 cm // 42.0 cm	7.6 cm // 15.4 cm	6.2 cm // 14.2 cm
	θ_{min} // θ_{max} [mrad]	30. // 48.5	43.6 // 113.6	32. // 54.	31.3 // 51.6

Table 4.1: *Performance parameters of the LEP detectors. Resolutions given are valid for the barrel parts only.*

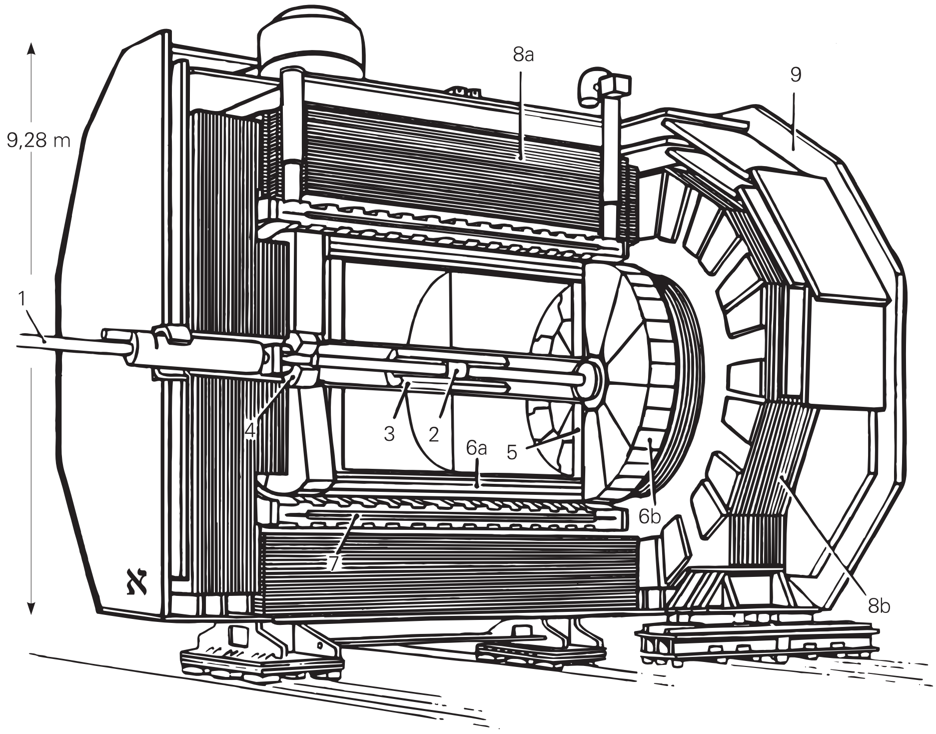

Figure 4.1: *The ALEPH detector. Its components are 1: beam pipe, 2: silicon vertex detector, 3: inner tracking chamber, 4: luminosity detector, 5: end plate of the time projection chamber, 6a,b: barrel and endcap parts of the electromagnetic calorimeter, 7: superconducting coil, 8a,b: barrel and end cap parts of the hadron calorimeter, 9: muon chambers.*

Still inside the solenoid an electromagnetic calorimeter consisting of alternating layers of lead and proportional tubes measures the positions and energies of electromagnetic showers using small 30×30 mm^2 readout pads, which are segmented into three sections in radial depth of four and two times nine radiation lengths. This allows measurements of the transverse and longitudinal shower development, which are important for particle identification.

The hadron calorimeter, outside the solenoid, is made of iron plates interleaved with limited-streamer tubes. The 1.2 m of iron also serve as the magnet return yoke and as muon filter. The calorimeter is read out in projective towers to sum up the energy of interacting hadrons, and the tubes also provide digital output signals to track penetrating muons.

Two double-layers of limited streamer tubes at the outside of the iron form the muon detector. They are read out via strip electrodes running parallel and perpendicular to the wires and provide ϕ and z coordinates of traversing muons.

At small angles, 40 mrad$< \theta <$155 mrad, a calorimeter very similar in construction to the electromagnetic calorimeter and a tracking device in front of it were mounted to determine the energies and positions of electrons and positrons from the Bhabha scattering process. This system allowed the determination of the luminosity with a precision of better than 1 %. To achieve higher precision, the tracking device was replaced in 1992 by a very compact silicon-tungsten calorimeter, extending the acceptance down to $\theta >$24 mrad and at the same time providing very good position resolution and hence a good definition of the acceptance. The experimental uncertainty on the determination of the luminosity could be reduced below 0.1 %.

4.2 The DELPHI experiment

DELPHI [10], the "DEtector with Lepton, Photon and Hadron Identification", is shown schematically in Figure 4.2 and employs many novel techniques aiming at superb particle identification capabilities.

The tracking system is segmented into a number of independent devices. The vertex detector consists of three layers of silicon strips with $r\phi$ readout at radii of 6.3, 9.0 and 10.9 cm. The third layer was added in 1991, and z readout was added to the first and third layer in 1994; the angular coverage of the inner layer was increased from $|\cos\theta| < 0.72$ to $|\cos\theta| < 0.91$ at the same time. At radii between 12 and 23 cm there is a drift chamber with jet chamber geometry, measuring up to 24 $r\phi$ coordinates per track. z information is obtained from multi-wire proportional chambers with circular cathode strips surrounding the jet chamber. The acceptance was $|\cos\theta| < 0.92$ for a minimum of 10 wires per track; this was extended by a new detector in 1995 to $|\cos\theta| <0.97$. The central detector is

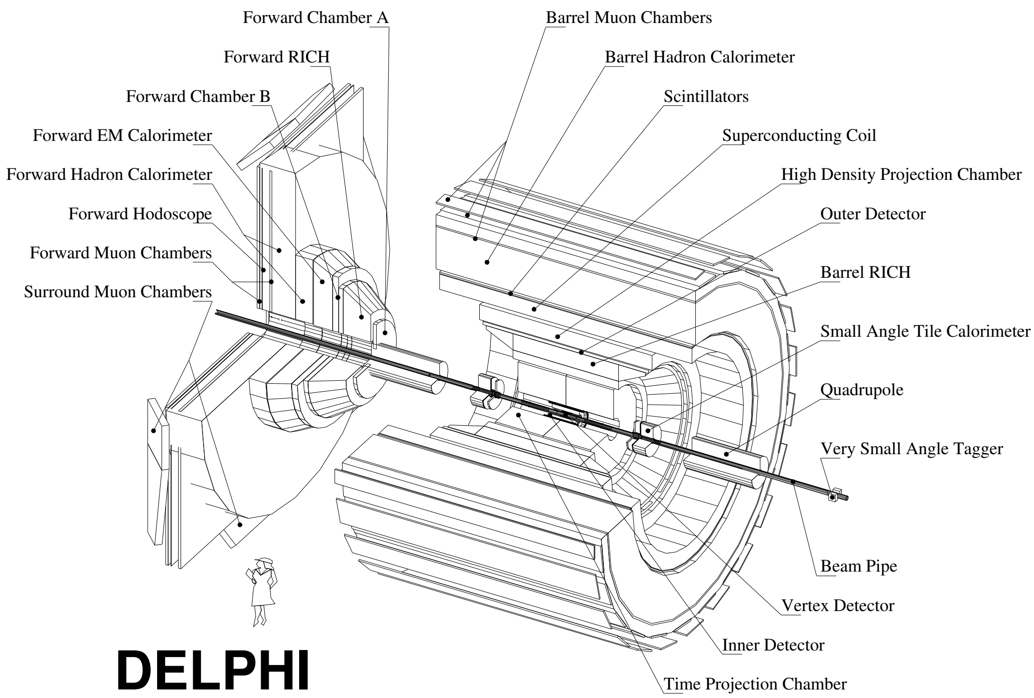

Figure 4.2: *The DELPHI detector*

a time projection chamber with 16 three-dimensional coordinates and 192 samples of ionisation loss measurements for tracks traversing the full radial range between 40 and 110 cm. Five layers of drift tubes, the "outer detector", surround the time projection chamber and provide $r\phi$ coordinates; three layers provide z information using timing information at the end of the anode wires. In the forward region, two forward chambers are mounted. One uses three modules of limited streamer tubes, each module with two staggered planes. The acceptance range of this chamber is $0.85 < |\cos\theta| < 0.98$. The second forward chamber is a drift chamber with 12 readout planes rotated by 120° with an acceptance $0.81 < |\cos\theta| < 0.98$. The tracking detector is inside of a magnetic field of 1.23 T in the z direction, which is provided by a superconducting solenoid.

Ring imaging Cherenkov detectors are located in the barrel region between the time projection chamber and the outer detector, and between the forward chambers in the endcap region. In each detector, a liquid and a gas radiator are used for particle identification in the momentum ranges 0.8 GeV $< p <$8 GeV and 2.5 GeV $< p <$25 GeV, respectively. The Cherenkov photons are focused onto photosensitive time projection chambers, where conversion electrons are produced. The angle of photon emission w.r.t the particle track is reconstructed from the tracks of the conversion electrons. The combination of dE/dx from the time projection chamber and measurements of the Cherenkov angle in the liquid and the gas radiator provide good separation of electrons, pions, kaons and protons over most of the momentum range at LEP I.

The electromagnetic calorimetry of DELPHI consists of a barrel calorimeter inside the solenoid and of two forward calorimeters. Each barrel calorimeter module is a small time projection chamber with high density material in the gas volume amounting to 18 radiation lengths. This design achieves an excellent position resolution for electromagnetic showers of ± 1 mrad in ϕ and ± 1.7 mrad in θ.

The forward calorimeters consist of lead glass blocks with a cross-section of 5×5 cm^2 and a depth of 40 cm equivalent to 20 radiation lengths.

Scintillation counters outside the solenoid measure the time-of-flight of charged particles.

The hadron calorimeter is installed in the return joke of the solenoid and consists of 20 layers of limited streamer tubes located in 18 mm wide gaps between 50 mm thick iron plates. The readout is done via cathode pads covering an angular region of $3.75°\times 2.96°$ in $\Delta\phi$ and $\Delta\theta$. The signals from five pads in the barrel and four or seven pads in the endcap are summed to form towers, which are read out independently and provide a high granularity. From 1994 onwards, cathodes of individual streamer tubes are also read out to further improve the granularity of the system.

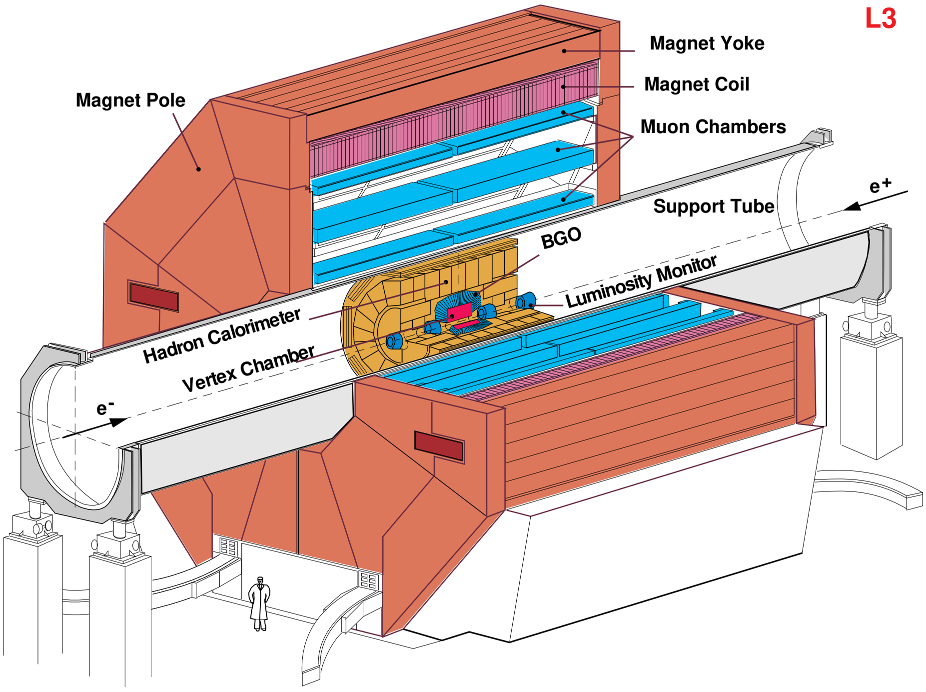

Figure 4.3: *The L3 detector*

Drift chambers in the barrel and endcap region at the outside of the hadron calorimeter serve as muon detector. The system was completed in 1994 by a layer of limited streamer tubes to fill gaps between the endcap and barrel regions.

Two very forward electromagnetic calorimeters on either side of the detector provide for the luminosity measurement. The absolute value is measured by calorimeters in the angular range 43 mrad$< \theta <$135 mrad, and a second set of calorimeters at smaller angles provided a high-statistics measurement of the relative change in luminosity. The system was upgraded in 1994 by a lead-scintillator calorimeter build with the "Shashlik" technique, which covers a wider range between 29 and 185 mrad in θ. Accurate definition of the inner acceptance is achieved on one side only by means of a precisely machined tungsten ring of 17 radiation lengths in front of the calorimeter. This system is capable of determining the absolute luminosity with an experimental systematic error of less than 0.1 %.

4.3 The L3 experiment

L3 [12], the third LEP detector, differs somewhat in design from the others and is shown schematically in Figure 4.3 .

The detector components of L3 are supported by a steel tube 32 m long and 4.45 m in diameter; the LEP beam line runs in the centre of the tube. The magnet coil has a diameter of 11.86 m and provides a magnetic field of 0.5 T. The magnet yoke forms the outside of the structure, all active detector elements are inside the magnetic field. The three layers of precisely aligned muon chambers form a high-resolution muon spectrometer with a precision on the transverse momentum of $\sigma(1/P_T) = 0.55 \cdot 10^{-3}(\mathrm{GeV}/c)^{-1}$. This is one of the prominent features of the L3 detector. For LEP II additional muon drift chambers were mounted in the endcap region extending the range down to $|\cos\theta| < 0.91$.

The hadron calorimeter is made of layers of depleted uranium plates with readout planes formed by proportional wire chambers. The chambers are read out via projective towers covering an angular range of 2° in $\Delta\phi$ and $\Delta\theta$. Inside the support tube, a muon filter is mounted which adds about one absorption length to the hadron calorimeter.

Inside the hadron calorimeter there is a time-of-flight system consisting of plastic scintillators, which is also used for triggering.

The electromagnetic calorimeter is made of BGO crystals, truncated pyramids in shape with 2×2 cm^2 at the inner and 3×3 cm^2 at the outer end and 24 cm in length. This system provides excellent position and energy resolution for electrons and photons.

The central detector, a time expansion chamber ("TEC"), is very small with a radial extension of 31.7 cm only. Its resolution of 50 μm for a total of 50 coordinates along a track is sufficient for charge identification of 50 GeV charged particles at 95 % confidence level. A z-detector consisting of two thin cylindrical multi-wire proportional chambers surrounds the TEC. Using the momentum measurement in the TEC slightly improves the momentum resolution of hadronic jets of 45 GeV in energy to 8.4 % compared to 10.2 % if the calorimeters alone are used.

A silicon vertex detector consisting of two layers with $r\phi$ and z strips each and with an angular coverage $|\cos\theta| <0.93$

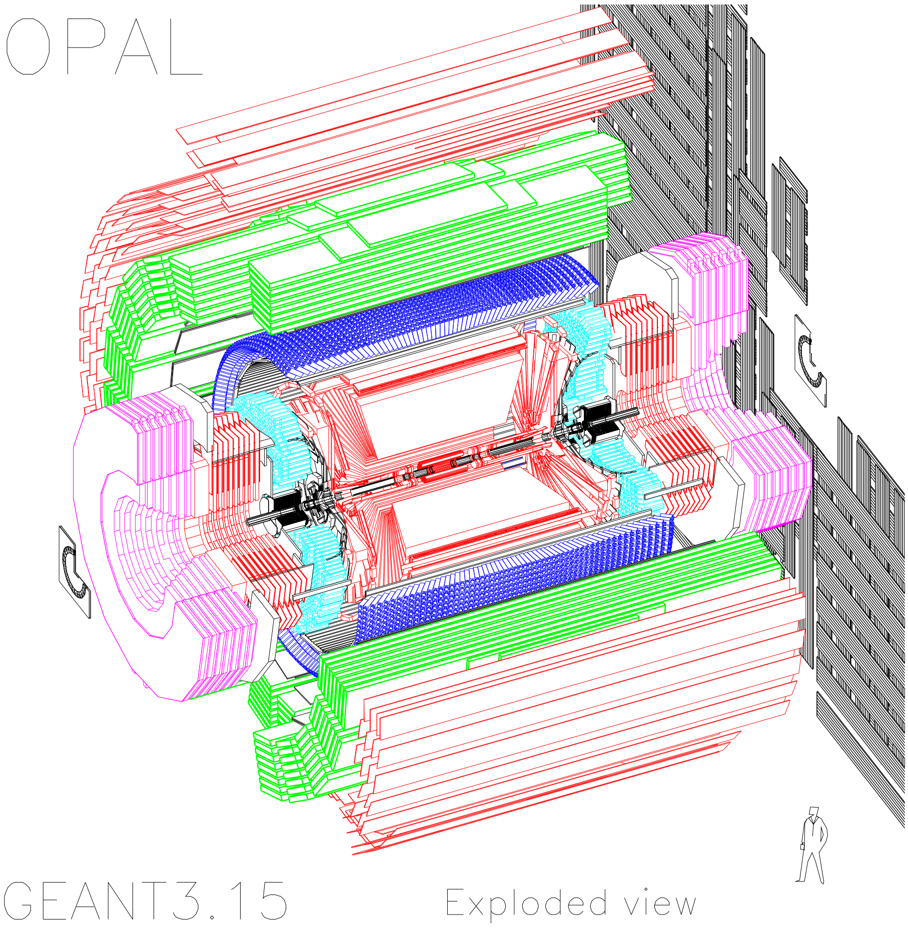

Figure 4.4: *The OPAL detector in an exploded view. This plot is generated from the geometry information used in the Monte Carlo simulation of the detector and illustrates its level of detail. The detector components are described in the text.*

was installed for running in 1994 and thereafter.

The luminosity detector is also made of BGO crystals and covers a range 25 mrad$< \theta <$70 mrad. Its energy resolution is 2 % at 45 GeV, and the angular resolution is 0.4 mrad in θ and 0.5° in ϕ. The systematic error on the luminosity determination was estimated to be 0.6 %. For running in 1993 and later three layers of precise silicon strip detectors were mounted in front of the BGO calorimeter to improve on the position measurement. Experimental systematic errors on the luminosity measurement could thereby be reduced to below 0.1 %.

4.4 The OPAL experiment

The "Omni-Purpose Apparatus for LEP physics", OPAL [11], is the most conventional in design of the four detectors and is shown in Figure 4.4 .

The tracking system consists of a silicon strip micro-vertex detector (installed in 1991), a vertex drift chamber, a large volume jet chamber and outer z-chambers and is contained inside a magnetic field of 0.435 T. The jet chamber is subdivided into 24 sectors with 159 signal wires in each sector and is operated at a pressure of 4 bar to obtain a good resolution of 3.8 % on the ionisation loss measurement. Radially, it extends from 0.25 m to 1.85 m, and at least eight hits are recorded for tracks within $|\cos\theta| <$0.98. Three-dimensional coordinates in (r,ϕ,z) for each hit are obtained from the wire position, the drift time and a charge division measurement of rather limited precision. Left-right ambiguities are resolved by 100 μm staggering of the signal wires. The vertex chamber consists of 36 sectors of the jet chamber design, with 12 wires running parallel to the beam direction and 6 wires inclined by an angle of 4° ("stereo cells") providing z information. The hit resolution is 50 μm in $r\phi$ and about 700 μm in z. z-chambers with 6 planes of wires running perpendicular to the beam direction are placed outside the jet chamber. They measure tracks leaving the jet chamber volume with a precision in z of about 300 μm. The first silicon strip detector consisted of two layers of single-sided silicon detector wafers at radii of 6.1 and 7.5 cm and reached an excellent single hit resolution of 5 μm in $r\phi$. The detector was replaced before data-taking in 1993 which also provides z information with a single hit resolution of 13 μm. Taking into account alignment uncertainties, the vertex detector resolution is 10 μm in $r\phi$ and 15 μm in z for tracks at normal incidence.

A time-of-flight system, consisting of 160 scintillation counters, is mounted outside the coil at a radial distance from the beam of 2.2 m. It measures the arrival time of particles with a precision better than 300 ps and is also used for triggering.

The electromagnetic calorimeter is made of lead glass blocks with a cross-section of 10×10 cm^2 and a depth of 24.6 and $\sim$22 radiation lengths in the barrel and endcap regions, respectively. Since the calorimeter is outside the coil, significant pre-showering occurs. Degradations in position and energy resolution are reduced by a pre-sampler consisting of limited streamer chambers.

Pre-sampler chambers are also used in the endcap part, since here pre-showering occurs in the pressure vessel of the jet chamber. The energy resolution of the lead glass alone is about $0.6\,\%/\sqrt{E/\mathrm{GeV}} \oplus 0.2$, but is degraded at low energies by almost a factor two due to the material in front ; half of the degradation is recoverable by use of the pre-sampler chambers.

The iron of the magnet yoke is segmented into nine layers at radii between 3.4 m and 4.4 m with planes of limited streamer tubes between them and serves as hadron calorimeter and muon filter. In addition to the barrel and end cap parts, also the magnet pole tips are instrumented, thus extending the coverage down to $|\cos\theta| < 0.99$. Read-out is via pads forming projective towers for the energy measurement; strips running the full length of the tubes provide single particle tracking for muons. The pads cover an angular region of $\Delta\phi \times \Delta\theta = 7.5° \times 5°$.

Four layers of large area drift chambers in the barrel and four layers of limited streamer tubes in the endcap regions form the muon detector, which provides two-dimensional coordinates with typical precisions of $\sim$2 mm.

The forward detector system comprises drift chambers in front of a 24 radiation length deep lead-scintillator sandwich with three planes of tube chambers embedded after 4 radiation lengths. This system covers an acceptance between 40 mrad and 150 mrad. For data taking in 1993 and thereafter a high precision tungsten sampling calorimeter with silicon strip readout was added with an acceptance in the range 26 mrad$< \theta <$60 mrad. The high radial precision of this device allowed a luminosity measurement with an experimental systematic error around 0.05 % to be achieved.

5 Electroweak observables

The measurable quantities in e^+e^- annihilation are the production cross-sections for various final states. At LEP, the electrons and positrons in the beam are not polarised; polarisation in the final state is only measurable in the $\tau^+\tau^-$ final state, where the topology of the τ decay serves as spin analyser. The total fermion pair production cross-section at $\sqrt{s} \simeq m_Z$ is dominated by Z exchange; only $\sim$1 % originate from γ exchange; the contribution from the γ–Z interference vanishes at $\sqrt{s} = m_Z$ and is <0.2 % within $\pm$3 GeV of the peak of the resonance. Identifying the produced final state fermions tests the strength of Z couplings to different fermion species; in the Standard Model these depend on the third component of the weak iso-spin and on the electric charge and the weak mixing angle, and are therefore universal in each class of fermions, *i. e.* for neutrinos, charged leptons, up-type quarks and down-type quarks. About 70 % of all produced Z bosons are expected to decay into hadrons, about 10 % into charged leptons and about 20 % decay into invisible neutrinos. The energy dependence of the total cross-section is given by the Breit-Wigner shape of the Z resonance and provides information on the mass and width of the Z. The angle between the direction of flight of the produced fermion and the incoming electron, θ, is another important measurable quantity revealing the structure of the Z couplings to fermions.

"Pseudo-observables" are derived from the measured differential cross-sections by de-convoluting pure QED photonic corrections, and - for hadronic final states - also final state QCD corrections. These pseudo-observables are the mass and total width of the Z, the partial decay widths into different fermion species, and the pure Z contributions to forward-backward asymmetries. The definitions and specialities of the most commonly used pseudo-observables are discussed in the sections below.

5.1 The electroweak cross-section in improved Born approximation

In the improved Born approximation, the structure of the cross-section formula remains unchanged and the Born-level couplings are replaced by effective couplings, which absorb the higher order electroweak corrections and are calculable within the Standard Model.

The electroweak differential cross-section in the collision of unpolarised electrons and positrons, σ_{ew}, for the production of massless fermion pairs, neglecting photonic corrections and QCD final state radiative corrections, can be written in terms of the electric charge, Q_{f}, and the effective couplings, $\hat{g}_v^{\mathrm{f}}$ and $\hat{g}_a^{\mathrm{f}}$, as

$$
\begin{aligned}
\frac{2s}{\pi}\frac{1}{N_c^{\mathrm{f}}}\frac{d\sigma_{\mathrm{ew}}}{d\cos\theta}(\mathrm{e^+e^-}\to\mathrm{f\bar{f}}) \;=\;& \\
&\left|\bar{\alpha}^2 Q^{\mathrm{f}2}\right|^2 (1+\cos^2\theta) \\
&-8\mathrm{Re}\left\{\bar{\alpha}Q^{\mathrm{f}}\chi(s)\left[\underbrace{\hat{g}_v^{\mathrm{e}}\,\hat{g}_v^{\mathrm{f}}}_{\gamma z_s}(1+\cos^2\theta)+2\underbrace{\hat{g}_a^{\mathrm{e}}\,\hat{g}_a^{\mathrm{f}}}_{\gamma z_a}\cos\theta\right]\right\} \\
&+16|\chi(s)|^2\left[\underbrace{(\hat{g}_v^{\mathrm{e}\,2}+\hat{g}_a^{\mathrm{e}\,2})(\hat{g}_v^{\mathrm{f}\,2}+\hat{g}_a^{\mathrm{f}\,2})}_{zz_s}(1+\cos^2\theta)\right. \\
&\left.\qquad+2\cdot\underbrace{4\,\hat{g}_v^{\mathrm{e}}\,\hat{g}_a^{\mathrm{e}}\,\hat{g}_v^{\mathrm{f}}\,\hat{g}_a^{\mathrm{f}}}_{zz_a}\cos\theta\right]
\end{aligned}
$$

with

$$
\chi(s) = \frac{G_{\mathrm{F}} m_{\mathrm{Z}}^2}{8\pi}\frac{s}{s-m_{\mathrm{Z}}^2+is\Gamma_{\mathrm{Z}}/m_{\mathrm{Z}}}\ . \tag{5.1}
$$

N_c^{f} is the number of QCD colour charges of the final state fermions, which is one for leptons and three for quark final states; $\bar{\alpha}$, the value of the electromagnetic coupling constant at the scale of the Z mass, is given by

$$
\bar{\alpha} \equiv \alpha(m_{\mathrm{Z}}) = \frac{\alpha(0)}{(1-\Delta\alpha)}\ ,
$$

where the QED vacuum polarisation correction $\Delta\alpha$ is about 0.060 with a small imaginary contribution.

For simplicity, terms depending on the final state mass, m_{f}, have been neglected in the above formula; they give rise to threshold terms $\sqrt{1-4m_{\mathrm{f}}^2/s}$ multiplying the differential cross-section and to additional coupling terms of order m_{f}^2/s; these are of course included in the computations performed to extract Z parameters from the measured cross-sections. For e^+e^- final states additional t-channel diagrams and the s–t interference have to be taken into account. After their subtraction equation 5.1 for the differential cross-section also holds for $e^+e^- \to e^+e^-$.

The formula given above is valid after the application of photonic corrections to the measured cross-sections. Technically, this is achieved by convolution of the pure electroweak cross-section with the radiator function according to equation 2.4 . The corrections include final state radiation, initial-state leptonic and hadronic pair production, initial-final-state QED interference and finally the dominant contribution from initial-state radiation. Various calculations were compared recently [17] and found to agree within 0.03 % for the predicted total cross-section at $\sqrt{s} = m_Z$ and within about 0.1 % $\pm$3 GeV away from the peak of the resonance.

The above description of the differential cross-section close to the Z resonance is valid under quite general assumptions: fermion pair annihilation and production in the s channel are mediated by a massless vector boson with unique vector couplings depending on the fermion charges only, and a massive vector boson with both axial-vector and vector couplings to fermions. It provides the definitions of the effective Z couplings, which can thus be extracted from the measured cross-sections and then are compared with the predictions of the Standard Model.

5.2 Total cross-section and forward-backward asymmetry

The angular dependence of the various terms in equation 5.1 is either of the type $\cos\theta$ or $(1+\cos^2\theta)$, which multiply certain combinations of couplings. The first term is from γ exchange and has an angular dependence of $(1+\cos^2\theta)$; the second term, containing the combinations of couplings labelled γz_s and γz_a, from γ–Z interference, disappears at $\sqrt{s} = m_Z$; the third term with the combinations zz_a and zz_s is the most important one and arises from Z exchange. The terms even in $\cos\theta$ contribute to the total cross-section given by

$$\sigma_{tot} = \int_{-1}^{1} \frac{d\sigma}{d\cos\theta}\, d\cos\theta\ ,$$

whereas $\cos\theta$-odd terms integrate to zero in the total cross-section but contribute to the forward-backward asymmetry, defined as

$$A_{\mathrm{fb}} = \frac{\int_0^1 \frac{d\sigma}{d\cos\theta}\, d\cos\theta - \int_{-1}^{0} \frac{d\sigma}{d\cos\theta}\, d\cos\theta}{\sigma_{tot}}\ .$$

In order to extract all the combinations of couplings involved, it is therefore sufficient to measure the energy dependence of the total production cross-sections and of the forward-backward asymmetries for the different final states into which the Z decays.

The total cross-section depends on photon exchange, the γz_s term from the interference and the zz_s term from the Z, where the latter is by far dominating. The forward-backward asymmetry at the pole, $\sqrt{s} = m_Z$, depends on the combination of couplings given essentially by zz_a/zz_s, and its energy dependence arises from the γz_a term in the interference contribution.

5.2.1 The line shape

For the energy dependence of the Z contribution to the total cross-section, the "line shape", one obtains by integration of the relevant part of equation 5.1 ,

$$\sigma_{\mathrm{ew,f\bar{f}}}(s) = \sigma_{\mathrm{f}}^0 \frac{s\Gamma_{\mathrm{Z}}^2}{(s-m_{\mathrm{Z}}^2)^2 + s^2\Gamma_{\mathrm{Z}}^2/m_{\mathrm{Z}}^2}\ . \qquad (5.2)$$

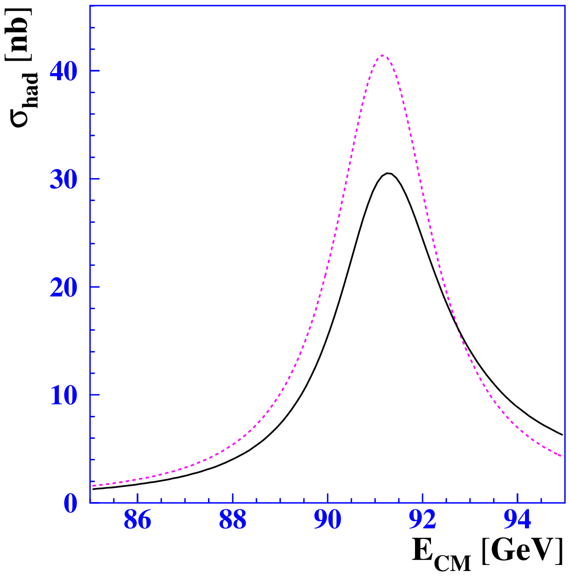

Figure 5.1: *Hadronic line shape and radiative corrections, calculated with the computer code ZFITTER [25] and with the choice of parameters m_{Z}=91.19* GeV, *m_{t}=175* GeV, *m_{H} =300* GeV *and α_s=0.118. The solid line shows the physical cross-section, the dashed line shows the pure electroweak cross-section obtained before applying photonic corrections.*

Here, σ_{f}^0 is the cross-section for production of the final state $\mathrm{f\bar{f}}$ at the pole, which can also be expressed in terms of partial decay widths,

$$\sigma_{\mathrm{f}}^0 = \frac{12\pi}{m_{\mathrm{Z}}^2} \frac{\Gamma_{\mathrm{e}}\Gamma_{\mathrm{f}}}{\Gamma_{\mathrm{Z}}^2}\ . \qquad (5.3)$$

The partial decay width, Γ_{f}, of the Z into a $\mathrm{f\bar{f}}$ final state in terms of the effective couplings is

$$\Gamma_{\mathrm{f}} = \frac{G_{\mathrm{F}} m_{\mathrm{Z}}^3}{6\pi\sqrt{2}} N_c^{\mathrm{f}} (\hat{g}_v^{\mathrm{f}\,2} + \hat{g}_a^{\mathrm{f}\,2}) \cdot (1 + \delta_{QED} + \delta_{QCD})\ . \qquad (5.4)$$

Note that here final state QED and QCD corrections, $\delta_{QED} = 3\alpha(m_{\mathrm{Z}})\ Q^{\mathrm{f}^2}/4\pi$ and δ_{QCD} as illustrated by equation 2.5, are explicitly included in the definition in order to obtain the physical width.

Contrary to the leptonic case, different $\mathrm{q\bar{q}}$ flavours in the final states cannot be completely separated experimentally, and therefore it is useful to take an inclusive approach and to define the hadronic decay width, Γ_{h}, as the sum of the decay widths to all quark flavours. The corresponding parametrisation of the energy dependence of the cross-section for $\mathrm{q\bar{q}}$ production, the hadronic line shape, is then obtained by substituting $\Gamma_{\mathrm{f}} = \Gamma_{\mathrm{h}}$ in equation 5.3 , *i.e.* σ_{f}^0 in equation 5.2 becomes σ_{h}^0.

For the extraction of the three parameters m_{Z}, Γ_{Z} and σ_{h}^0, contributions from γ exchange and from γ–Z interference have small effects and are set to their Standard Model values; the same is true for the imaginary parts of the photon vacuum polarisation and for imaginary parts of the couplings. This implies some Standard Model dependence, in particular, of the extracted Z mass (see also section 5.3).

The predicted hadronic line shape and the effect of photonic corrections on it is illustrated in Figure 5.1 .

5.2.2 Leptonic line shape and forward-backward asymmetry

The energy dependence of the cross-sections for various final states is identical, the only difference is the cross-section at the pole, σ^0_{f}. The case $\mathrm{e^+e^-} \to \mathrm{e^+e^-}$ is special due to the presence of $\mathrm{e^+e^-}$ scattering by photon exchange in the t-channel. This leads to additional contributions to the cross-section, as is shown in Figure 5.2 . The Z mass, width and couplings to electrons are extracted after subtracting the t-channel and s–t interference contributions from the total electroweak cross-section.

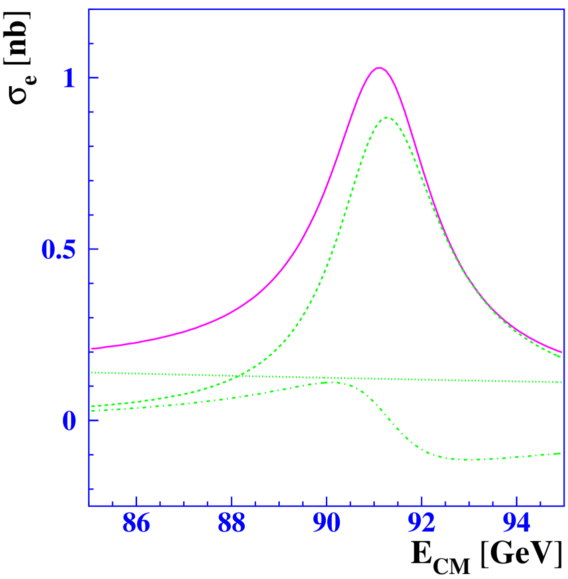

Figure 5.2: *The electroweak cross-section for* $\mathrm{e^+e^-} \to \mathrm{e^+e^-}$ *before pure QED corrections (full line); since the* t*-channel cross-section is divergent at small angles, the angular acceptance was restricted to* $|\cos\theta| < 0.7$*. The dashed, dotted and dashed-dotted lines show separately the s- and t-channel and the s–t interference contributions, respectively.*

Cross-sections are determined by normalisation to a reference reaction, the t-channel dominated scattering of $\mathrm{e^+e^-}$ at small angles ("Bhabha scattering"). Therefore all pole cross-sections have a common contribution to their experimental errors from the statistical and experimental as well as theoretical systematic errors in this reference reaction. It therefore became common practice to use instead the ratios of pole cross-sections defined as

$$R_{\mathrm{f}} = \frac{\sigma^0_{\mathrm{h}}}{\sigma^0_{\mathrm{f}}} \equiv \frac{\Gamma_{\mathrm{h}}}{\Gamma_{\mathrm{f}}} \qquad \text{for } \mathrm{f\bar{f}} = \mathrm{e^+e^-}, \mu^+\mu^-, \tau^+\tau^- \, . \tag{5.5}$$

The experimental errors on R_{e}, R_μ and R_τ are entirely dominated by the total error on the lepton cross-sections, with small common errors of about 20 % from the normalisation to the number of hadrons.

The measurements of the forward-backward asymmetries can be condensed into one single parameter per lepton species in the final state, the pole asymmetry $A^{0,\mathrm{f}}_{\mathrm{fb}}$, which is given by the following combinations of effective couplings

$$A^{0,\mathrm{f}}_{\mathrm{fb}} \equiv \frac{3}{4}\mathcal{A}_{\mathrm{e}}\mathcal{A}_{\mathrm{f}} \tag{5.6}$$

with

$$\mathcal{A}_{\mathrm{f}} \equiv \frac{2\,\hat{g}^{\mathrm{f}}_v\,\hat{g}^{\mathrm{f}}_a}{\hat{g}^{\mathrm{f}\,2}_v + \hat{g}^{\mathrm{f}\,2}_a} \, . \tag{5.7}$$

$A^{0,\mathrm{f}}_{\mathrm{fb}}$ corresponds to the asymmetry at $\sqrt{s} = m_{\mathrm{Z}}$, where the interference term vanishes. Note that, contrary to the peak cross-sections, this definition of the peak asymmetry does not contain QED nor QCD final state corrections.

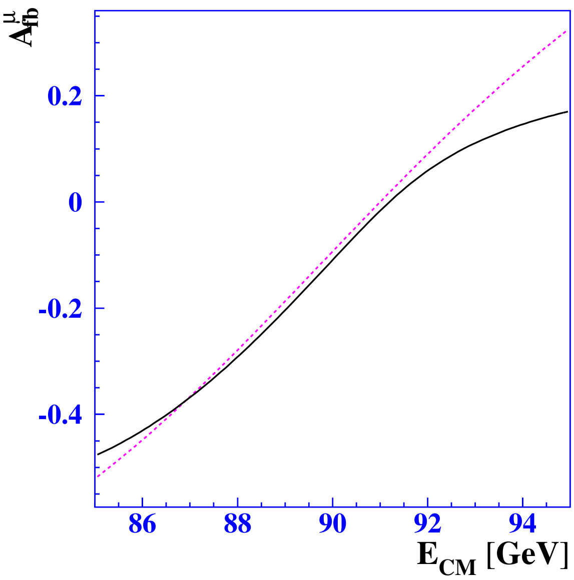

Figure 5.3: *Energy dependence of the leptonic (=$\mu^+\mu^-$) forward-backward asymmetry and radiative corrections. The solid line shows the physical asymmetry, the dashed line shows the pure electroweak asymmetry before applying radiative corrections.*

The energy dependence and the effect of photonic corrections on the forward-backward asymmetry is shown in Figure 5.3 . From the comparison between different calculations preformed recently [17] an uncertainty from QED de-convolution of about ± 0.0002 on the peak asymmetry is inferred.

In $e^+e^- \to e^+e^-$, t-channel and s–t interference contributions lead to a significant change of the asymmetry and its energy dependence. Its importance is seen in Figure 5.4.

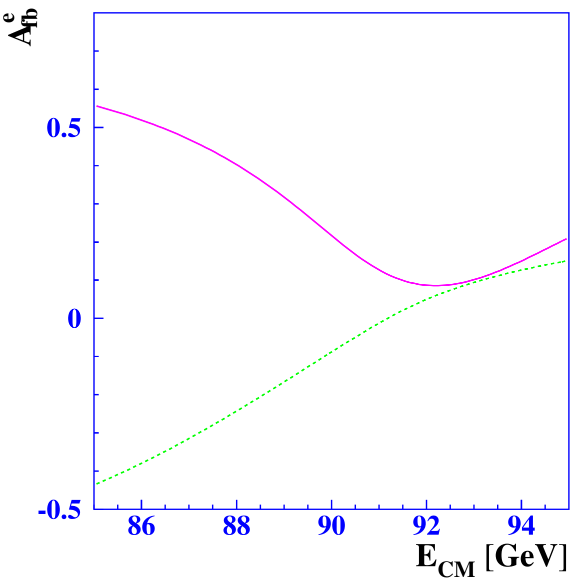

Figure 5.4: *The forward-backward asymmetry for* $e^+e^- \to e^+e^-$ *before pure QED corrections (full line), for an angular acceptance* $|\cos\theta| < 0.7$. *The dashed line shows the s-channel contribution for comparison.*

The γ–Z interference term of equation 5.1 in the lepton case is dealt with by taking the couplings appearing in the γz_s and γz_a terms equal to the couplings in the zz terms, usually assuming universality of the couplings between the initial and final state leptons, *i. e.* $\hat{g}_v^e\,\hat{g}_v^f \equiv \hat{g}_v^{\ell\,2}$ and $\hat{g}_a^e\,\hat{g}_a^f \equiv \hat{g}_a^{\ell\,2}$. Again, imaginary parts of the photon vacuum polarisation and of the effective couplings are set to their Standard Model values and not included in the definition of $A_{fb}^{0,\ell}$.

5.3 Model-independent analysis of the Z resonance

The parametrisation of the Z resonance presented in the above sections still depend on some Standard Model assumptions on the γ–Z interference. The OPAL collaboration suggested in their analysis of cross-sections and asymmetries to treat the four combinations of couplings labelled $\gamma z_{a,s}$ and $zz_{a,s}$ in equation 5.1 as independent parameters in the fit [38], allowing to test that the couplings derived from interference contributions are identical to the couplings from the pole cross-sections and asymmetries.

In a more rigorous, completely model-independent approach a S-matrix ansatz [39] was suggested to describe the cross-section without any reference to the Standard Model other than QED and QCD corrections.

The parametrisation for the total ("tot") and difference between forward and backward ("fb") cross-sections, before photonic corrections, is given by

$$\sigma^f_{A,\mathrm{ew}}(s) = \frac{4}{3}\pi\alpha(0)^2\left[\frac{g^f_A}{s} + \frac{j^f_A(s-\overline{m_Z}^2) + s\,r^f_A}{(s-\overline{m_Z}^2)^2 + \overline{m_Z}^2\,\overline{\Gamma_Z}^2}\right]$$

$$\text{for } A = \text{tot or fb};$$

$$A^f_{\mathrm{fb,ew}}(s) = \frac{3}{4}\frac{\sigma_{\mathrm{fb,ew}}(s)}{\sigma_{\mathrm{tot,ew}}(s)}. \qquad (5.8)$$

Note that here a standard Breit-Wigner denominator, *i.e* without s-dependent width, is used, leading to a different definition of the Z mass and width. m_Z and Γ_Z are related to $\overline{m_Z}$ and $\overline{\Gamma_Z}$ by a multiplicative factor,

$$\begin{aligned} m_Z &= \overline{m_Z}\sqrt{1+\frac{\overline{\Gamma_Z}^2}{\overline{m_Z}^2}} &\simeq& \overline{m_Z} + 34.1\ \mathrm{MeV} \\ \Gamma_Z &= \overline{\Gamma_Z}\sqrt{1+\frac{\overline{\Gamma_Z}^2}{\overline{m_Z}^2}} &\simeq& \overline{\Gamma_Z} + 0.9\ \mathrm{MeV}. \end{aligned} \qquad (5.9)$$

g_{tot} describes photon exchange and is simply given by QED as $g_{\mathrm{tot}} = Q^{f\,2}/|1-\Delta\alpha|^2$, while g_{fb} vanishes.

The other parameters, j_{tot} and j_{fb} respectively r_{tot} and r_{fb}, describe the Z and γ–Z interference contributions to the total and the forward – backward cross-sections. Note that here corrections arising from the running of α are included in the definition of the parameters. By comparison of equation 5.8 with equation 5.1 they are related to the combinations of couplings labelled $zz_{s,a}$ and $\gamma z_{s,a}$ and are thus predicted in the framework of the Standard Model.

Of special importance is the parameter $j^{\mathrm{had}}_{\mathrm{tot}}$, which shifts the position of the peak of the resonance and therefore is strongly correlated with the Z mass. A determination of $j^{\mathrm{had}}_{\mathrm{tot}}$ tests the validity of the standard approach which sets this term to its Standard Model value. A sufficiently precise determination of $j^{\mathrm{had}}_{\mathrm{tot}}$ requires cross-section measurements below and above the Z peak, as performed by the TOPAZ experiment at KEK [40], at a centre-of-mass energy of about 60 GeV, and at LEP II at energies of 133 GeV and >160 GeV.

5.4 Inclusive quark forward-backward asymmetry

Since quarks fragment into jets of hadrons, the forward-backward asymmetries of $q\bar{q}$ final states cannot in general be directly measured.

Instead, one uses the average charge in the forward and backward hemispheres, given by $\left\langle Q_F^{f,0}\right\rangle = Q^f A^f_{fb}$ and $\left\langle Q_B^{f,0}\right\rangle = -Q^f A^f_{fb}$.

The "charge asymmetry" is defined as the difference between the charges in the forward and backward hemispheres. For an inclusive sample of $q\bar{q}$ final states composed of the natural mixture of quark flavours from Z decay this is given at parton level by

$$\left\langle Q_{\mathrm{fb}}^{\mathrm{q},0}\right\rangle = \sum_{\mathrm{f}} 2Q^{\mathrm{f}}\frac{\Gamma_{\mathrm{f}}}{\Gamma_{\mathrm{h}}}A_{\mathrm{fb}}^{\mathrm{f}}\,,$$

where the sum runs over the quark flavours f = u, d, c, s and b. Since up-type quarks and down-type quarks have the same asymmetry but opposite charges the charge asymmetry in the inclusive hadron sample is reduced.

In practice, the fragmentation process dilutes the observed hemisphere charges. An estimator for the quark charge is derived from the sums of momentum-weighted track charges in a hemisphere. Defining $\delta^{\mathrm{f}} = \left\langle Q^{\mathrm{f}} - Q^{\bar{\mathrm{f}}}\right\rangle$ as the average observed charge difference between the quark and anti-quark hemispheres the measured charge asymmetry becomes

$$\langle Q_{\mathrm{fb}}^{\mathrm{q}}\rangle = \sum_{\mathrm{f}} \delta^{\mathrm{f}}\frac{\Gamma_{\mathrm{f}}}{\Gamma_{\mathrm{h}}}A_{\mathrm{fb}}^{\mathrm{f}}\,. \tag{5.10}$$

The method relies strongly on Monte Carlo simulations of the fragmentation process and hadron decays.

$\left\langle Q_{\mathrm{fb}}^{\mathrm{q}}\right\rangle$ depends on the product of the four couplings in the asymmetry term of equation 5.1 and is mostly sensitive to the leptonic effective weak mixing angle, $\sin^2\theta_{\mathrm{W}}^{\mathrm{eff},\ell}$, through the vector coupling of the initial state electrons, $\hat{g}_v^{\mathrm{e}}$. Since the numerical value of $\hat{g}_v^{\mathrm{e}}$ is much smaller than the vector couplings of quarks, $\hat{g}_v^{\mathrm{e}}$ is about five or ten times more sensitive to a change in $\sin^2\theta_{\mathrm{W}}^{\mathrm{eff}}$ than the vector coupling of up-type or down-type quarks, respectively.

5.5 Heavy quarks

Distinguishing the final state quark flavour for heavy quarks, $\mathrm{c\bar{c}}$ and $\mathrm{b\bar{b}}$, is possible by tagging their decays and relatively long life times. Commonly, one uses the ratios of partial decay widths,

$$\begin{aligned} R_{\mathrm{b}} &= \tfrac{\Gamma_{\mathrm{b\bar{b}}}}{\Gamma_{\mathrm{h}}} \\ R_{\mathrm{c}} &= \tfrac{\Gamma_{\mathrm{c\bar{c}}}}{\Gamma_{\mathrm{h}}}\,. \end{aligned} \tag{5.11}$$

In these ratios, propagator corrections cancel. The special $\mathrm{Z\text{–}b\bar{b}}$ vertex corrections arising from the large b coupling to the top quark via the $\mathrm{W}^{\pm}$ boson therefore manifest themselves in R_{b}.

The pole asymmetries are given analogous to the leptonic case by

$$\begin{aligned} A_{\mathrm{fb}}^{0,\mathrm{c}} &\equiv \tfrac{3}{4}\mathcal{A}_{\mathrm{e}}\mathcal{A}_{\mathrm{c}} \\ A_{\mathrm{fb}}^{0,\mathrm{b}} &\equiv \tfrac{3}{4}\mathcal{A}_{\mathrm{e}}\mathcal{A}_{\mathrm{b}}\,. \end{aligned} \tag{5.12}$$

Contrary to the lepton case, the direction of the produced fermion is diluted by gluon radiation and fragmentation in quark final states, and therefore QCD corrections are necessary to obtain the pole asymmetries from the measured ones. The directions of the primary quarks are usually inferred from the thrust axis of the event, leading to additional corrections; this will be discussed in more detail in section 8.3 .

The sensitivity of the heavy quark asymmetries to the effective weak mixing angle arises mostly from $\mathcal{A}_{\mathrm{e}}$, because its dependence on the weak mixing angle is the strongest due to the small value of the leptonic vector coupling. To be quantitative, the sensitivity, $\partial\mathcal{A}_{\mathrm{f}}/\partial\sin^2\theta_{\mathrm{W}}^{\mathrm{eff}}$, is about -7.9, -3.5 and -0.6 for f = ℓ, c and b final states, respectively, if a value of $\sin^2\theta_{\mathrm{W}}^{\mathrm{eff}} = 0.23$ is assumed. In addition, the b-quark asymmetry, proportional to $\mathcal{A}_{\mathrm{e}}\mathcal{A}_{\mathrm{b}}$, is expected to be about six times larger than the electron asymmetry and 1.5 times larger than the c-quark asymmetry. Therefore, for a given value of the absolute precision in the measured b-quark asymmetry, the relative precision is large. For these reasons, the value derived from the b-quark asymmetry is the most precise determination of the effective leptonic weak mixing angle among all LEP observables.

5.6 Tau lepton polarisation

Parity violation in the weak interaction causes all final states from Z decay to be longitudinally polarised; only for τ leptons this can be measured using the subsequent parity-violating weak decays of the τ as a polarimeter. The polarisation is defined in terms of the cross-section for the production of right-handed τ^-, $\sigma_{\mathrm{r}} = \sigma(\mathrm{Z}\to\tau_{\mathrm{r}}^-\tau_{\mathrm{l}}^+)$, and left-handed τ^-, $\sigma_{\mathrm{l}} = \sigma(\mathrm{Z}\to\tau_{\mathrm{l}}^-\tau_{\mathrm{r}}^+)$, from the interactions of the unpolarised $\mathrm{e}^+\mathrm{e}^-$ in the LEP beams,

$$\mathcal{P}_\tau = \frac{\sigma_{\mathrm{r}}-\sigma_{\mathrm{l}}}{\sigma_{\mathrm{r}}+\sigma_{\mathrm{l}}}\,. \tag{5.13}$$

The polarisation of the τ leptons from $\mathrm{Z}\to\tau^+\tau^-$ decays at $\sqrt{s} = m_{\mathrm{Z}}$ is given in the improved Born approximation by

$$\mathcal{P}_\tau(\cos\theta) = -\frac{\mathcal{A}_\tau(1+\cos^2\theta)+2\mathcal{A}_{\mathrm{e}}\cos\theta}{1+cos^2\theta+2\mathcal{A}_{\mathrm{e}}\mathcal{A}_\tau\cos\theta}\,. \tag{5.14}$$

This simplifies to the average τ polarisation over all angles,

$$\langle\mathcal{P}_\tau\rangle\,(s=m_{\mathrm{Z}}^2) = \frac{-2\,\hat{g}_v^\tau\,\hat{g}_a^\tau}{(\hat{g}_v^{\tau\,2}+\hat{g}_a^{\tau\,2})} = -\mathcal{A}_\tau\,. \tag{5.15}$$

Note that the polarisation, unlike the charge forward-backward asymmetry, is independent of the effective vector and axial-vector couplings of the initial state electrons and gives the sign of the ratio of couplings $\hat{g}_v^\tau\,/\,\hat{g}_a^\tau$.

Another observable from $\mathrm{Z}\to\tau^+\tau^-$ decays is the τ polarisation forward-backward asymmetry,

$$A_{\mathrm{fb}}^{\mathcal{P}_\tau} = \frac{\mathcal{P}_{\tau,forw.}-\mathcal{P}_{\tau,backw.}}{\mathcal{P}_{\tau,forw.}+\mathcal{P}_{\tau,backw.}}\,, \tag{5.16}$$

where $\mathcal{P}_{\tau,forw.}$ and $\mathcal{P}_{\tau,backw.}$ are the average polarisations of forward ($0° < \theta < 90°$) and backward ($90° < \theta < 180°$) going τ^-. Expressed in terms of couplings, this is given by

$$A_{\mathrm{fb}}^{\mathcal{P}_\tau}(s=m_{\mathrm{Z}}^2) = -\frac{3}{2}\frac{\hat{g}_v^{\mathrm{e}}\,\hat{g}_a^{\mathrm{e}}}{(\hat{g}_v^{\mathrm{e}\,2}+\hat{g}_a^{\mathrm{e}\,2})} = -\frac{3}{4}\mathcal{A}_{\mathrm{e}} \tag{5.17}$$

and is independent of the final state couplings. Further details on τ polarisation and QED radiative corrections are discussed, *e. g.*, in reference [41] .

5.7 Observables with longitudinally polarised electrons

The same parity violating effect leading to longitudinal polarisation in the Z final states also leads to a dependence of cross-sections on the helicity states of the initial state electrons. This can be studied with longitudinally polarised electrons in the initial state, which are available at the linear collider at Stanford (SLC). Contrary to the unpolarised case, the combinations of couplings $\mathcal{A}_e$ or $\mathcal{A}_f$ of the initial or final state particles only enter linearly into these observables and therefore the relative sign of the ratio of the vector and axial-vector couplings can be determined.

For a given average polarisation level $\mathcal{P}_e$ of the electrons, the left-right cross-section asymmetry, A_{lr}, is given by

$$A_{lr} = \frac{1}{\mathcal{P}_e} \frac{\sigma_l - \sigma_r}{\sigma_l + \sigma_r} ; \tag{5.18}$$

where σ_l and σ_r are the cross-sections for left-handed and right-handed electrons.

Considering pure Z exchange, this depends only on the initial state coupling constants,

$$A_{lr}(s = m_Z^2) = \mathcal{A}_e . \tag{5.19}$$

The forward-backward asymmetries can also be measured with polarised electron beams, leading to the definition of the polarised forward-backward asymmetry,

$$A_{fb,lr} = \frac{1}{\mathcal{P}_e} (A_{fb,l} - A_{fb,r}) . \tag{5.20}$$

The contribution from Z exchange is

$$A_{fb,lr}(s = m_Z^2) = \frac{3}{4} \mathcal{A}_f , \tag{5.21}$$

which depends on the final state couplings only.

5.8 Other important observables

The direct measurement of the mass of the top quark [15] at the Tevatron collider at Fermilab by the experiments CDF and DØ is of great importance, since, firstly, the comparison of the directly measured value with the one obtained from virtual top quark loops is a crucial test of the Standard Model. Secondly, only with the top quark mass as an input parameter electroweak observables become sensitive to the mass of the Higgs boson.

Direct measurements of the W boson mass, m_W [42], at the Tevatron by the CDF and DØ experiments and by the four LEP experiments at LEP II provide another important check, because the W mass is predictable from electroweak observables and the Z mass.

Measurements of neutrino nucleon scattering [43] can directly be translated into a measurement of the weak mixing angle, $\sin^2\theta_W = 1 - m_W^2/m_Z^2$, which is related to the effective weak mixing angle by electroweak corrections, see equation 2.8 .

5.9 Sensitivity of the observables to electroweak corrections

Within the Standard Model all observables described above can be calculated. The dominant electroweak corrections arise from the top quark due to the large mass splitting in the b and t quark iso-doublet. Although the top quark mass is by now measured with a precision of several GeV, it is nevertheless interesting to identify the variables which offer the most significant information on the top quark mass from virtual loops. Figure 5.5 shows the change of each observable, normalised to its present experimental error, which is induced by a change of the top quark mass by 1 GeV. Standard Model predictions were calculated with ZFITTER, and the experimental errors can be found in Table 10.1 .

Of primary interest is of course the last free parameter of the Standard Model, the mass of the Higgs boson. The sensitivity of electroweak observables to the Higgs mass is shown in Figure 5.6 , which indicates the change of each of the measured observables, normalised to its present experimental error, which is caused by a change of

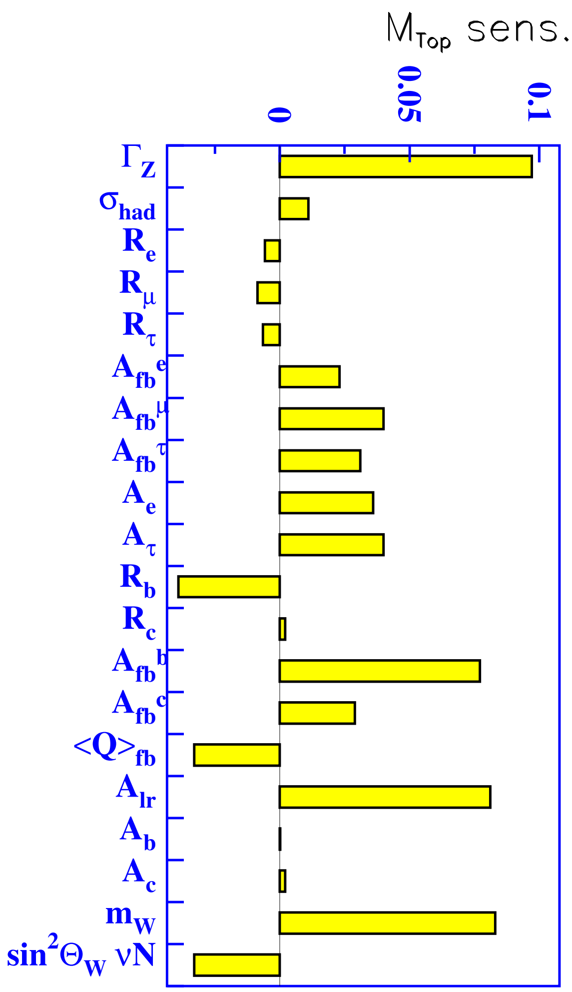

Figure 5.5: *The sensitivity of electroweak observables to the value of the top quark mass.*

$\log_{10}(m_{\rm H}/\text{GeV})$ by one unit. Large changes in $m_{\rm H}$ cause relatively moderate changes of the measured observables; *e. g.* a change of $m_{\rm H}$ from 100 GeV to 1000 GeV changes $\Gamma_{\rm Z}$, $A_{\rm fb}^{0,\rm b}$ or A_{lr} by only about three times their present errors.

The apparently dominant sensitivity of the total Z width to both $m_{\rm t}$ and $m_{\rm H}$ is weakened because of its dependence on the strong coupling constant, which enters through the hadronic width. This leaves the asymmetry-type measurements $A_{\rm fb}^{0,\rm b}$ and $A_{\rm lr}$ as the most sensitive observables.

Comparing the sensitivities of the various observables to the top quark and Higgs boson masses it becomes obvious that the effects of electroweak corrections on $m_{\rm H}$ and $m_{\rm t}$ are in most cases strongly anti-correlated, and it is therefore difficult to disentangle them. Some differences, however, are notable: $R_{\rm b}$ has some sensitivity to $m_{\rm t}$, but is largely insensitive to $m_{\rm H}$. The W boson mass is sensitive to both $m_{\rm t}$ and $m_{\rm H}$. The ratios of decay widths $\sigma_{\rm h}^0$, $R_{\rm e}$, R_μ and R_τ exhibit a positively correlated dependence on $m_{\rm t}$ and $m_{\rm H}$. However, these also depend on the value of the strong coupling constant. If, instead, the leptonic decay width, Γ_ℓ, is extracted from these measurements in combination with the total Z width, according to equations 5.3 and 5.5, one obtains a determination of the effective ρ parameter, independent of the strong coupling constant; Γ_ℓ depends dominantly on the top quark mass. Relative to this the asymmetry-type measurements show a more pronounced dependence on the Higgs boson and are therefore the most significant observables for a determination of the mass of the Higgs boson.

A comparison of the two figures also shows that a direct measurements of the top quark mass with a precision of a few GeV permits important conclusions on the Higgs sector to be drawn from the presently available electroweak measurements.

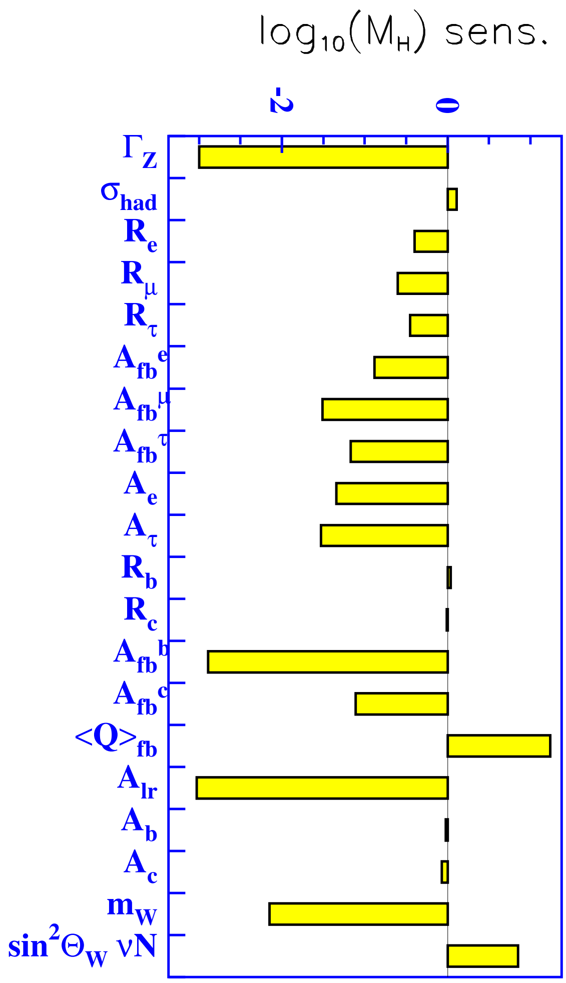

Figure 5.6: *The sensitivity of electroweak observables to the value of the Higgs boson mass.*

6 Line shape and asymmetry measurements

Measurements of the observables introduced in the previous chapter were performed by the four experiments at LEP and by the SLD collaboration. These will be described in some detail here and in the next two chapters.

Many results are not yet final, and almost all averages are therefore also still preliminary. However, most of the analyses discussed here have reached a high level of maturity and use the full data sets available; therefore only small modifications to the drawn conclusions are expected in the future.

The experiments extracted the pseudo-observables m_{Z}, Γ_{Z}, σ_{h}^{0}, R_{ℓ} and $A_{\mathrm{fb}}^{0,\ell}$ for the three charged lepton species, $\ell = \mathrm{e}, \mu, \tau$, by fitting the parametrisation illustrated by equation 5.1 to the hadronic and leptonic cross-sections and leptonic forward-backward asymmetries measured at different energies around the Z resonance [44, 45].

The approximate centre-of-mass energies and integrated luminosities used in the analyses were summarised already in Table 3.2, and the numbers of recorded events are shown in Table 6.1 . The data set is dominated by the high-statistics run performed at the peak energy point in 1994 and the two energy scans around the Z resonance in 1993 and 1995.

The integrated luminosity used by the experiments is smaller than the luminosity delivered by LEP, since all experiments apply stringent quality criteria on data to be used in the analyses. These criteria include clean beam conditions and full functionality of the essential parts of the detectors: luminometer, central tracking system including the magnet, electromagnetic and hadron calorimeters and the muon chambers. In addition, periods with high machine induced background and read-out dead-times and data taking inefficiencies of the experiments reduced the usable integrated luminosity.

year	A	D	L	O	all
			$\mathrm{q\bar{q}}$		
'90/91	451	357	416	454	1678
'92	680	697	678	733	2788
'93	640	677	646	646	2609
'94	1654	1241	1307	1524	5726
'95	739	584	311	344	1978
total	4164	3556	3358	3701	14779
			$\ell^+\ell^-$		
'90/91	55	36	40	58	189
'92	82	70	58	88	298
'93	78	74	64	82	298
'94	190	129	127	184	630
'95	80	67	28	42	217
total	485	376	317	454	1638

Table 6.1: *The event statistics in units of* 10^3 *used for the analysis of the* Z *line shape and lepton forward-backward asymmetries by the experiments ALEPH (A), DELPHI (D), L3 (L) and OPAL (O). Note that numbers in 1993 and thereafter are still preliminary.*

6.1 Cross-section measurements

Measurements of the cross-sections for Z decays into fermion pairs $\mathrm{f\bar{f}}$ require an unambiguous identification of final state particles, good control of the experimental acceptance and detection efficiency, ε_{ac}, and a precise knowledge of the integrated luminosity, $\int L$. The cross-section, $\sigma_{\mathrm{f\bar{f}}}$, is obtained by dividing the total number of produced fermion pair events by the integrated luminosity. The produced number of events is given by the number of candidate events, $N_{\mathrm{f\bar{f}}}^{cand}$, after subtraction of the expected number of background events, $N_{\mathrm{f\bar{f}}}^{bkg}$. The integrated luminosity was determined from the number of identified $\mathrm{e^+e^-} \rightarrow \mathrm{e^+e^-}$ events scattered at small angles; this well-known QED process is dominated by t-channel photon exchange with only very small contributions from Z exchange. The integrated luminosity is given by the number of identified Bhabha events within a well defined acceptance after normalisation to the calculated cross-section for small-angle Bhabha scattering.

The analysis of the experiments starts from a luminosity weighted average energy for events taken at approximately the same energy, referred to as an "energy point". The r.m.s spread of the average energies contributing to one energy point is typically $\sim$10 MeV.

With these definitions, the cross-section at the average energy E_i is given by

$$\sigma(E_i) = \frac{N_{\mathrm{f\bar{f}}}^{cand}(E_i) - N_{\mathrm{f\bar{f}}}^{bkg}(E_i)}{\varepsilon_{ac}(E_i)} \, \frac{1}{\int L\,(E_i)} \,. \qquad (6.1)$$

In principle, the determination of the integrated luminosity is important to all cross-section measurements, hadronic as well as leptonic decay channels of the Z. However, the uncertainty introduced by the luminosity determination is correlated between all of these channels. In the standard parametrisation, as introduced in the previous chapter, the number of observed leptons is normalised to the number of hadrons, and therefore, in practice, only the hadronic cross-section is affected by uncertainties from the luminosity determination.

6.1.1 Determination of the luminosity

The measurement of the luminosity relies on a very efficient detection of electrons scattered at small angles within a well defined acceptance. This is best achieved with calorimetric measurements, which also have the advantage that final state photons close to the scattered electrons or positrons are naturally included. The fiducial region should be as close as possible to the beam line to increase the statistics and reduce the Z contribution.

The Bhabha cross-section is strongly peaked towards small scattering angles, given in lowest order by

$$\begin{aligned} \sigma_{\mathrm{Bh}} &\simeq \frac{1040\ \mathrm{nb\,GeV}^2}{s}\left(\frac{1}{\theta^2_{min}}-\frac{1}{\theta^2_{max}}\right) \\ &\propto Z^2_{det}\left(\frac{1}{R^2_{min}}-\frac{1}{R^2_{max}}\right), \end{aligned} \tag{6.2}$$

where $\theta_{min,max}$ are the minimal and maximal accepted scattering angles, $R_{min,max}$ are the corresponding inner and outer radii of the detectors, and Z_{det} is the distance of the luminosity detectors from the interaction point.

As the basic element of the luminosity determination all experiments use electromagnetic calorimeters with cylindrical symmetry about the beam axis, with typical inner and outer radii of the fiducial acceptance, measured from the beam axis, of $\sim$7 cm and $\sim$15 cm, respectively, placed about 2.5 m away from the interaction point (see Table 4.1 for details).

The statistical precision of the LEP I data imposes a systematic error on the luminosity measurement below 0.1 % . This requires a precision on the geometrical alignment of the order of $\pm 20\ \mu$m, $\pm 100\ \mu$m and ± 1 mm on R_{min}, R_{max} and Z_{det}, respectively.

Longitudinal and transverse displacements of the interaction point position also affect the luminosity measurement; their effect is minimised by an asymmetric definition of the acceptance, loose on one side and tighter on the other. The tight-loose and loose-tight selections are performed concurrently, and the results are averaged. This procedure also has the advantage of including events with photon radiation, thus making the measurement more inclusive and the cross-section calculation more reliable.

Background arises from random coincidences between off-momentum electrons and positrons, which are lost from the beam and hit the detectors on both sides. This background depends on the operating conditions of LEP and varied from year to year. Relatively soft cuts on the minimal energy and on the difference in azimuthal angle, ϕ, of the observed showers allowed to suppress this background efficiently. The cleanliness of the luminosity signal is demonstrated in Figure 6.1, which shows a scatter plot of the particle energies recorded by the luminosity calorimeters on both sides. Background events at energies much lower than the beam energy cluster in the lower left corner of the plot. In most events the two recorded energies are close to the beam energy, shown by the black region in the upper right corner. The vertical and horizontal tails towards low energies arise from events with one hard radiated photon. The region between the signal and the background is populated by double-radiative events.

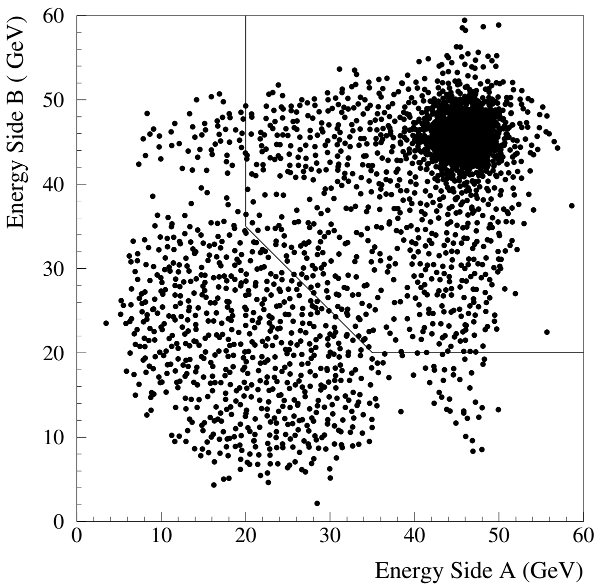

Figure 6.1: *Scatter plot of the energies recorded on the left and right side by the ALEPH luminosity detectors.*

The theoretical cross-section within the fiducial acceptance, $\sigma^{th}_{\mathrm{Bh}}$, provides the normalisation. The calculations include the small contribution from the Z at low angles and from the γ–Z interference; multi-photon radiation is taken into account based on an exponentiated $O(\alpha)$ calculation including the majority of the leading logarithmic and part of the next to leading logarithmic terms of $O(\alpha^2)$. The theoretical Bhabha cross-section also depends on details of the experimental acceptance and the cuts used to select pairs of scattered electrons in the calorimeters. Therefore, Monte Carlo event generators are needed. The uncertainty of the present version of the generator BHLUMI [46] is estimated to be $\Delta\sigma^{th}_{Bh}/\sigma^{th}_{Bh} = \pm 0.11$ % [47]; it is dominated by missing leading logarithmic photonic $O(\alpha^2)$ corrections.

The integrated luminosity is obtained from the number of accepted Bhabha events, N_{Bh}, after subtraction of background events, N_{bkg}, and correction for the experimental efficiency, $\varepsilon_{\mathrm{Bh}}$, and after normalising to the theoretical cross-section, $\sigma^{th}_{\mathrm{Bh}}$:

$$\int L = \frac{N_{\mathrm{Bh}} - N_{bkg}}{\varepsilon_{\mathrm{Bh}}} \cdot \frac{1}{\sigma^{th}_{\mathrm{Bh}}} . \tag{6.3}$$

The present experimental errors are summarised in the first line of Table 6.2 . They are significantly smaller than the error on σ^{th}_{Bh}, and match well the systematic error of the hadronic event selection.

	ALEPH			DELPHI			L3			OPAL		
	'93	'94	'95	'93	'94	'95	'93	'94	'95	'93	'94	'95
$\mathcal{L}^{\rm exp.}$	0.067%	0.073%	0.080%	0.24%	0.09%	0.09%	0.10%	0.078%	0.128%	0.046%	0.046%	0.046%
$\sigma_{\rm had}$	0.068%	0.072%	0.073%	0.10%	0.10%	0.10%	0.052%	0.051%	0.10%	0.084%	0.084%	0.094%
$\sigma_{\rm e}$	0.30%	0.30%	0.31%	0.59%	0.54%	0.75%	0.30%	0.23%	1.0%	0.23%	0.24%	$^{(a)}$
σ_{μ}	0.12%	0.12%	0.12%	0.28%	0.30%	0.40%	0.31%	0.31%	1.0%	0.16%	0.15%	$^{(a)}$
σ_{τ}	0.20%	0.20%	0.20%	0.60%	0.60%	0.60%	0.67%	0.65%	0.60%	0.43%	0.46%	$^{(a)}$
$A_{\rm fb}^{\rm e}$	0.0018	0.0019	0.0020	0.0025	0.0022	0.0021	0.003	0.003	0.01	0.0016	0.0016	0.002
$A_{\rm fb}^{\mu}$	0.0005	0.0005	0.0005	0.0010	0.0015	0.0015	0.0008	0.0008	0.005	0.001	0.001	0.001
$A_{\rm fb}^{\tau}$	0.0009	0.0007	0.0009	0.0020	0.0020	0.0020	0.003	0.003	0.003	0.002	0.002	0.002

Table 6.2: *Preliminary experimental systematic errors for the analysis of the Z line shape and lepton forward-backward asymmetries at the Z peak (from [44]). The errors quoted do not include the common uncertainty due to the LEP energy calibration and the calculation of the theoretical small-angle Bhabha cross-section.*
$^{(a)}$*No result quoted yet.*

6.1.2 Classification of events

The design of the LEP detectors and the cleanliness of the LEP beams allowed the experiments to trigger on multi-hadronic and leptonic Z decays with high redundancy and essentially 100% efficiency. The identification of multi-hadronic events is based on a few simple cuts like track and cluster multiplicities, deposited energy or energy balance along the beam line.

The experiments use very detailed simulation programs [35, 37] to understand their selection efficiencies. Thanks to the high redundancy of their detectors, cross-checks using the data themselves are possible by comparing event samples identified with different selection criteria.

Hadronic events are characterised by a large number of particles, leading to high track multiplicities in the central detectors and high cluster multiplicities in the electromagnetic and hadron calorimeters. For genuine $q\bar{q}$ events, the energy is balanced along the beam line, which is not the case for hadronic events produced in two-photon reactions.

Lepton pairs are selected by requiring low track and cluster multiplicities. Electrons are identified by requiring an energy deposit in the electromagnetic calorimeters close to the centre-of-mass energy. Muons have track momenta close to the beam energy, only minimum ionising energy deposits in the electromagnetic and hadron calorimeters and signals in the outer muon chambers. In $\tau^+\tau^-$ events energy is missing due to the undetectable neutrinos from the decay of the two τ leptons. These are therefore selected by requiring the total energy and momentum sums to be below the centre-of-mass energy to discriminate against e^+e^- and $\mu^+\mu^-$, and to be above a minimum energy to reject lepton pairs arising from two-photon reactions. Backgrounds are typically a few permille for multi-hadrons, $O(0.1\%)$ for e^+e^- and $\mu^+\mu^-$ and $O(1\%)$ for $\tau^+\tau^-$.

The separation between leptonic and hadronic events and their distinction from two-photon reactions ("2γ") are exemplified in Figure 6.2, in a two-dimensional distribution of the number of charged tracks and the energy sum of all tracks calculated from the measured momentum assuming the pion mass. A peak from e^+e^- and $\mu^+\mu^-$ events at high momenta and low multiplicities is clearly separated from two-photon background at relatively low multiplicities and momenta. The intermediate momentum region at low multiplicities is populated by $\tau^+\tau^-$ events. Hadronic events populate the high multiplicity region at energies below the centre-of-mass energy, since neutral particles in the jets are not measured in the central detector.

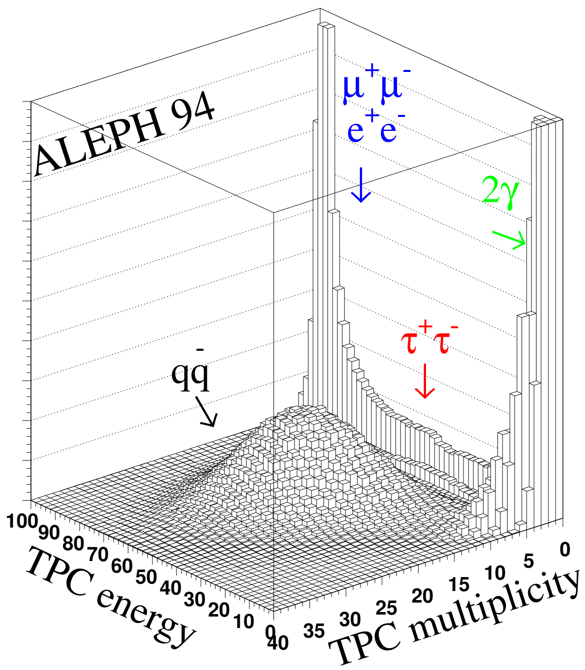

Figure 6.2: *Distribution of the charged track multiplicity ("TPC multiplicity") and the sum of track energies ("TPC energy") measured in the central detector of ALEPH.*

6.1.3 The hadronic cross-section

Since the Z decays predominately to hadrons, this channel provides the highest statistical precision and contributes most to determinations of the Z mass and width. The high statistics must be matched by low systematic errors in the selection procedures and acceptance corrections. The latter can be kept small by using calorimetric measurements, because the coverage in polar angle of the calorimeter systems of all detectors is better than the angular coverage of the tracking systems, and therefore the uncertainty from unmeasured particles escaping through the beam pipe is less important. The measurements are corrected to full acceptance assuming an angular dependence of the symmetric part in $\cos\theta$ of the initially produced quark pair according to $1+\cos^2\theta$; hadronisation effects require the use of QCD event generators. Events with initial state radiation lead to a reduced effective centre-of-mass energy, $\sqrt{s'}$; such events are included in the definition of the cross-sections and also require corrections based on event generators. The minimal values of $\sqrt{s'}$ differ among the experiments and range between its minimum of twice the quark mass up to 10% of the centre-of-mass energy.

Hadronic events can be selected with simple cuts on the track and cluster multiplicities and on the total momentum or energy. This guarantees high selection efficiencies and already suppresses backgrounds from leptonic Z decays to a sufficiently low level. Contributions from two-photon reactions, $e^+e^- \to e^+e^- +$ hadrons, may be further suppressed by cutting on the energy imbalance along the beam line.

Various techniques are employed to control systematic errors at the required low level. The ALEPH collaboration uses two selections, one based on the calorimeter system with an acceptance of $\sim$99.1 % and one purely based on TPC tracks with an acceptance of $\sim$97.5 %. Only relatively simple cuts are needed to identify hadronic events. Both selections demand more than 5 charged tracks coming from the interaction point within a polar angle range of $|\cos\theta| < 0.95$. The TPC selection requires the energy calculated from the momentum sum of all tracks to be greater than 10 % of the centre-of-mass energy. The calorimetric selection demands a combined electromagnetic and hadronic energy sum of more than 20 % of the beam energy, and more than 7 GeV in the barrel region or more than 1.5 GeV in each endcap. The acceptance corrections are based on the QCD event generator JETSET [48] and are controlled by rotating well measured events in the barrel region into the beam pipe region. Effects from undetected particles can thus be simulated in real data and Monte Carlo and the level of agreement serves as an estimate of the systematic error arising from the understanding of the acceptance. The calorimetric and track based selections are averaged, taking into account common parts of the statistical and systematic errors.

The DELPHI selection is based on charged tracks only. The multiplicity of tracks with momentum greater than 0.4 GeV in a polar angle range between 20° and 160° is required to be at least four, and the energy calculated from the sum of all track momenta had to exceed 12 % of the centre-of-mass energy. The efficiency of this selection is $\sim$95.2 % with an estimated systematic error of about 0.1 %.

The L3 measurement is based on the calorimeters and achieves an acceptance of $\sim$99.2 %. Events are selected if the total visible energy exceeds 50 % of the centre-of-mass energy and the hadronic energy is greater than 2.5 GeV; cuts on the energy balance along the beam line and in the transverse direction in combination with requirements on the total number of clusters efficiently suppress background from leptonic Z decays and from two-photon reactions. The uncertainty in the residual acceptance correction is estimated by using the HERWIG generator [49] in addition to JETSET.

The OPAL event selection employs combinations of charged tracks and calorimeter clusters. The visible energy, which also includes the forward detector system, must exceed 9 % of the beam energy, and the sum of the invariant masses calculated from the tracks in each of two hemispheres defined by a plane perpendicular to the thrust axis of each event is demanded to be greater than 3.5 GeV. Cuts on track and cluster multiplicities and on the energy imbalance along the beam line suppress backgrounds. The acceptance of this selection is $\sim$99.6 %; uncertainties in the small acceptance correction due to the beam pipe or other holes in the coverage of the detector are determined by studying the effect of a simulated hole in the barrel region, both in data and in Monte Carlo events.

Dominant backgrounds to the hadron samples selected this way arise from Z decays to $\tau^+\tau^-$ with subsequent hadronic τ decays and from two-photon interactions with hadrons in the final state. Background from $\tau^+\tau^-$ is estimated using a leptonic event generator [50]. The remaining uncertainties are small and only affect the measurement of the pole cross section, because the line shape of this background is the same as that of the hadrons. The two-photon background shows only a small energy dependence over the range of the Z resonance and is typically several tens of pb in magnitude; since this component is non-resonant, its uncertainty also affects the error on the Z width.

The total systematic errors attributed to their hadronic event selections by the collaborations are summarised in the second line of Table 6.2 .

Measurements by the DELPHI collaboration of the hadronic cross-section at different energies are shown in Figure 6.3 . The measurements are compared with the Standard Model expectation for two, three and four generations of light neutrinos.

6.1.4 The leptonic cross-sections

Although the leptonic cross-sections also contribute to the line shape parameters m_Z and Γ_Z, the main interest is the precision measurement of the leptonic Z branching ratio rel-

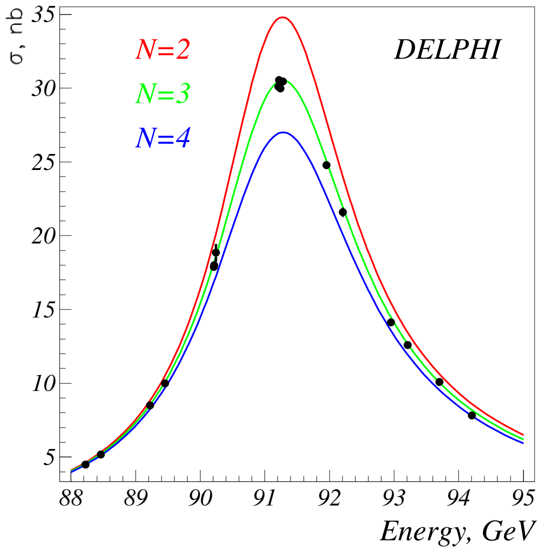

Figure 6.3: *Measurements of hadronic cross-sections by the DELPHI collaboration, from [51]. The errors are smaller than the size of the data points and therefore invisible.*

ative to the hadronic one. Distinguishing between lepton species provides an experimental test of the universality of Z couplings to all charged lepton species, which is assumed to hold in the Standard Model. If this is validated experimentally, then all leptons can be combined to determine the leptonic branching ratio. Systematic errors arising from ambiguities in the identification of different lepton species cancel, if the analysis is designed such that it starts from a common lepton sample and events are classified as e^+e^-, $\mu^+\mu^-$ or $\tau^+\tau^-$ final states within this sample.

The use of tracking information is a necessary ingredient in the lepton analyses, and therefore the angular ranges are restricted to $|\cos\theta|$ less than 0.90 to 0.95 or even lower in $\tau^+\tau^-$ final states. In e^+e^- final state the t-channel contribution is large in the forward direction, and therefore the angular range is commonly restricted to $|\cos\theta| < 0.7$ in this channel; however, ALEPH uses an asymmetric acceptance $-0.9 < \cos\theta < 0.7$. The selection efficiencies within these fiducial acceptances are high, typically around 99 %, and the resulting systematic errors are therefore small, as can be seen from lines three to five in Table 6.2. Backgrounds arise from the ambiguity in the distinction of $\tau^+\tau^-$ events with subsequent τ decays to leptons from e^+e^- and $\mu^+\mu^-$ final states, and from two-photon reactions. Cosmic ray background from muons traversing the detectors is at the permille level, but can safely be subtracted by extrapolating from clear cosmic ray induced events that miss the interaction point or arrive earlier or later in time than the interacting particle bunches in the beams.

The t-channel contribution in the $e^+e^- \to e^+e^-$ channel is either explicitely included in the measurement and taken into account at the level of the fit performed to extract R_e, or it is subtracted from the measured cross-sections before they enter into the fit. Systematic uncertainties from the t-channel have recently been estimated [52] by careful comparison of the calculations implemented in ALIBABA [53] and TOPAZ0 [24]. The estimated systematic errors on the subtracted t-channel contribution lie between 1.2 pb and 1.5 pb over the LEP I energy range, if a large acollinearity between the final state electrons of 25 ° is allowed for.

Leptonic event generators [54, 50] and detailed detector simulations are employed to correct for detector effects within the acceptance. Depending on the cuts that can be handled by the fitting programs used to extract electroweak parameters, a correction to full acceptance may be needed, *i. e.* to $|\cos\theta| \leq 1$ which is achieved with the help of the event generators.

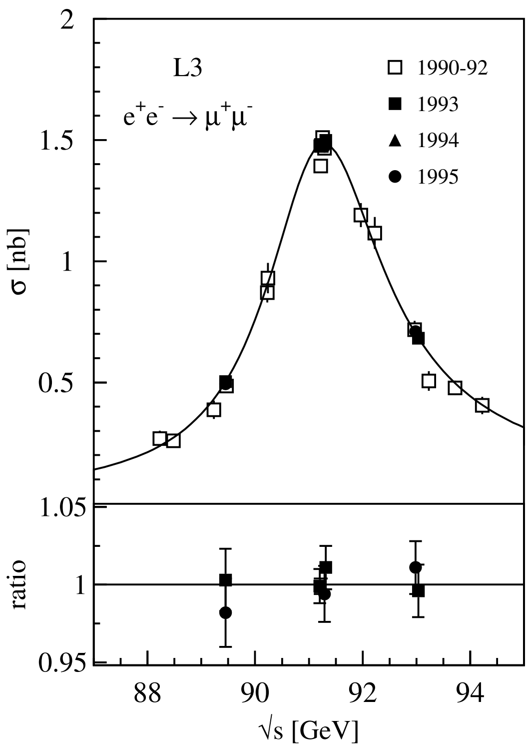

Figure 6.4: *Measurements of muon cross-sections by the L3 collaboration, from [55].*

As an example, measurements of the $e^+e^- \to \mu^+\mu^-$ cross-section by the L3 collaboration are shown in Figure 6.4. The solid line shows the result of the fit to the hadron and muon data based on the parameters m_Z, Γ_Z, σ^0_h and R_μ (see section 6.3 for details). In this fit the shape of the curve is mostly fixed by the measurements of the hadronic cross-sections, whereas the height is given by the muon data. The scatter of the measurements about the fitted line is shown in the lower part of the figure and demonstrates the good agreement of the measurements with the parametrisation.

6.2 Forward-backward asymmetries

Measurements of the leptonic forward-backward asymmetries do not require the same high quality criteria on the detector performance as are needed in the cross-section measurements. Since the asymmetries are determined from the fractions of forward ($\cos\theta > 0$) and backward ($\cos\theta < 0$) going fermions within selected fermion pair events of one lepton species, no measurement of the integrated luminosity nor a detailed understanding of selection efficiencies are needed. However, it is important to unambiguously determine the charge of the leptons. The precise definition of the angular acceptance is also of great importance. The event sample used to determine the leptonic forward-backward asymmetries is usually slightly larger than the one used for the cross-section measurements.

The same leptonic event generators [54, 50] as for the cross-section measurement, with subsequent detector simulation, are used to handle detector effects and, eventually, to correct the measurements to full acceptance.

The cosine of the scattering angle, $\cos\theta$, is defined either in the laboratory frame or, again depending on the fitting program used, in the rest frame of the produced fermion pair, $\cos\theta^*$, with

$$\cos\theta^* = \frac{\cos\frac{1}{2}(\theta_- - \theta_+ + \pi)}{\cos\frac{1}{2}(\theta_- + \theta_+ - \pi)},$$

where θ_- and θ_+ are the scattering angles of the lepton respectively anti-lepton. Both definitions are in principle equivalent, but require slightly different radiator functions in the de-convolution of pure QED effects.

Instead of taking the difference of the forward and backward cross-sections normalised to the total cross-section ("counting method"), *i. e.*

$$A_{\rm fb} = \frac{\sigma(\cos\theta > 0) - \sigma(\cos\theta < 0)}{\sigma^{\rm tot}},$$

the experiments extracted the forward-backward asymmetry from a maximum-likelihood fit to the assumed $\cos\theta$-dependence of the cross-section ("fitting method") according to

$$\frac{d\sigma}{d\cos\theta} = C\cdot(1+\cos^2\theta + \frac{8}{3}A_{\rm fb}\cos\theta)\,; \qquad (6.4)$$

C is simply an arbitrary normalisation constant reflecting the fact that no absolute cross-section normalisation is needed in the $A_{\rm fb}$ measurement. This method provides a slightly better statistical precision because the full shape of the angular distribution is used and not only two angular bins. The method is insensitive to details of the experimental acceptance, as long as this does not discriminate between positively and negatively charged leptons. Differences between the counting and fitting methods provide valuable systematic checks on possible detector defects if found to be beyond the statistical expectation.

t-channel contributions in the $e^+e^- \to e^+e^-$ channel are treated as in the cross-section measurements, either by explicitely including them in the fitting procedure or by correcting the measured asymmetries before they enter into the fit.

Measurements of the differential cross-section of $e^+e^- \to \mu^+\mu^-$ at different energies are shown in Figure 6.5 . They illustrate well the different magnitudes of the cross-sections at different energies and also clearly show the change in angular dependence with energy.

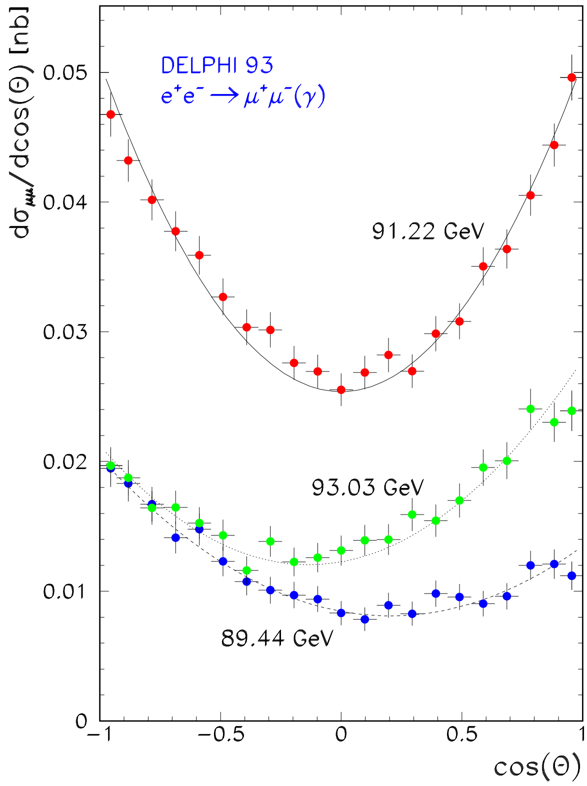

Figure 6.5: *Measurements of the differential muon cross-section at different energies by the DELPHI collaboration, from [51].*

Figure 6.6 shows the measured asymmetries by all experiments as functions of the centre-of-mass energy. They agree well with the Standard Model expectation shown as the full line.

Averages over the four experiments of the ratio of the leptonic and hadronic widths and the pole asymmetries are summarised in Figure 6.7 . Details of the fitting and averaging procedures involved will be given in sections 6.3 and 6.4 . The agreement among the lepton species and with the Standard Model is good, justifying the assumption of universality of the Z couplings to leptons.

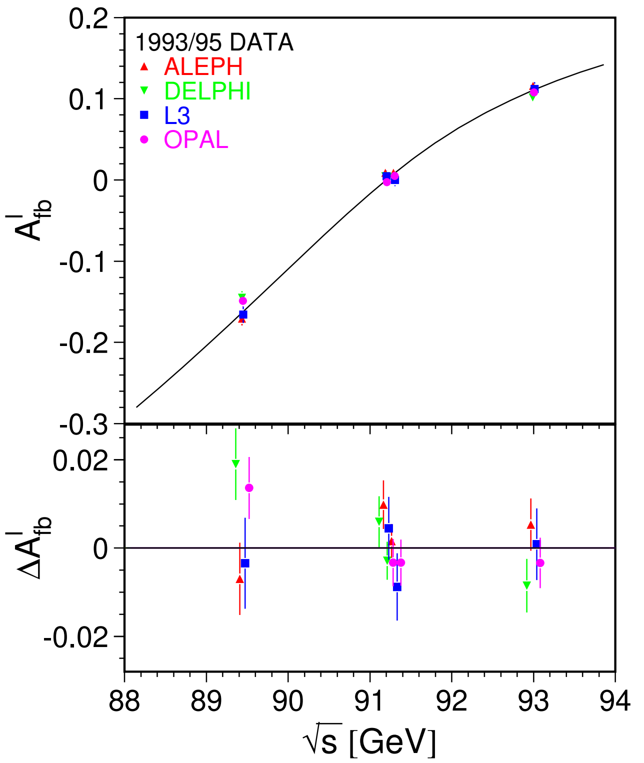

Figure 6.6: *Measurements of leptonic forward-backward asymmetries by the LEP experiments.*

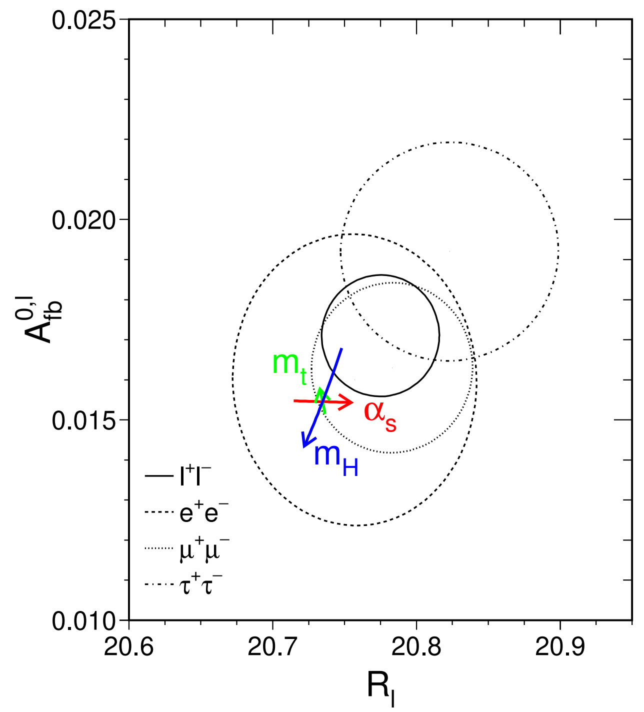

Figure 6.7: *Measurements by the four LEP experiments of the ratios of partial widths, R_ℓ, and the pole forward-backward asymmetry for leptons, $A^{0,\ell}_{\rm fb}$. The contour lines refer to 68 % confidence level. The arrows indicate the Standard Model expectation for* $m_{\rm t} = (176.5 \pm 5.5)$ GeV, 60 GeV $< m_{\rm H} <$ 1000 GeV *and* $\alpha_s = 0.118 \pm 0.003$.

6.3 The fitting procedure

The measured cross-sections and forward-backward asymmetries were treated in χ^2 minimisation procedures to extract essentially model-independent parameters describing the line shape and asymmetry measurements. Although different in detail, the four LEP experiments have agreed to present their results using a common set of nine parameters, namely $m_{\rm Z}$, $\Gamma_{\rm Z}$, $\sigma^0_{\rm h}$, $R_{\rm l}$ and $A^{0,\ell}_{\rm fb}$ for ℓ = e, μ, τ. (see sections 5.2.1 and 5.2.2). The full covariance matrix of the input measurements, $(\mathcal{V}_{exp})$, was constructed by each collaboration, *exp* = A, D, L, O, to describe the correlations between statistical and systematic errors of the measurements. The typical size of the error matrix is 182×182, resulting from 26 different energy points at which cross-sections in four channels and forward-backward asymmetries in three channels were determined. Correlations between the errors arise from the statistical and systematic errors of the luminosity measurements used for all cross-section determinations, from the detector acceptance and efficiencies, from the LEP beam energy common to all channels, and from uncertainties in the theoretical calculations, which are dominated by the uncertainty on the small-angle Bhabha cross section and the t-channel contribution to wide-angle Bhabha scattering.

The uncertainty on the centre-of-mass energy, given by the energy error matrix $(\mathcal{V}^E)$ of Table 3.5, was propagated to an error matrix of the measured cross-sections via

$$(\mathcal{V})_{i,j} = \frac{d\sigma(E_i)}{dE} \cdot (\mathcal{V}^E)_{i,j} \cdot \frac{d\sigma(E_j)}{dE}, \qquad (6.5)$$

and analogous for the asymmetries.

The spread of the centre-of-mass energy due to the natural spread in energy of the beam particles leads to a correction on the cross-sections given by equation 3.9 and the values of the energy spread listed in Table 3.3 . The effects of this correction are an increase of the cross-section at $\sqrt{s} = m_{\rm Z}$ of 0.16%, a decrease of $\Gamma_{\rm Z}$ of about 5 MeV and are negligible on other quantities.

χ^2 is given in terms of the vector of measurements, $\left(\sigma^j, A^j_{\rm fb}\right)$, the vector of theoretical predictions, $(\sigma^t(\mathrm{f\bar{f}}, E_i, \mathbf{p}), A^t_{\rm fb}(\mathrm{f\bar{f}}, E_i, \mathbf{p}))$, depending on the parameter vector $\mathbf{p} = (m_{\rm Z}, \ldots, A^{0,\tau}_{\rm fb})$, and the covariance matrix, $(\mathcal{V}_{exp})$, of the measurements by

$$\begin{aligned} \chi^2 \quad &= \quad \Delta^T \cdot (\mathcal{V}_{exp})^{-1} \cdot \Delta \quad \text{with} \\ &\Delta = (\sigma^t(\ldots), A^t_{\rm fb}(\ldots)) - \left(\sigma^j, A^j_{\rm fb}\right) . \end{aligned} \qquad (6.6)$$

The theoretical predictions for the cross-sections and asymmetries depending on the parameters $\mathbf{p}$, as illustrated by equation 5.1, are calculated for each final state, $\mathrm{f\bar{f}}$, and each energy, E_i, by the use of semi-analytical calculations available as computer codes. DELPHI, L3 and OPAL use ZFITTER [25], the ALEPH collaboration uses MIZA [56]. ZFITTER can handle simple cuts like the minimal scattering angle of the outgoing fermion and the maximal acollinearity angle between the final state fermions, whereas MIZA requires the input measurements to be corrected to full acceptance.

The measured values of the nine parameters of interest, denoted by the vector **p**, are determined by the set of numbers for which χ^2 becomes minimal. The minimisation procedure also determines the correlation coefficients between the parameters.

The four sets of nine parameters, one for each experiment, are shown in Table 6.3; more details and the full correlation matrices may be found in the references [57, 51, 55, 38, 44]. Figures illustrating the agreement of the individual measurements, their averages and the agreement with Standard Model expectations are presented in section 6.4.1 .

The OPAL numbers in Table 6.3 are derived by parameter transformation from a more model independent set of 15 parameters used by this collaboration, which describes the γ–Z interference contribution to the leptonic cross-sections and asymmetries by additional free parameters. The OPAL and L3 measurements of the Z mass and width have been provisionally corrected for small shifts between the preliminary and final determination of the beam energy; fits with the full covariance matrix of the final energy determination (see Table 3.5) were so far released by ALEPH and DELPHI only.

	ALEPH	DELPHI
m_Z [GeV]	91.1883 ± 0.0031	91.1866 ± 0.0029
Γ_Z [GeV]	2.4951 ± 0.0043	2.4893 ± 0.0040
σ_h^0 [nb]	41.520 ± 0.068	41.556 ± 0.079
R_e	20.659 ± 0.088	20.89 ± 0.13
R_μ	20.820 ± 0.061	20.690 ± 0.078
R_τ	20.769 ± 0.071	20.88 ± 0.13
$A_{fb}^{0,e}$	0.0176 ± 0.0037	0.0189 ± 0.0050
$A_{fb}^{0,\mu}$	0.0170 ± 0.0025	0.0154 ± 0.0027
$A_{fb}^{0,\tau}$	0.0167 ± 0.0028	0.0222 ± 0.0039
	L3	OPAL
m_Z [GeV]	91.1886 ± 0.0029	91.1843 ± 0.0029
Γ_Z [GeV]	2.4999 ± 0.0043	2.4958 ± 0.0043
σ_h^0 [nb]	41.411 ± 0.074	41.46 ± 0.07
R_e	20.78 ± 0.11	20.83 ± 0.14
R_μ	20.84 ± 0.10	20.794 ± 0.069
R_τ	20.75 ± 0.14	20.98 ± 0.11
$A_{fb}^{0,e}$	0.0148 ± 0.0063	0.0107 ± 0.0054
$A_{fb}^{0,\mu}$	0.0176 ± 0.0035	0.0156 ± 0.0026
$A_{fb}^{0,\tau}$	0.0233 ± 0.0049	0.0189 ± 0.0034

Table 6.3: *Results from fits to the hadronic and leptonic cross-section and to the leptonic forward-backward asymmetries of individual experiments [58, 44]. All numbers are preliminary.*

6.3.1 Study of common theoretical uncertainties

Indications on the size of the uncertainties arising from the parametrisation of the line shape curves can be addressed by comparing different calculations. Full fits with the computer programs MIZA and ZFITTER have been performed on the same input data, and the differences were found to be small compared to the experimental errors. The hadronic pole cross-section, σ_h^0, comes out 0.01 nb different, and the leptonic pole asymmetries show differences of only 0.0002. Differences in other parameters are much less important. This difference seen in σ_h^0 is slightly smaller than the contribution of the estimated uncertainty of about 0.1 % in the radiative corrections [18]. These findings are consistent with the recent, very detailed comparison of different calculations [17], which also includes a third program, TOPAZ0 [24], but does not perform full fits to cross section and asymmetry data. At the peak, $\sqrt{s} = m_Z$, the deviations between the calculations on the predicted size of the deconvolution of pure QED radiative contributions are 0.01 nb on the hadronic pole cross-section and 0.0002 on the lepton forward-backward asymmetries. Errors at this level are (at present) negligible compared to the uncertainty which is induced by the theoretical error in the luminosity determination or compared with the statistical errors in the leptonic pole asymmetries.

A small dependence of the measured parameters on the Standard Model is introduced through those parts of the parametrisation that are fixed to their expected values, like imaginary parts of the couplings and the γ–Z interference term in the parametrisation of the hadronic cross-section. The dominant effect is due to the Higgs boson mass, m_H, since all other parameters of the Standard Model are reasonably well fixed by now. Some of the results shown in Table 6.3 above prefer a rather low value of the Higgs boson mass below 60 GeV, whereas it is usually set to m_H=300 GeV in the calculations of the fixed contributions. This may result in shifts of parameters extracted from combined fits to electroweak precision data. To quantify this, effects on the derived line shape and asymmetry parameters due to variations of the Higgs boson mass were investigated. Compared with experimental errors, the only noticeable effect is on the Z mass, where a large variation of m_H between 10 GeV and 1000 GeV leads to a small uncertainty of only $\Delta_H m_Z = \pm 0.3$ MeV.

Systematic uncertainties from the treatment of t-channel and s–t interference contributions are correlated between all experiments. They were determined by including in the fit to the ALEPH data the energy-dependent uncertainties of reference [52] at each energy point, and can be considered as representative of other experiments also. t-channel uncertainties were found to contribute ± 0.025 to the error on R_e and ± 0.0002 to the error on $A_{fb}^{0,e}$.

6.4 Combination of line shape and asymmetry results by the four experiments

The combination of the results obtained by the four collaborations is based on the common set of the nine parameters m_Z, Γ_Z, σ_h^0, R_ℓ and $A_{fb}^{0,\ell}$ for ℓ = e, μ, τ and the full error correlation matrices, (C_{exp}), for each of the four experiments, exp = A, D, L, O. In addition, the contributions of errors common among all experiments have to be taken into account. These common errors arise from the uncertainties in centre-of-mass energy and from the use of event generators common to all experiments, which have errors due to uncertainties in the underlying calculations. Most important are the uncertainties on the luminosity determination from small angle Bhabha scattering with an error of 0.11 % on the value of the measured luminosity, and uncertainties from the calculated t-channel contribution in e^+e^- final states of ± 0.025 on R_e.

The individual covariance matrices and the matrix of common errors are used to construct the full covariance matrix, (C), of all input measurements. A symbolic representation of this matrix is shown in Table 6.4. Each table element represents a 9×9 matrix: (C_{exp}) for exp = A, D, L and O are the covariance matrices of the experiments and $(C_c) = (C_E) + (C_L) + (C_t)$ is the matrix of common errors: (C_E) is the error matrix due to LEP energy uncertainties as given in Table 6.5; (C_L) arises from the theoretical error on the small-angle Bhabha cross-section calculations, and C_t contains the common error from the t-channel treatment in the e^+e^- final state.

(C)	ALEPH	DELPHI	L3	OPAL
A	(C_A)	(C_c)	(C_c)	(C_c)
D		(C_D)	(C_c)	(C_c)
L			(C_L)	(C_c)
O				(C_O)

Table 6.4: *Symbolic representation of the covariance matrix, (C), used to combine the line shape and asymmetry results of the four experiments. Elements below the diagonal are the same as those above, but are left blank for simplicity. The components of the matrix are explained in the text.*

The combined parameter set and its covariance matrix are obtained from a χ^2 minimisation, with

$$\chi^2 = (\mathbf{X} - \mathbf{X_m})^T (C)^{-1} (\mathbf{X} - \mathbf{X_m}); \tag{6.7}$$

$(\mathbf{X} - \mathbf{X_m})$ is the vector of residuals of the combined parameter set to the individual results.

The contribution of energy related uncertainties to the error on the nine parameters, which are common to all LEP experiments, were determined in a special fit by reducing the experimental errors to half their original values, whereas the energy related uncertainties remained unchanged. In this way, two covariance matrices are obtained, which are each written as the sum of an experimental component, (C^0_{exp}), and another one, (C_E), from energy uncertainties :

$$\begin{aligned} (C_{exp}) &= (C^0_{exp}) + (C_E) \\ (C_{exp,\frac{1}{2}}) &= (C^0_{exp})/4 + (C_E)\,. \end{aligned}$$

Here, $(C_{exp,\frac{1}{2}})$ is the error matrix of the fitted parameters with halved experimental errors, and (C_{exp}) is the full covariance matrix as defined above. Although it is not strictly possible to write the squared total error as a quadratic sum of two components, a good approximation is obtained this way, which is in agreement with the naive expectations, see *e. g.* equation 3.2. The contribution to the error matrix from energy uncertainties is then determined analytically by

$$(C_E) = \frac{4}{3}(C_{exp,\frac{1}{2}}) - \frac{1}{3}(C_{exp})\,. \tag{6.8}$$

This procedure was used on data of the ALEPH and L3 [59] collaborations, and good agreement on the extracted matrix (C_E) was found. The energy related errors are shown in Table 6.5. Compared with other errors, only the contribution to the errors on m_Z and Γ_Z of 1.5 MeV and 1.2 MeV, respectively, is important. The anti-correlation between the electron asymmetries and the μ and τ asymmetries is due to the negative slope in the energy dependence of the electron asymmetry from the t-channel contribution.

(C_E)	m_Z [MeV^2]	Γ_Z [MeV^2]	σ_h^0 [nb^2]
m_Z [MeV^2]	1.5^2	-0.4^2	-0.08^2
Γ_Z [MeV^2]		1.2^2	-0.08^2
σ_h^0 [nb^2]			0.0095^2
	$A_{fb}^{0,e}$	$A_{fb}^{0,\mu}$	$A_{fb}^{0,\tau}$
$A_{fb}^{0,e}$	0.00027^2	-0.00018^2	-0.00018^2
$A_{fb}^{0,\mu}$		0.00023^2	0.00023^2
$A_{fb}^{0,\tau}$			0.00023^2

Table 6.5: *The contribution of LEP energy uncertainties to the errors on parameters derived from line shape and asymmetry measurements, given as covariance matrix elements. The contribution to the error on Γ_Z for the combined results presented in Table 6.6 is conservatively set to 1.5 MeV, because the L3 and OPAL experiments have not yet updated their results using the full energy error matrix.*

The uncertainties on the energy spread, given in the caption of Table 3.3, lead to an uncertainty of 0.3 MeV on Γ_Z, to a negligible contribution of 0.005 nb to the error on σ_h^0, and are totally negligible for other parameters.

The result of the combination is shown in Table 6.6. The χ^2 per degree of freedom of the combination is 20.8/27; the "χ^2 probability", *i.e* the probability to obtain a value of χ^2 larger than this, is 80 %.

		correlation matrix								
		m_Z	Γ_Z	σ_h^0	R_e	R_μ	R_τ	$A_{fb}^{0,e}$	$A_{fb}^{0,\mu}$	$A_{fb}^{0,\tau}$
m_Z [GeV]	91.1867 $\pm$ 0.0020	1.00	0.05	−0.01	0.00	−0.03	−0.02	0.02	0.05	0.04
Γ_Z [GeV]	2.4948 $\pm$ 0.0025		1.00	−0.16	0.00	−0.01	0.00	0.00	0.00	0.00
σ_h^0 [nb]	41.486 $\pm$ 0.053			1.00	0.06	0.11	0.08	0.00	0.00	0.00
R_e	20.755 $\pm$ 0.059				1.00	0.05	0.03	−0.01	0.01	0.00
R_μ	20.783 $\pm$ 0.037					1.00	0.06	0.00	0.01	0.00
R_τ	20.823 $\pm$ 0.050						1.00	0.00	0.00	0.01
$A_{fb}^{0,e}$	0.0160 $\pm$ 0.0024							1.00	0.00	0.00
$A_{fb}^{0,\mu}$	0.0163 $\pm$ 0.0014								1.00	0.03
$A_{fb}^{0,\tau}$	0.0192 $\pm$ 0.0018									1.00

		correlation matrix				
		m_Z	Γ_Z	σ_h^0	R_ℓ	$A_{fb}^{0,\ell}$
m_Z [GeV]	91.1867 $\pm$ 0.0020	1.00	0.04	−0.01	−0.02	0.06
Γ_Z [GeV]	2.4948 $\pm$ 0.0025		1.00	−0.15	0.00	0.00
σ_h^0 [nb]	41.486 $\pm$ 0.053			1.00	0.14	0.00
R_ℓ	20.776 $\pm$ 0.028				1.00	0.01
$A_{fb}^{0,\ell}$	0.0171 $\pm$ 0.0010					1.00

Table 6.6: *Combined parameters from line shape and forward-backward asymmetry measurements from the 1990 - 1995 data of the four LEP experiments. In the lower part lepton universality is assumed. The results are still preliminary. Note that correlation matrix elements below the diagonal have been left blank for simplicity.*

With the assumption of universal couplings of the Z to leptons the number of parameters can be reduced to five. Γ_ℓ in R_ℓ is defined as the partial decay width of the Z into massless leptons, *i. e.* Γ_τ was corrected in the average by 0.23 % to take into account τ mass effects. The five parameter results are also shown in Table 6.6 .

6.4.1 Comparison of line shape and asymmetry measurements with Standard Model expectations

The latest, close to final results on the Z mass are shown in Figure 6.8 . The value for χ^2 per degree of freedom represents the diagonal χ^2 of the m_Z measurements, taking as the error the experimental error without the common LEP error resulting from energy uncertainties.

The total error on the Z mass arises about equally from statistics ($\pm$1.3 MeV) and from the energy calibration ($\pm$1.5 MeV) and has reached a relative precision of $21 \cdot 10^{-6}$; this is almost as precise as the Fermi constant, with $\Delta G_F/G_F = 20 \cdot 10^{-6}$.

The stability with time of the Z mass measurements at LEP is illustrated in Figure 6.9 . The error on the Z mass was always dominated by the systematic error from the energy calibration. Despite very different calibration techniques and running conditions of LEP the results remained stable over the years. The big improvement between 1991 and 1992 is due to the first measurements of the beam energy with the resonant depolarisation technique; more frequent calibrations in combination with better control and logging of machine parameters led to the steady improvements thereafter.

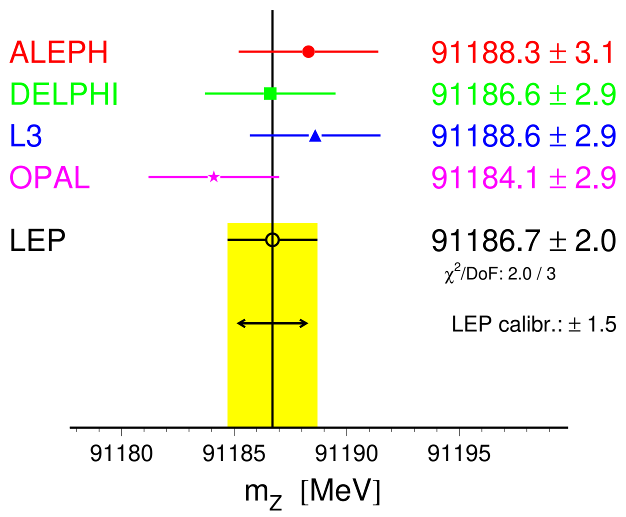

Figure 6.8: *Measurements of the Z mass by the four LEP experiments.*

Due to its high precision, the Z mass is chosen as an input parameter to the Standard Model rather than being a prediction from other precision data; Γ_Z, however, is then predictable. Statistical errors dominate this measurement. This will be even more true once all experiments have updated their measurements with the new energy calibration results, which will bring the current systematic error from

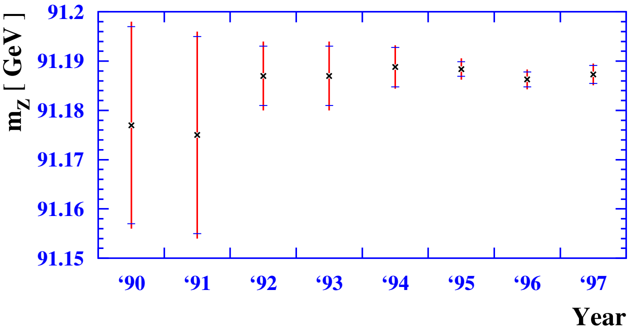

Figure 6.9: *History of the Z mass measurements at LEP. The results are taken from the numbers presented at summer conferences in the year shown on the abscissa. Shown on the measurements are the total errors; the horizontal bars indicate the errors from the energy calibration, which were always dominant.*

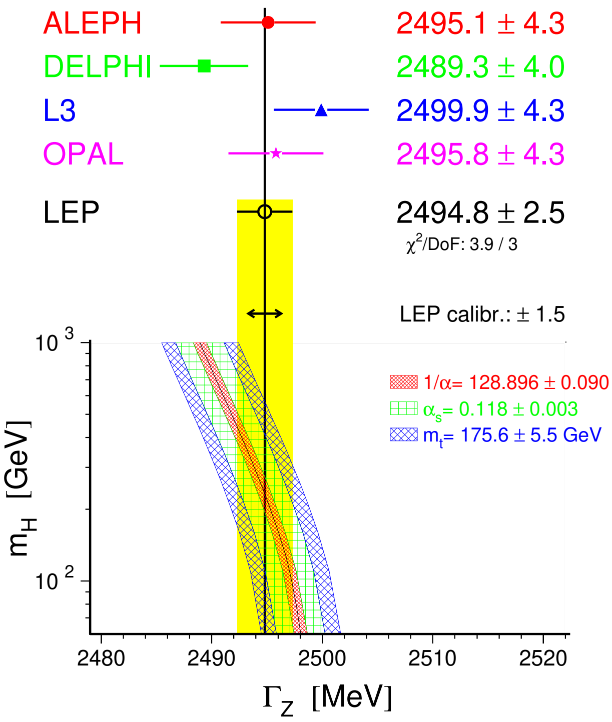

Figure 6.10: *Measurements of the* Z *width,* Γ_Z.

the energy determination of 1.5 MeV down to 1.2 MeV. The level of agreement with the Standard Model expectation, for three generations of light neutrinos, is shown by the graph on the lower part of Figure 6.10, as a function of the value of the Higgs boson mass, m_H. The hatched areas indicate the variation of the electromagnetic coupling constant, $\alpha(m_Z)$, the strong coupling constant, α_s, and the top quark mass, m_t within the ranges indicated in the figure; note that these variations are added linearly. The experimental value of Γ_Z lies at the centre of the Standard Model prediction, which has a large dependence on m_H, α_s and still some dependence on m_t, although this by now has a relative error of only $\Delta m_t / m_t$=3 % .

Results on the hadronic pole cross-sections are shown in Figure 6.11 . The value for χ^2 per degree of freedom represents the diagonal χ^2 of the σ^0_h measurements, taking the experimental errors only without the common error of 0.046 nb from the theoretical uncertainty on the small-angle Bhabha cross-section affecting all luminosity measurements. The agreement among the experiments and with the Standard Model expectation is good. The total error on the LEP average value of σ^0_h is completely dominated by the common error in the luminosity determination. The largest uncertainty on the Standard Model prediction of σ^0_h arises from the uncertainty in the strong coupling constant, α_s. Again, the Standard Model prediction is calculated for three types of light neutrinos.

The measurements of R_ℓ by the individual experiments are summarised in Figure 6.12 . The dependence of the Standard Model expectation on the Higgs mass and on the variation of parameters is also shown on the figure. Clearly visible is the dominant dependence of R_ℓ on the strong coupling constant, α_s. The average of the measurements is consistent with the expectations, slightly preferring a low Higgs mass and a relatively large value of α_s.

Results on the leptonic pole forward-backward asymmetry are given in Figure 6.13 . The average is well consis-

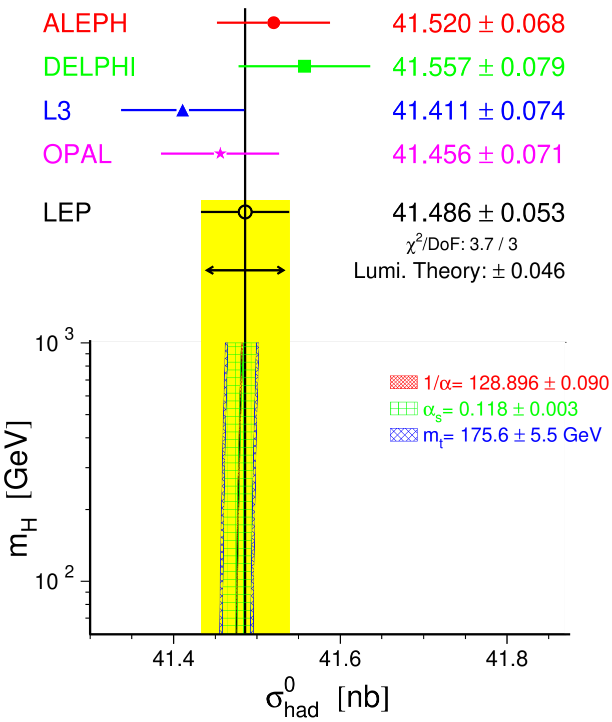

Figure 6.11: *Measurements of the hadronic pole cross-section,* σ^0_h.

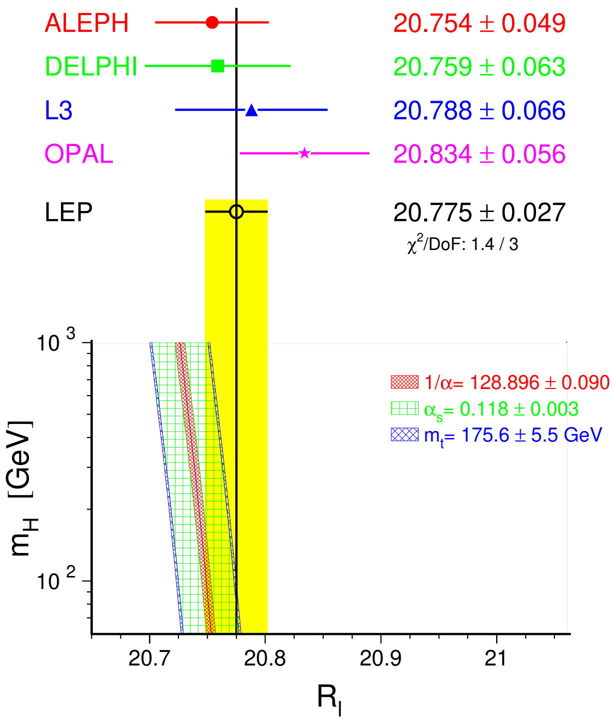

Figure 6.12: *Measurements of the ratio $R_\ell = \Gamma_h/\Gamma_\ell$.*

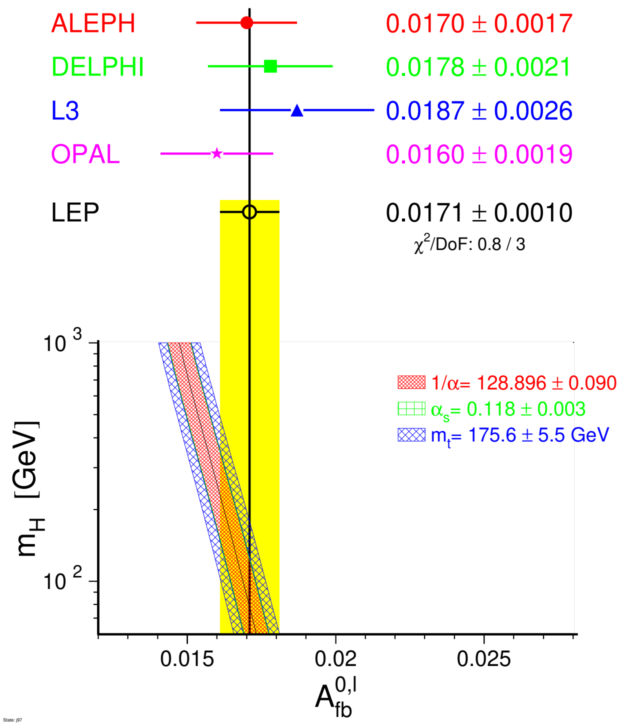

Figure 6.13: *Measurements of the leptonic pole forward-backward asymmetry, $A_{\mathrm{fb}}^{0,\ell}$.*

tent with the Standard Model expectation, preferring a very low value of the Higgs boson mass. There is also a non-negligible dependence of the Standard Model prediction on the value of the electromagnetic coupling constant at the scale of m_Z, $\alpha(m_Z)$ (see section 9.1); the induced error is as large as the one arising from the uncertainty in the mass of the top quark. There is no visible dependence of $A_{\mathrm{fb}}^{0,\ell}$ on the strong coupling constant.

6.4.2 Model-independent Z parameters

All collaborations have also performed fits to their line shape and asymmetry measurements using the S-matrix ansatz [60, 61, 62, 63, 64], as described in section 5.3 . They were combined in the same way as described above for the standard parameter set. The average S-matrix parameters are listed in Table 6.7 .

	LEP average			SM prediction
m_Z [GeV]	91.1882	±	0.0031	–
Γ_Z [GeV]	2.4945	±	0.0024	2.4932
$r_{\mathrm{had}}^{\mathrm{tot}}$	2.9637	±	0.0062	2.9603
r_ℓ^{tot}	0.14245	±	0.00032	0.14253
$j_{\mathrm{had}}^{\mathrm{tot}}$	0.14	±	0.14	0.22
j_ℓ^{tot}	0.004	±	0.012	0.004
r_ℓ^{fb}	0.00292	±	0.00019	0.00266
j_ℓ^{fb}	0.780	±	0.013	0.799

Table 6.7: *Combined results from S-matrix fits of the four experiments, assuming lepton universality. In addition to the data taken around the Z peak data from the high energy running of LEP at 133* GeV*, 161* GeV *and 172* GeV *taken during the years 1995 to 1996 are included. The Standard Model predictions are shown in the last column (for m_t =175.6* GeV*, m_H=300 GeV , $\alpha_s(m_Z)$=0.118 and $1/\alpha(m_Z)$=128.896). Note that the mass and width were corrected for the shifts arising from the different definitions of the Breit-Wigner denominator, $m_Z = \overline{m_Z} + 34.1$ MeV and $\Gamma_Z = \overline{\Gamma_Z} + 0.9$ MeV.*

There is good agreement with the Standard Model expectation. The largest differences are seen in the lepton sector. r_ℓ^{fb} is about 1.4 standard deviations higher than expected and reflects the fact that the forward-backward asymmetries at the peak are measured slightly higher than predicted by the Standard Model. j_ℓ^{fb}, which describes the energy dependence of the forward-backward asymmetries, is $\sim$1.5 standard deviations lower than expected. The other j and r parameters agree much better, and therefore this justifies well the standard procedure to determine the Z parameters, which assumes combinations of couplings as in the Standard Model in all terms describing the differential cross-sections.

The model-independent value of the Z mass agrees well within errors with the standard one of Table 6.6 . The Z mass is strongly correlated with the contribution from the interfer-

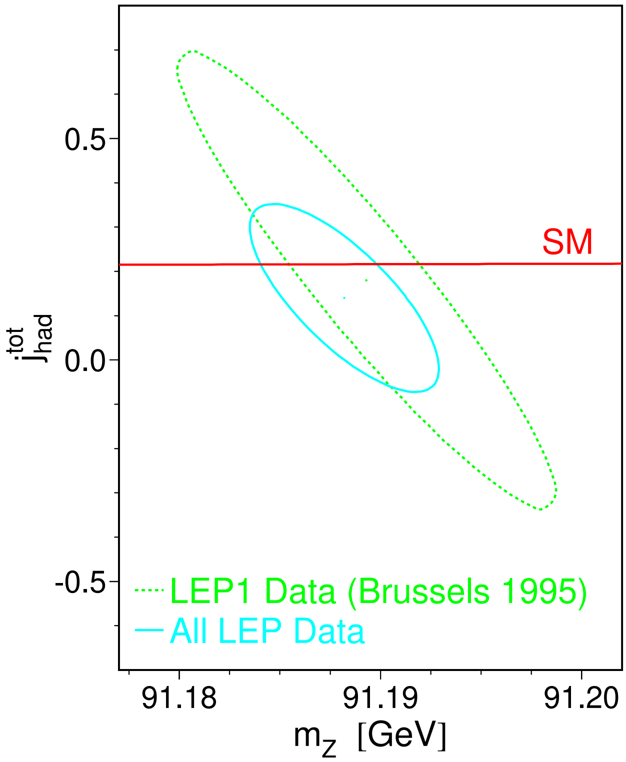

Figure 6.14: *Model-independent determination of the Z mass using the S-matrix ansatz. Shown are the 68 % confidence level contours in the m_Z–j^{tot}_{had} plane for data taken at LEP I alone [65] and including LEP II data taken up to 1996 [44].*

ence term measured by j^{tot}_{had}, which is fixed sufficiently well by the high-energy data to obtain a competitive error on the Z mass. This is shown in Figure 6.14 .

6.5 Inclusive hadronic charge asymmetry

Measurements of the inclusive hadronic charge asymmetry, $\left\langle Q^{q,0}_{fb}\right\rangle$, as explained in section 5.4, have been made by all experiments [66, 67, 68, 69]. The dominant source of systematics arises from the modelling of the charge flow in the fragmentation process. The relevant properties can be measured from the data for heavy quarks, but for light quarks they depend on the fragmentation parameters in the event generators used in the Monte Carlo simulations. At present, the smallest of the fragmentation and decay modelling errors in any pair of individual results is taken as common to both and taken into account in the averaging procedure. The experiments express their results in terms of the leptonic effective weak mixing $\sin^2\theta_W^{eff,\ell}$. The average is $\sin^2\theta_W^{eff,\ell} = 0.2322 \pm 0.0010$, where the error is dominated by systematics.

6.6 Derived parameters from line shape results

By simple parameter transformation of the five and nine parameter results presented in the previous sections one can determine the hadronic or leptonic decay widths of the Z and also the "invisible width", $\Gamma_{inv} = \Gamma_Z - \Gamma_h - \Gamma_e - \Gamma_\mu - \Gamma_\tau$ (see equations 5.3 and 5.5).

	without	with
	lepton universality	
Γ_h [MeV]	1742.3±3.2	1743.2±2.3
Γ_{inv} [MeV]	500.9±2.6	500.1±1.8
Γ_{inv}/Γ_ℓ	-	5.961±0.023
Γ_ℓ [MeV]	-	83.91±0.10
Γ_e [MeV]	83.95 ±0.15	-
Γ_μ [MeV]	83.83 ±0.21	-
Γ_τ [MeV]	83.67 ±0.25	-

Table 6.8: *Partial decay width of the Z, derived by parameter transformation from the results in Table 6.6 and their correlations.*

Table 6.8 gives the results. The agreement within errors of the leptonic widths shows the validity of the assumption that the Z couplings are the same for all lepton species ("lepton universality"). Lepton universality is assumed in the third column of the table and leads to smaller errors also on the hadronic and invisible widths, because Γ_e in equation 5.3 is replaced by the more precise average Γ_ℓ of the three widths. Note that Γ_ℓ is defined as the decay width of the Z to a massless pair of leptons.

Assuming that only neutrinos contribute to the invisible width and using the Standard Model prediction for $(\Gamma_\nu/\Gamma_\ell)_{SM}$=1.991±0.001, the measured value of Γ_{inv}/Γ_ℓ implies for the effective number of light neutrino types

$$N_\nu = \frac{\Gamma_{inv}}{\Gamma_\ell} / \left(\frac{\Gamma_\nu}{\Gamma_\ell}\right)_{SM} = 2.994 \pm 0.011 \,.$$

The value of $(\Gamma_\nu/\Gamma_\ell)_{SM}$ is calculated for a Higgs mass of 300 GeV and a top quark mass of 175.6±5.5 GeV; the error also accounts for a variation of the Higgs mass between 60 GeV $< m_H <$ 1000 GeV. The small uncertainty is due to an almost complete cancellation of higher-order contributions in the ratio of widths. The result obtained for N_ν agrees perfectly within errors with three and justifies the choice for the number of neutrino types made repeatedly above. A value of N_ν clearly excluding two or four could already be determined from the very first results obtained at SLC and LEP. Nowadays, the value of this measurement lies in its usefulness to constrain any non-Standard Model process involving undetectable Z decay products. The good agreement of N_ν with three means that there is no indication for Z decays into invisible particles other than the three neutrino species ν_e, ν_μ and ν_τ. With the Standard Model value of $\Gamma_{\nu}^{SM} = (167.12 \pm 0.2)$ MeV the limit on any non-Standard Model contribution from a process x can be quantified:

$$\begin{aligned} \Gamma_{\text{inv}}^{\text{x}} &= \Gamma_{\text{inv}} - 3\,\Gamma_{\nu}^{SM} \\ &= (-1.3 \pm 1.8)\ \text{MeV} \\ &< 2.8\ \text{MeV at } 95\,\%\ \text{confidence level}\ , \end{aligned}$$

where, conservatively, Γ_{inv}^{x} was constrained to only positive values when deriving the limit, *i.e.* its Gaussian probability density was integrated over positive values only and the limit was set at the point where the integral reaches 95% of the integral from zero to infinity.

It is interesting to note that the error on $\Gamma_{\text{inv}}/\Gamma_{\ell}$ has a large contribution from the relative uncertainty on the luminosity, L, which enters into the widths via their relation with the hadronic pole cross-section (equation 5.3); the error is approximately given by

$$\Delta\frac{\Gamma_{\text{inv}}}{\Gamma_{\ell}} \simeq 15 \cdot \frac{\Delta L}{L}\ .$$

The contribution from the theoretical uncertainty in the luminosity determination alone therefore leads to an error on $\Gamma_{\text{inv}}/\Gamma_{\ell}$ of $\Delta(\Gamma_{\text{inv}}/\Gamma_{\ell})_{lum} = \pm 0.017$, which is the dominant error.

7 Measurements of lepton couplings

In order to extract more information on leptonic couplings other measurements have to be considered, which depend only linearly on the coupling terms, $\mathcal{A}_\ell$, of either the initial or final state particles. These are measurements of τ lepton polarisation and measurements with polarised electrons at the SLC.

7.1 Measurements of τ lepton polarisation

The longitudinal polarisation, $\mathcal{P}_\tau$, of τ leptons from Z decays can be measured from the angular distribution of the decay products from the parity-violating decays of the τ leptons.

In the τ rest frame, the angular distribution of the hadron in semi-hadronic two-body decays of the τ is given by

$$\frac{1}{N}\frac{dN}{d\cos\theta^*} = \frac{1}{2}(1+\xi_s\mathcal{P}_\tau\cos\theta^*)\ ,$$

where ξ_s is one for spinless hadrons (π, K) and $\xi_s = (m_\tau^2 - 2{m_h}^2)/(m_\tau^2 + 2{m_h}^2)$ for hadrons with spin one (ρ, a1).

The angle θ^* in the τ rest frame can be derived from the energy, E_h, of the hadron in the lab frame, where the τ has an energy equal to the beam energy, E_{beam}:

$$\cos\theta^* = \frac{2E_h/E_{\mathrm{beam}} - 1 - (m_h/m_\tau)^2}{1-(m_h/m_\tau)^2}\ .$$

The momentum spectrum of the hadron can therefore be used to measure the average polarisation of the τ leptons. With $x = E_h/E_{\mathrm{beam}}$, this becomes (neglecting mass terms):

$$\frac{1}{N}\frac{dN}{dx} = 1+\xi_s\mathcal{P}_\tau(2x-1)\ .$$

For τ decays into $e\nu\bar{\nu}$ and $\mu\nu\bar{\nu}$ the relation for the energy spectrum is more complicated:

$$\frac{1}{N}\frac{dN}{dx} = \frac{1}{3}\left[(4x^3-9x^2+5)+\mathcal{P}_\tau(8x^3-9x^2+1)\right]\ .$$

Sensitivity to $\mathcal{P}_\tau$ in τ decays into spin-one hadrons can be regained by also measuring the helicity states of the hadrons from their decay products; in addition to θ^*, therefore an additional angle in the hadron rest frame between the hadron's line of flight and the direction or decay plane defined by its decay products is taken into account in the analyses.

The LEP collaborations have used the decay channels $\tau\to e\nu\nu$, $\tau\to\mu\nu\nu$, $\tau\to\pi\nu$, $\tau\to K\nu$, $\tau\to\rho\nu$ and $\tau\to a1\,\nu$. Each channel has to be isolated and analysed separately. The highest sensitivity to $\mathcal{P}_\tau$ is obtained from two-body decays. Experimentally, $\mathcal{P}_\tau$ is estimated from comparisons of the shape of the energy spectrum with Monte Carlo samples generated with $\mathcal{P}_\tau = +1$ or $\mathcal{P}_\tau = -1$. Separate analyses of events with forward and backward going τ leptons allow to determine the forward-backward polarisation asymmetry, $A_{\mathrm{fb}}^{\mathcal{P}_\tau}$. More detailed descriptions of the experimental techniques can be found in the references [70, 71, 72, 73, 44].

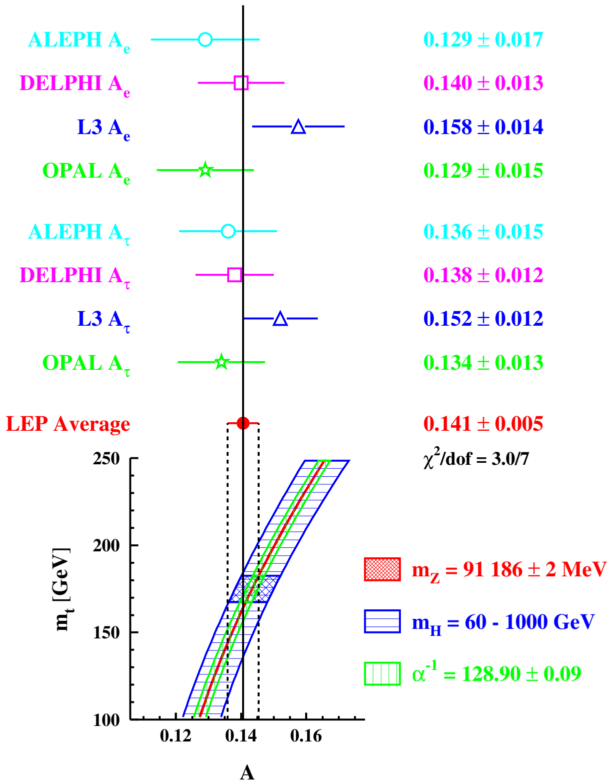

Figure 7.1: *Measurements of the parameters $\mathcal{A}_e$ and $\mathcal{A}_\tau$ from the polar angle dependence of the average tau polarisation, $\mathcal{P}_\tau$.*

Corrections and hence uncertainties on them are small; the $\sqrt{s}$ dependence, radiative effects and mass terms result in a correction of only 0.003 with an estimated error of less than ± 0.001, which is small compared with the experimental errors. The validity of the V$-$A structure in weak decays of τ leptons was assumed without any error. Common uncertainties may arise from the modelling of hadronic τ decays, in particular in the a1 channel. These are also estimated to be at the level of ± 0.001. Tau polarisation measurements at LEP are therefore far from being dominated by common systematic errors, and no such errors need to be taken into account in the averages.

Figure 7.1 and Table 7.1 list the latest results from the LEP experiments. There is good agreement among the measurements and with the Standard Model expectation.

$\mathcal{A}_\tau = -\mathcal{P}_\tau$	0.1411± 0.0064
$\mathcal{A}_e = -\frac{4}{3}A_{fb}^{\mathcal{P}_\tau}$	0.1399± 0.0073
with lepton universality	
$\mathcal{A}_\ell$	0.1406±0.0048

Table 7.1: *Averages of $\mathcal{A}$ parameters from τ polarisation measurements by the LEP experiments.*

7.2 Measurements with polarised electrons at the SLC

The availability of polarised electrons at the SLC and the possibility to measure the left-right polarisation asymmetry of the same kind of observables discussed in the previous sections enables the determination of initial and final state couplings separately according to equations 5.18 and 5.20 in section 5.7 .

The left-right polarisation asymmetry of the hadronic cross-section is determined by simply counting hadronic events in collisions of polarised electrons and unpolarised positrons for the two possible longitudinal polarisation states of the electrons [74]. The measurement does not depend on the knowledge of the absolute luminosity, detector acceptance or efficiency, but requires a precise knowledge of the absolute polarisation averaged over the particles colliding at the interaction point. Small residual corrections from pure γ exchange and γ–Z interference are then applied to the measured asymmetry to obtain directly the combination of couplings denoted by $\mathcal{A}_e$ in section 5.7 .

At present, about 10^5 Z decays have been analysed; this statistics was more than doubled in the recent 1997 run of the SLC. The measurement of the left-right polarisation asymmetry of the hadronic cross section constitutes the most precise single determination of the effective leptonic weak mixing angle.

The longitudinal polarisation of the electron beam, $\mathcal{P}_e$, is constantly determined by use of a Compton scattering polarimeter, which measures the circularly polarised photons from a pulsed high-power laser after they are scattered off the beam particles. The scattered electrons are also monitored in a Cherenkov detector system. Typical beam polarisation levels are around 80 % with a systematic uncertainty estimated to be $\Delta\mathcal{P}_e/\mathcal{P}_e = 0.64\%$. This leads to the dominant systematic error on A_{lr}.

By measuring the left-right forward-backward asymmetries of leptons final state couplings $\mathcal{A}_e$, $\mathcal{A}_\mu$ and $\mathcal{A}_\tau$ become accessible. Assuming lepton universality, these measurements can be combined with the A_{lr} measurement given above.

The present average of all such measurements at the SLC is

$$\mathcal{A}_e = 0.1546 \pm 0.0032 \quad \text{or}$$
$$\sin^2\theta_W^{eff} = 0.23055 \pm 0.00041\,.$$

7.3 Lepton couplings

If the τ polarisation measurements are used together with the leptonic cross-section and forward-backward asymmetry measurements the axial-vector and vector couplings of the Z to leptons can unambiguously be determined using the relations of equations 5.4, 5.5, 5.6, 5.15 and 5.16. The overall sign was chosen to be in agreement with neutrino scattering data [75]. Contour lines of this combination are shown in Figure 7.2 and compared with the Standard Model expectation.

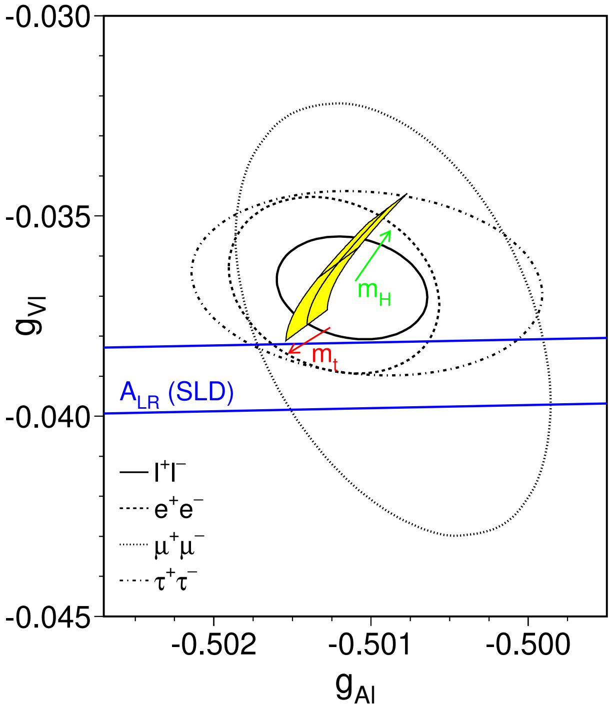

Figure 7.2: *68 % confidence level contour lines in the plane of the effective couplings $\hat{g}_a$ and $\hat{g}_v$ for individual leptons and with lepton universality imposed.*

The couplings of the three lepton species are consistent with one another within the experimental errors, as expected from lepton universality in the Standard Model. The measurement of the left-right polarisation asymmetry by the SLD collaboration, A_{lr}, is also shown in the figure, and reasonable agreement with the LEP measurements is found. The measurements are in agreement with the Standard Model, indicated by the dark area for $m_t = (175.6 \pm 5.5)$ GeV and 60 GeV $< m_H <$ 1000 GeV. The SLD measurement prefers a very small value of the Higgs boson mass.

The values of couplings are listed in Table 7.2 . If the value of the invisible width of the Z (see Table 6.8) is attributed exclusively to the decay into three generations of neutrinos, the coupling to neutrinos can be inferred assuming $\hat{g}^\nu = \hat{g}_a^\nu = \hat{g}^\nu$.

A quantified test of lepton universality is obtained by taking the ratios of coupling constants, as shown in Table 7.3 .

LEP only		
$\hat{g}_v^{\mathrm{e}}$	=	-0.0368 ± 0.0015
$\hat{g}_v^{\mu}$	=	-0.0372 ± 0.0036
$\hat{g}_v^{\tau}$	=	-0.0367 ± 0.0015
$\hat{g}_a^{\mathrm{e}}$	=	-0.50121 ± 0.00046
$\hat{g}_a^{\mu}$	=	-0.50084 ± 0.00067
$\hat{g}_a^{\tau}$	=	-0.50098 ± 0.00075
$\hat{g}_v^{\ell}$	=	-0.03683 ± 0.00085
$\hat{g}_a^{\ell}$	=	-0.50109 ± 0.00032
$\hat{g}^{\nu}$	=	0.50125 ± 0.00092

LEP + SLC		
$\hat{g}_v^{\mathrm{e}}$	=	-0.03845 ± 0.00071
$\hat{g}_v^{\mu}$	=	-0.0357 ± 0.0031
$\hat{g}_v^{\tau}$	=	-0.0365 ± 0.0015
$\hat{g}_a^{\mathrm{e}}$	=	-0.50109 ± 0.00045
$\hat{g}_a^{\mu}$	=	-0.50095 ± 0.00065
$\hat{g}_a^{\tau}$	=	-0.50099 ± 0.00075
$\hat{g}_v^{\ell}$	=	-0.03792±0.00058
$\hat{g}_a^{\ell}$	=	-0.50100±0.00031

Table 7.2: *Effective* Z *couplings to leptons.*

LEP only		
$\hat{g}_v^{\mu}$ / $\hat{g}_v^{\mathrm{e}}$	=	1.01 ± 0.12
$\hat{g}_v^{\tau}$ / $\hat{g}_v^{\mathrm{e}}$	=	0.997 ± 0.060
$\hat{g}_a^{\mu}$ / $\hat{g}_a^{\mathrm{e}}$	=	0.9993 ± 0.0017
$\hat{g}_a^{\tau}$ / $\hat{g}_a^{\mathrm{e}}$	=	0.9996 ± 0.0018

LEP + SLC		
$\hat{g}_v^{\mu}$ / $\hat{g}_v^{\mathrm{e}}$	=	0.928 ± 0.087
$\hat{g}_v^{\tau}$ / $\hat{g}_v^{\mathrm{e}}$	=	0.950 ± 0.044
$\hat{g}_a^{\mu}$ / $\hat{g}_a^{\mathrm{e}}$	=	0.9997 ± 0.0016
$\hat{g}_a^{\tau}$ / $\hat{g}_a^{\mathrm{e}}$	=	0.9998 ± 0.0018

Table 7.3: *Ratios of effective* Z *couplings to leptons as a test of lepton universality.*

The axial-vector couplings of all lepton species are found to be the same with a precision of approximately 0.2 %, and the agreement among the vector couplings is tested to a level better than 10 %.

8 Measurements involving heavy quarks

Measurements of partial decay widths and forward-backward asymmetries for specific quark flavours in $Z \to q\overline{q}$ can only be performed with high precision for b and c quarks, which are separable from the light quarks by means of various tagging techniques. Good control of the tagging efficiencies and purities allows measurements of the production fraction of heavy quarks in Z decays, and the determination of the charge of the produced heavy quarks is essential to measure the forward-backward asymmetries. An overview of the various types of analyses is given in the following subsections. More details on heavy flavour analyses at LEP may be found in a recent review [76].

8.1 Heavy quark tagging methods

8.1.1 Lepton tags

All four experiments employed leptons from semi-leptonic decays of b and c quarks, $b \to \ell^-$ and $c \to \ell^+$, as tags [77, 78, 79, 80]. The large masses and the hard fragmentation function of hadrons containing heavy quarks lead to high-momentum leptons in events where the heavy quark decays semi-leptonically.

Leptons in hadronic events come from the following sources * :

$b \to \ell^- \overline{\nu} X$	prompt b decay
$\bar{c} \to \ell^- \overline{\nu} X$	prompt $\bar{c}$ decay
$\bar{b} \to \bar{c} \to \ell^- \overline{\nu} X$	cascade
$b \to \bar{c} \to \ell^- \overline{\nu} X$	cascade
$q\overline{q} \to \ell^- X$	non-prompt background and misidentified leptons
$\bar{b} \to b \to \ell^-$	$b\bar{b}$ mixing

Electrons in jets are identified by their specific energy loss, dE/dx, in the tracking chambers, by the matching in position and energy of the charged track with the associated energy clusters observed in the electromagnetic calorimeters and by the longitudinal and transverse shape of the energy deposits.

Muons leave minimum-ionising energy deposits in the electromagnetic and the hadron calorimeters and have signals in the outer muon chambers.

The possibility to use several independent experimental signatures to identify leptons allows detailed checks to be made on the Monte Carlo simulations of these processes. Therefore, experimental systematic errors are well under control.

Cuts in the lepton momentum (typically $p \gtrsim 3$ GeV) and in the transverse momentum of the lepton relative to the nearest jet (typically $p_T \gtrsim 1$ GeV) are used to enhance the contribution from $b \to \ell^-$. The branching fractions $BR(b \to \ell)$ and $BR(b \to c \to \ell)$ are determined from the LEP data with sufficient precision, whereas other branching fractions have to be taken from measurements at lower energies at the PETRA, PEP and CESR e^+e^- colliders or from hadronisation models.

The shape of the momentum spectrum of leptons from heavy quark decays is taken from semi-leptonic decay models with parameters tuned to measurements at lower energies. The LEP experiments have agreed on three standard parametrisations, which eases the task of averaging the measurements [81].

The b quark tagging efficiency of lepton tag methods is typically 10 %, and the purity is 90 %.

*This also implies charge conjugate processes.

8.1.2 Vertex tags

The silicon strip vertex detectors enable the LEP experiments to be sensitive to secondary vertices from the decays of b or c flavoured hadrons, which have a decay length of a few millimetres at LEP energies. Despite its larger mass the b quark life time is longer than that of the c quark, because the weak b decay is suppressed by the relevant Kobajashi-Maskawa matrix element. The mean fractions of the beam energy carried by hadrons containing b and c quarks are approximately 70 % and 50 %, again favouring longer paths of flight for b hadrons; on the other hand, c hadrons are lighter than b hadrons. In summary, the life time found in events containing b quarks is larger than in c events, whereas events with u and d primary quarks do not generally contain secondary vertices. Events with a primary s quark contain low-multiplicity vertices at very long life times.

Life time tags either reconstruct explicitly the secondary vertex and determine the decay length, or employ more inclusive methods that are based on the presence of tracks with large impact parameters with respect to the primary event vertex, *i. e.* the interaction point. Vertex tags achieve tagging efficiencies for b quarks of the order of 30 % at 90 % purity.

8.1.3 Combined vertex - mass tag

Another powerful b tag is obtained if vertex information is combined with a tag exploiting the mass difference between b and c quarks. Tracks in a hemisphere are ordered by decreasing consistency with the secondary vertex and their invariant mass is computed, adding one track after the other. The algorithm stops as soon as the c quark mass is exceeded, and the probability that the last added track comes from the primary vertex is used as the tagging variable. In genuine b hemispheres, the c quark mass is easily exceeded using tracks from the secondary vertex only, whereas tracks from the primary vertex have to be added in if the primary quark is lighter.

8.1.4 Event shape tags

Event shape variables which are sensitive to the large mass and hard fragmentation of b quarks allow to select b-enriched event samples. These properties lead to large transverse momenta relative to the direction of the b quark and to a relatively hard momentum spectrum of the decay products from b-hadrons. Sensitive variables are constructed from the transverse and longitudinal momenta of all or the most energetic tracks, from the invariant mass of the tracks, and from classical event shape variables such as the sphericity of a jet. Since the sensitivity of single event shape variables to b quarks is low, the combination of many variables as input to artificial neural networks has become quite common. Compared with other methods, the achievable purities from such tagging methods are low at LEP energies. Therefore event shape tags are usually combined with other methods; solely an event shape tag to determine the b quark branching fraction of the Z boson was used in an analysis by the L3 collaboration [82].

8.1.5 D and D* meson tags

In addition to semi-leptonic decays of heavy quarks, b decays and c fragmentation into D mesons and their subsequent decays into kaons and pions provide a powerful tool to tag the flavour of an event. In the region of high momentum, or high $x = E_{\mathrm{D}}/E_{\mathrm{beam}}$, D mesons arise predominantly from c quarks and are therefore most useful for measurements of R_{c} [83, 84, 85] or the c quark forward-backward asymmetry [86, 87]. The exclusive reconstruction of the D meson decay provides good purities, but the efficiencies suffer from the small fraction of identifiable decay chains. Good particle identification capabilities, in particular the separation of kaons from pions, are essential in these analyses. Good track resolution and double track separation are also needed in the reconstruction of invariant masses of parent particles. Most commonly used are D^* mesons, which decay to a $\mathrm{D}^{0,\pm}$ meson ground state and a photon or pion. The masses of the D^* and the D^0 are very similar, and therefore the difference between the reconstructed mass of a D meson candidate and the invariant mass of the D candidate combined with a charged pion provides a powerful variable to suppress combinatorial background.

A pure sample of events with b and c quarks is obtained that way, and the separation of these two flavours relies on the other methods described above. The component from b quarks in the sample can then be subtracted on a statistical basis.

Samples enriched in c quark content clearly suffer from the small statistics of exclusively reconstructed events, and therefore electroweak measurements with c quarks do not significantly constrain Standard Model parameters; however, their agreement with the Standard Model expectation is an important test of the structure of the vector and axial-vector couplings in the quark sector.

8.1.6 Multi-tag methods

Precision measurements of electroweak parameters from heavy quarks need good control of the purities and efficiencies, which should be largely independent of Monte Carlo simulations. Since b quarks at LEP are produced in pairs, and given the large number of tagging methods available, multi-tag methods have been developed to achieve this goal [88, 89, 90, 91].

Comparing the number of cases where one or both event hemispheres have been tagged as a b quark enables measurements of the tagging efficiency from the data. The fraction of tagged hemispheres, f_t, and the fraction of doubly tagged events, f_{dt}, are given by

$$\begin{aligned} f_t &= R_{\mathrm{b}}\varepsilon_{\mathrm{b}} + R_{\mathrm{c}}\varepsilon_{\mathrm{c}} + (1 - R_{\mathrm{b}} - R_{\mathrm{c}})\varepsilon_{\mathrm{uds}} \\ f_{dt} &= R_{\mathrm{b}}{\varepsilon_{\mathrm{b}}}^2 c_{\mathrm{b}} + R_{\mathrm{c}}\varepsilon_{\mathrm{c}}^2 c_{\mathrm{c}} + (1 - R_{\mathrm{b}} - R_{\mathrm{c}}){\varepsilon_{\mathrm{uds}}}^2 \;, \end{aligned} \tag{8.1}$$

where $R_{\mathrm{b,c}} = \Gamma_{\mathrm{b,c}}/\Gamma_{\mathrm{h}}$, $\varepsilon_{\mathrm{b,c,uds}}$ are the tagging efficiencies for flavours b, c and uds, and c_{b}, c_{c} are factors taking into account correlations between the tagging efficiencies in the two hemispheres of an event. Since ε_{b} is larger than ε_{c} and much larger than $\varepsilon_{\mathrm{uds}}$ and $c_{\mathrm{b}}, c_{\mathrm{c}} \simeq 1$, R_{b} and ε_{b} can be extracted from such measurements. Other parameters have to be taken from Monte Carlo simulations.

Since the event vertex is common to both hemispheres of an event, hemisphere correlations are induced, all summed up in the parameters c_{b} and c_{c} above. If the precision on the primary event vertex is low, the tagging efficiency for both hemispheres will be reduced; if a b with a long lifetime is present in one hemisphere, it will certainly be tagged, but it also degrades the resolution on the primary vertex and thus reduces the tagging efficiency for the b quark in the other hemisphere. This relatively large effect can be avoided by reconstructing a primary vertex independently in the two hemispheres.

Combining more tags reduces the number of parameters that have to be taken from simulations and can be determined from the data instead, and hence helps in reducing systematic uncertainties. Particularly useful are combinations of b, c and uds tags. The tags are assigned certain priorities, and only the highest priority tag in a hemisphere is counted if more than one tagging condition is fulfilled. Measuring the singly tagged fractions and the doubly tagged fractions, for the same tag or for mixed tags, determines the tagging efficiencies as well as the production fractions R_{b} and R_{c} of heavy quarks. These methods achieve high statistical precision with good control of systematic errors and were employed in measurements of $R_{\mathrm{b}} = \Gamma_{\mathrm{b\bar{b}}}/\Gamma_{\mathrm{h}}$.

8.2 Measurements of the b width

Results on R_b are summarised in Figure 8.1 . Almost all measurements are dominated by systematic errors. The most precise results are obtained using multiple tag techniques. Also shown on the figure is a recent result from the SLD detector at SLAC [92]; they exploit their excellent vertex detector and the very small beam spot of the SLC machine to obtain a competitive result, although their statistics amounts to only about 5 % of that of one LEP experiment.

The combined average is compared to the Standard Model prediction, indicated by the line showing the calculated value of R_b as a function of the top quark mass. Note that variations of Standard Model parameters within their errors are invisible compared to the thickness of the line. The average of the measurements prefers a very low value of the top mass. More details on the averaging are given in section 8.4 below.

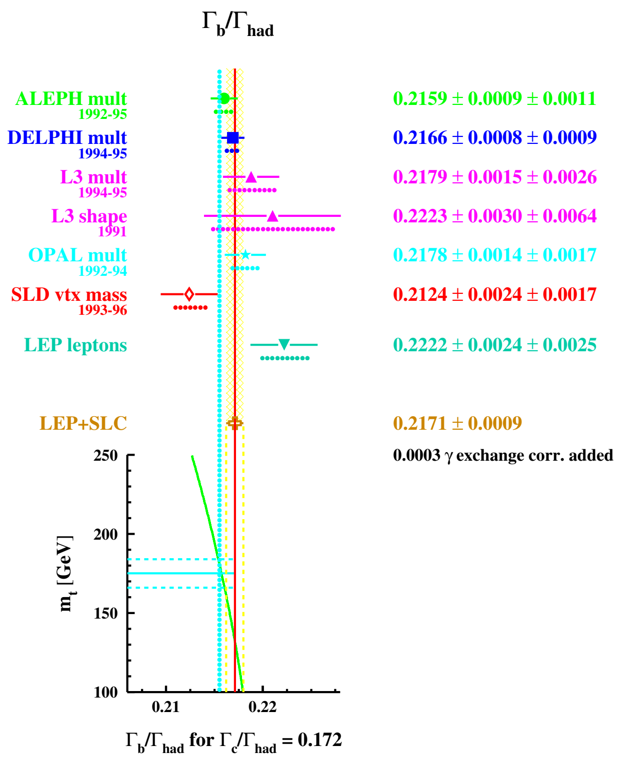

Figure 8.1: *Measurements of the ratio of the* Z *decay width to* b *quarks and the hadronic width, R_b, by the four LEP experiments. R_b is correlated with the value used for R_c, which has been set to its Standard Model expectation of $R_\mathrm{c} = 0.172$. Shown as the error bar on each measurement is the combination of the statistical and systematic errors. The second error below each measurement illustrates the estimated size of the systematic error.*

8.3 Forward-backward asymmetries

Measurements of the forward-backward asymmetry of heavy quarks require the reconstruction of the direction of flight and the charge of the produced quark or anti-quark.

The charge and direction of the lepton in lepton tags provide an estimator for both. The same is true for tagging methods using exclusively reconstructed particles. Monte Carlo simulations provide the small corrections needed to account for the difference in direction of flight between the decaying b or c hadron and the reconstructed particle.

To exploit the high statistics of vertex tags the separation between quarks and anti-quarks has to be achieved by the use of hemisphere charge techniques [93, 94, 95].

The hemisphere charge, Q_{hem}, is a momentum weighted sum of the charges of tracks in an event hemisphere, typically defined as

$$Q_{hem} = \frac{\sum_i Q_i |p_i^{\parallel}|^{\kappa}}{\sum_i |p_i^{\parallel}|^{\kappa}} , \tag{8.2}$$

where Q_i is the charge of track i, and $p_i^{\parallel}$ is the momentum component along the thrust axis. κ is determined from hadronisation models to give optimal charge resolution, and is typically 0.5 for b quarks. The thrust axis of the event serves as a measure of the direction of the b quark, *i.e.* the scattering angle θ.

The forward-backward asymmetries are extracted from fits to the $\cos\theta$ distribution, assuming that the differential cross-section has the shape of equation 6.4 .

Several small corrections are necessary to arrive from the observed asymmetry determined this way at the pole asymmetry, $A_\mathrm{fb}^{0,\,\mathrm{b}}$, which only contains the Z contribution. The contribution from γ–Z interference, QED radiative corrections, the non-zero b quark mass and QCD corrections have to be taken into account. The measurements of the asymmetries were taken at different centre-of-mass energies, and therefore had to be corrected to the same energies of 89.55 GeV, 91.26 GeV and 92.94 GeV for the peak−2, peak and peak+2 data by taking the predicted energy dependence of the observed asymmetries from the Standard Model. This slope depends only on the axial-vector couplings of the initial and final state fermions and thus does not depend on the value of the asymmetry at the peak. The measured asymmetries are transformed to pole asymmetries in the sense of equation 5.12 by applying these corrections according to

$$A_\mathrm{fb}^0 = A_\mathrm{fb}^{meas} + \sum_i \delta A_\mathrm{fb}{}^i \; ; \tag{8.3}$$

the corrections $\delta A_\mathrm{fb}{}^i$ are summarised in Table 8.1 .

The QCD corrections depend strongly on the experimental cuts used to select events with b quarks and on the method to extract the asymmetry. It arises largely from the contribution of events with hard gluon radiation to the asymmetry and from the the difference between the quark direction and the thrust axis of the jet, which is used in the

Source	$\delta A_{\mathrm{fb}}^{\mathrm{b}}$	$\delta A_{\mathrm{fb}}^{\mathrm{c}}$
$\sqrt{s}$ from 91.26 GeV to m_Z	-0.0013	-0.0034
QED corrections	$+0.0041$	$+0.0104$
b mass, γ, $\gamma - Z$	-0.0003	-0.0008
QCD corrections (approx.)	$+0.003$	$+0.002$
	± 0.001	± 0.001

Table 8.1: *Corrections to be applied to the measured quark asymmetries at $\sqrt{s} = m_Z$. QED corrections were calculated with ZFITTER, QCD corrections according to reference [96]. Note that experimental cuts can lead to QCD corrections different than quoted in the table.*

analyses. The QCD correction reduces the asymmetry and may be written as

$$A_{\mathrm{fb}}^{QCD} = (1 - \mathcal{B}\delta\frac{\alpha_s}{\pi})A_{\mathrm{fb}}^{0}\,, \tag{8.4}$$

where δ is a factor from theoretical calculations, and $\mathcal{B}$ is an experimental bias factor. δ also depends on hadronisation effects and therefore, in practice, its value has to be taken from hadronisation models [48, 49]. The size of δ is about 0.8, with a substantial model dependence. The experiments use detailed detector simulations in addition to the hadronisation models to determine $\mathcal{B}$, which typically reduces the actual correction to be applied by about a factor of two, albeit with some variation between different analyses and methods [97].

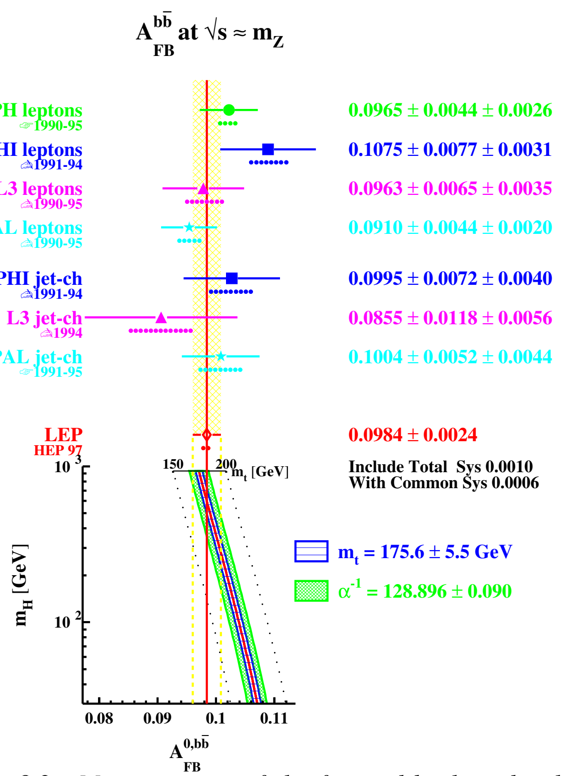

Figure 8.2: *Measurements of the forward-backward pole asymmetry for b quarks, $A_{\mathrm{fb}}^{0,\mathrm{b}}$, by the four LEP experiments. Shown as the error bar on each measurement is the combination of the statistical and systematic errors; the systematic error is indicated by the second error bar below each measurement.*

Results on the existing measurements of the $\mathrm{b\bar{b}}$ forward-backward asymmetry of b quarks, and the data sets used by each of the four LEP experiments are shown in Figure 8.2 . Since $A_{\mathrm{fb}}^{0,\mathrm{b}}$ is correlated with the value taken for R_{c}, each measurement has been correctied to the Standard Model expectation of $R_{\mathrm{c}} = 0.172$ for the purpose of this plot. In all cases, the estimated systematic errors, also indicated in the figure, are about a factor two smaller than the statistical errors. Comparison with the Standard Model prediction, expressed as a function of the Higgs mass and with variations from the electromagnetic coupling constant and the top quark mass within the ranges indicated in the figure, shows that the average prefers a high value of the Higgs mass.

The off-peak statistics collected by the LEP experiments lead to measurements of the b and c quark asymmetries at the peak of the Z resonance and about 2 GeV above and below. Averages of measurements at different energies are shown in Figure 8.3; the energy dependencies also agree well with the expectation from the Standard Model.

For more details on the combined results see subsection 8.4 and Table 8.2 .

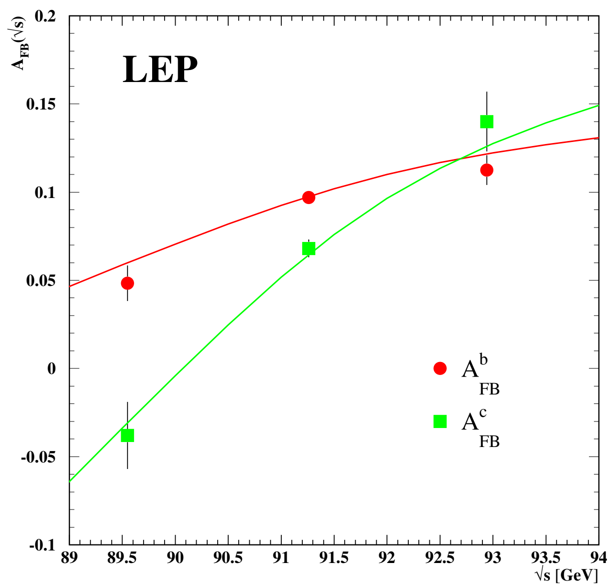

Figure 8.3: *Average of measurements by the LEP experiments of the b and c quark forward-backward asymmetries as a function of the centre-of-mass energy. The solid lines indicate the Standard Model prediction.*

8.4 Combination of results on heavy quarks

The experimental analyses not only determine the observables interesting to electroweak physics, but at the same time determine semi-leptonic branching ratios of b and c

LEP only		correlation matrix			
		R_b	R_c	$A_{fb}^{0,b}$	$A_{fb}^{0,c}$
R_b	0.2174 ± 0.0009	1.00	−0.22	−0.03	0.02
R_c	0.1727 ± 0.0050		1.00	0.03	−0.08
$A_{fb}^{0,b}$	0.0983 ± 0.0024			1.00	0.13
$A_{fb}^{0,c}$	0.0739 ± 0.0048				0.13

LEP & SLC		correlation matrix					
		R_b	R_c	$A_{fb}^{0,b}$	$A_{fb}^{0,c}$	$\mathcal{A}_b$	$\mathcal{A}_c$
R_b	0.2170±0.0009	1.00	−0.20	−0.03	0.01	−0.03	0.02
R_c	0.1734±0.0048		1.00	0.03	−0.07	0.04	−0.04
$A_{fb}^{0,b}$	0.0984±0.0024			1.00	0.13	0.03	0.02
$A_{fb}^{0,c}$	0.0741±0.0048				1.00	0.00	0.07
$\mathcal{A}_b$	0.900 ±0.050					1.00	0.08
$\mathcal{A}_c$	0.650 ±0.058						1.00

Table 8.2: *Combined results on measurements of decay fractions into b and c quarks and of asymmetries from the 1990 - 1995 data of the four LEP experiments (upper part) and combination with results from SLC (lower part) (from [44]). The results are still preliminary.*

quarks, the fragmentation parameters, $\langle x_E \rangle_b$ and $\langle x_E \rangle_c$, and the average b mixing parameter, $\overline{\chi}$. $\langle x_E \rangle_b$ and $\langle x_E \rangle_c$ represent the fraction of the beam energy carried by the b and c hadron, respectively. $\overline{\chi}$ describes the probability that a hadron containing a $\overline{b}$ quark decays as its anti-particle, containing a b quark. The fragmentation probabilities of c quarks into charmed mesons and baryons enter into measurements relying on charm suppression or on charm tags. These additional quantities introduce correlations among the electroweak parameters discussed above and are all determined from measurements at LEP. The combination of heavy flavour results from LEP and SLC is based on a multi-parameter fit which determines the eleven parameters $A_{fb}^{0,b}$, $A_{fb}^{0,c}$, R_b, R_c, BR($b \to \ell$), BR($b \to c \to \ell$), $\overline{\chi}$ and the probabilities for c quarks to fragment into D^{*+}, D^+, D^0 or into charmed baryons [81, 98, 44]. The averages of parameters relevant to electroweak physics resulting from this combination and the reduced correlation matrix are shown in Table 8.2 . Recent results from SLD on R_b [92], R_c [99] and on the left-right forward-backward asymmetries [100] have similar systematics and were therefore also included in the averaging.

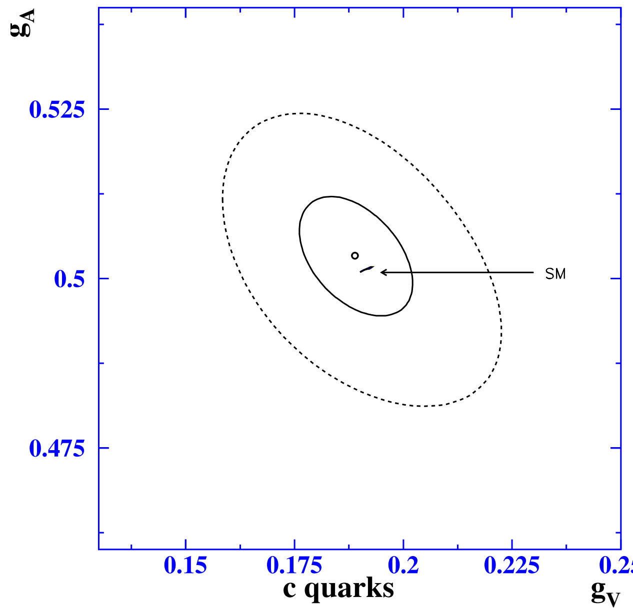

Figure 8.4: *Contour lines in the plane of vector and axial-vector couplings for c quarks; shown are the 1 σ and 95% confidence level contours. The black area indicates the Standard Model expectation.*

8.5 Couplings of heavy quarks

The many measurements of observables involving heavy quarks can conveniently be summarised by extracting the effective Z couplings to b and c quarks. In particular, the measurements of the heavy quark asymmetries depend more strongly on the value of the electron vector coupling than on the quark couplings (see section 5.5), and therefore the errors on the quark couplings are rather large.

Information about the quark couplings is extracted from a fit using all leptonic asymmetry-type measurements, including τ polarisation and the SLC A_{lr} measurement, together with the b and c partial decay widths and the measured b and c quark asymmetries at three energies at and around the Z pole as well as the determinations of $\mathcal{A}_b$ and $\mathcal{A}_c$ at the SLC. Contour lines of such fits are shown on figures 8.4 and 8.5, where a comparison with the Standard Model expectation is also indicated by the small black area.

The errors on the heavy quark couplings are rather large

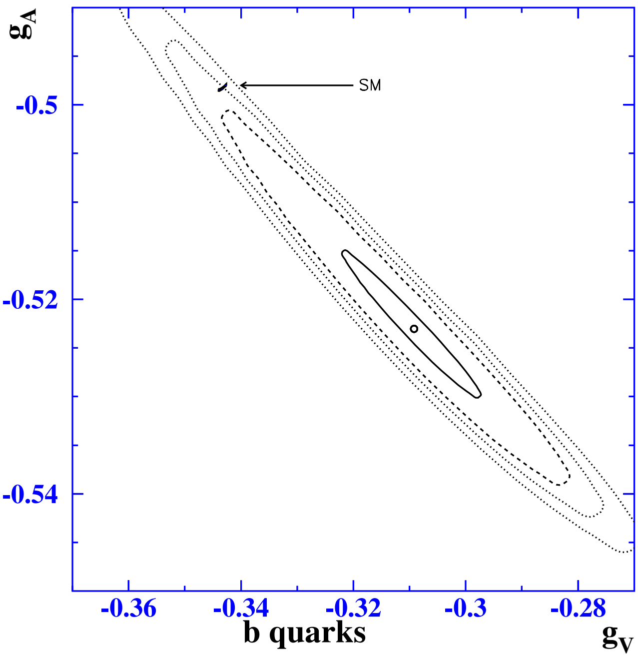

Figure 8.5: *Contour lines in the plane of vector and axial-vector couplings for b quarks; shown are the 1 σ and the 95%, 99% and 99.9% confidence level contours. The black area indicates the Standard Model expectation.*

compared with the ranges of the Standard Model prediction. Good agreement with the expectations is observed for the c quark couplings, but the b quark couplings show a disagreement with the Standard Model expectation at the 99% confidence level. One reason for this large disagreement in this two-dimensional representation is the deviation of the average partial decay width into b quarks, $R_b \propto \hat{g}_v^{b\,2} + \hat{g}_a^{b\,2}$, from the Standard Model, which is close to two standard deviations. Another reason is the relatively low value of the average forward-backward asymmetry measurements of b quarks, $\propto \mathcal{A}_e\mathcal{A}_b$, which results in a low value of $\mathcal{A}_b$ when the combined LEP and SLC measurements of the leptonic asymmetry parameter, $\mathcal{A}_\ell$, are used to extract the b quark asymmetry parameter $\mathcal{A}_b$ [†]. This is shown more clearly in Table 8.3, which gives the values of $\mathcal{A}_b$ and $\mathcal{A}_c$ extracted separately from the LEP and SLC data. There is good agreement between $\mathcal{A}_b$ solely from the LEP measurements and the Standard Model value of $\mathcal{A}_b = 0.9344 \pm 0.0005$; there is also good agreement with the value obtained from the left-right forward-backward asymmetry of b quarks at SLC. However, with $\mathcal{A}_\ell$ taken from the combined leptonic LEP data and the SLD measurement of A_{lr} a significant discrepancy with the Standard Model of 2.5 standard deviations appears.

Therefore, the large disagreement with the Standard Model shown in Figure 8.5 is the manifestation of three slight problems in the present data, which each in itself is

$\mathcal{A}_b$	$\mathcal{A}_c$
LEP ($\mathcal{A}_\ell = 0.1461 \pm 0.0033$)	
0.897 ± 0.030	0.674 ± 0.046
SLD	
0.900 ± 0.050	0.650 ± 0.058
LEP+SLD ($\mathcal{A}_\ell = 0.1505 \pm 0.0023$)	
0.877 ± 0.023	0.653 ± 0.037

Table 8.3: *Asymmetry parameters $\mathcal{A}_b$ and $\mathcal{A}_c$ of b and c quarks from LEP data alone with LEP average $\mathcal{A}_\ell$, from SLD, and from LEP+SLD with the LEP+SLD average value for $\mathcal{A}_\ell$.*

not really serious. The fact that all three show up in a plot of the b quark couplings may just be a random coincidence. This deserves further experimental clarification.

For completeness, the b quark couplings expressed as left and right-handed couplings are shown in Figure 8.6. Of course, the same discrepancy with the Standard Model shows up here, but, taking it seriously, one might argue that the deviation from the Standard Model appears to be more in the right-handed than in the left-handed couplings.

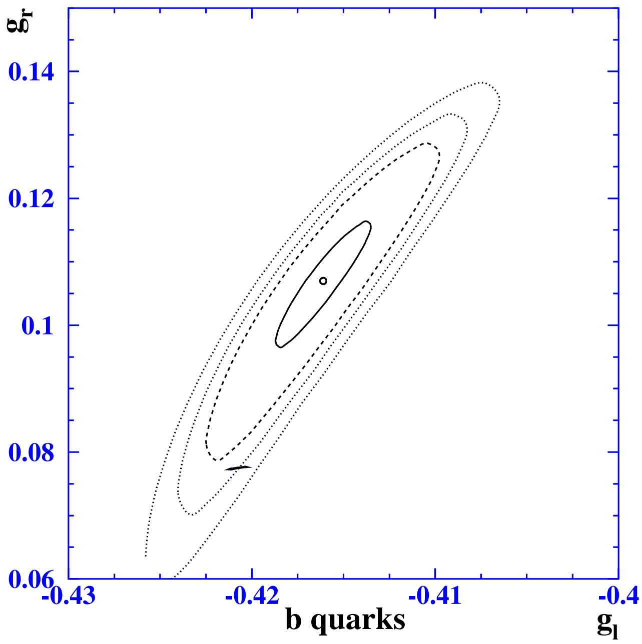

Figure 8.6: *Left and right-handed couplings of b quarks; 1 σ, 95%, 99% and 99.9% confidence level contours are shown.*

[†] As will be pointed out in section 10.2, there is only very poor agreement among the various determinations of the effective leptonic weak mixing angle, and hence in the various determinations of $\mathcal{A}_\ell$.

9 Other Standard Model parameters

An interpretation of the measurements at the Z resonance within the framework of the Standard Model requires knowledge about the other input parameters, namely the electromagnetic and the strong coupling constants and the mass of the top quark, and also the mass of the Higgs boson. Measurements of the mass of the $W^\pm$ boson and of the weak mixing angle in neutrino scattering experiments provide important consistency checks of the theory on the one hand and contribute to the knowledge on m_H on the other. A brief description of the present experimental situation concerning these other parameters and observables and the status of searches for the Higgs boson and for physics beyond the Standard Model are therefore presented in this chapter.

9.1 The electromagnetic coupling constant

Although at low energies the electromagnetic coupling constant, or fine structure constant, is known with an impressive precision of 40 ppb [14], its value at the scale of the Z mass $\alpha(m_Z)$, which is modified by vacuum polarisation effects, has a much lower precision of only ~700 ppb. At an energy scale $\sqrt{s}$, $\alpha(s)$ is given by

$$\alpha(s) = \frac{\alpha}{1 - \Delta\alpha(s)}\,,$$

where $\Delta\alpha(s)$ is the contribution from photon vacuum polarisation. The leading contribution is from light fermion loops in the photon propagator. For leptons, this is precisely calculable from QED; for light quarks, however, the non-perturbative nature of QCD contributions at small energies and ambiguities in the definition of the light quark masses do not permit a reliable calculation within the framework of QCD. Since the evaluation of the quark loop diagrams can be related to measurements of the hadronic cross-section, experimental data on $q\overline{q}$ production in e^+e^- annihilation are used as input. With the help of a dispersion relation and the optical theorem the hadronic contribution, $\Delta\alpha_{\mathrm{had}}(m_Z)$, can thus be determined, at the price of a significant experimental uncertainty entering into the value for $\alpha(m_Z)$. Most of this uncertainty arises from low-energy data due to the complicated resonance structure at these energies, the precision of the measurements and various assumptions that need to be made when combining results from different experiments. The energy range from 1 to 12 GeV contributes about 50% to the correction $\Delta\alpha_{\mathrm{had}}(m_Z)$, but constitutes over 80% of its uncertainty. Recent re-evaluations [22, 101, 102, 103] of an earlier work [104] show quite good consistency. A good overview may be obtained from reference [103].

For results presented in this review, a value of $\Delta\alpha_{\mathrm{had}}(m_Z) = 0.0280 \pm 0.0007$, corresponding to $\alpha(m_Z) = 1/(128.896 \pm 0.090)$ [22], is used.

Slightly stronger experimental constraints on $\Delta\alpha_{\mathrm{had}}(m_Z)$ can be obtained by using in addition measurements of τ lepton decays into two or four pions [105]. The result is consistent with the value given above, and the estimated error is about 5 % smaller.

There also are determinations of the electromagnetic coupling constant relying heavily on quasi-analytical approximations of the cross-section $e^+e^- \to$ hadrons at low energies [106]. The quoted errors are smaller by ~30 % compared to the value given above as the default for this note. Another very recent evaluation [107] also uses τ data and in addition employs QCD calculations based on a Wilson Operator Product Expansion down to 1.8 GeV to improve on the $e^+e^- \to$ hadrons cross-section measurements. The quoted error of only 0.0036 on $1/\alpha(m_Z)$ is surprisingly low, and the central value obtained is very consistent with the above value. If this work is used in analyses of electroweak data a substantial dependence of electroweak physics on non-perturbative QCD calculations will be introduced.

Clearly the value of the electromagnetic coupling constant at the scale of the Z mass has become one of the limiting input parameters to any Standard Model calculation and will therefore trigger much further activity over the coming years, both experimentally and theoretically.

9.2 The strong coupling constant

The strong coupling constant, α_s, is fixed with high precision by the data taken at the Z resonance through the QCD correction δ_{QCD} to the hadronic decay width of the Z, which has been calculated to third order in α_s/π. Using this value of α_s in all Standard Model calculations minimises uncertainties from QCD in the predictions of electroweak precision observables. However, as a test of QCD it is important to compare the results on α_s from the Z resonance to results obtained from QCD studies at other energies and from other observables.

Recent reviews of determinations of α_s [108, 14] all give approximately the same central value, but differ substantially in the errors assigned to it. The list of α_s determinations from a variety of processes at different energies is long, and all suffer from substantial systematic errors due the effect from the omission of higher orders in the QCD calculations. Although the errors quoted on individual measurements are typically around ± 0.005, an analysis of the scatter of the measurements shows that the shape of this distribution is far from being Gaussian, and the measurements are strongly correlated through theoretical errors. Different authors use different methods to estimate the effect of the dominating theoretical uncertainties on the mean. If one simply requires 68 % of the measurements to be within the assigned error band around the mean, an error estimate of ± 0.005 is obtained. More optimistic treatments introduce correlation coefficients between the different measurements and thus force the χ^2-value of the combination to be one per degree of freedom, leading to an error on the mean of only ± 0.003.

In summary, the average value of the strong coupling constant evolved to the scale of the Z mass is 0.118, with an error of $\pm$(0.003 to 0.006). In this average, the determination of α_s from the hadronic Z width is not used.

9.3 The top quark mass

Direct measurements of the mass of the top quark, m_{t}, are of fundamental importance in the Standard Model. The large value of m_{t} makes electroweak corrections involving the top quark dominating other effects. It is vital to check that the top-dependent corrections within the Standard Model are as predicted, and a precise knowledge of m_{t} from direct measurements is a precondition to become sensitive to other radiative effects, *e. g.* due to the Higgs boson.

Since the top quark was discovered at the Tevatron $\mathrm{p\bar{p}}$ collider at Fermilab [13], its mass has been determined by the CDF and DØ experiments with a relative precision that is better than our knowledge of any other quark mass. The pair-produced top quarks each decay dominantly into a b quark and a W boson, which allows a clean identification of events containing top quarks. The top quark mass is reconstructed from these decay products. Different experimental techniques have to be used depending on the W decay modes to either quark pairs or into a charged lepton and a neutrino. Good consistency among the different methods and experiments is achieved. The results are summarised in Table 9.1; with an assumed common error between the CDF and DØ measurements of 3 GeV the average value is [15]

$$m_{\mathrm{t}} = 175.6 \pm 5.5\,\mathrm{GeV}\,.$$

	m_{t} [GeV]
CDF average	176.8 ± 6.5
DØ average	173.3 ± 8.4
average	175.6 ± 5.5

Table 9.1: *Measurements of the top quark mass (from [15]).*

9.4 The W boson mass

The W boson mass is sensitive to genuine electroweak corrections via loops involving the top quark and the Higgs boson. With m_{Z}, the weak, strong and electromagnetic coupling constants, the top quark mass and the Higgs boson mass as input to Standard Model calculations the W mass is predicted and therefore provides a powerful consistency test.

Measurements of the W boson mass in $\mathrm{p\bar{p}}$ collisions were performed at the CERN $\mathrm{Sp\bar{p}S}$ [109] and at the Tevatron at Fermilab by the CDF [110] and DØ [111] collaborations. The W mass has to be determined from the transverse momentum components of its decay products w.r.t the beam line, because the large number of particles close to the beam pipe prevents the usage of longitudinal momentum components. The spectrum measured in the "transverse mass" of W decay products is used to extract the W mass. Common errors of 50 MeV between the two most precise measurements originate from the proton structure functions and from the assumed transverse momentum spectrum of the produced W bosons.

Since 1996 LEP operates at centre-of-mass energies beyond the threshold for W pair production. At the energy of 161 GeV the W mass is extracted by comparing the measured production cross-section with the predicted one as a function of the W mass. At higher energies, the W mass is reconstructed from the W decay products, in the $\mathrm{W}\to \mathrm{q\bar{q}q\bar{q}}$ and $\mathrm{W}\to \mathrm{q\bar{q}}\ell\nu$ decay channels [112]. All LEP measurements are affected by a common error of 30 MeV from the uncertainty in the beam energy, and the measurements in the $\mathrm{q\bar{q}q\bar{q}}$ channel suffer from a QCD uncertainty at present estimated to be as large as 100 MeV from gluon exchange between the decay products of the two W bosons in an event ("colour reconnection" [113]).

The measurements of the weak mixing angle in neutrino-nucleon scattering experiments can also be interpreted as a measurement of the W boson mass (see section 9.5).

All precision measurements of the W boson mass are summarised in Table 9.2 . The present world average value, including the neutrino experiments, is

$$m_{\mathrm{W}} = 80.41 \pm 0.07\,\mathrm{GeV}\,.$$

9.5 Neutrino-nucleon scattering

Neutrino scattering experiments [43] determine the ratio of charged-to-neutral current events by detection of neutrino interactions with or without a charged lepton in the final state. The Z-mediated neutral currents depend on the right- and left-handed couplings of the Z to quarks and hence on the weak mixing angle (see equation 2.3), which can be extracted from the measured neutral-to-charged current ratio observed when neutrinos collide with an iso-scalar target.

experiment	m_W [GeV]
colliders	
UA2	80.36 ± 0.37
CDF	80.38 ± 0.12
DØ	80.44 ± 0.11
average colliders	80.41 ± 0.09
neutrino scattering	
νN average	80.25 ± 0.19
LEP II	
ALEPH	80.51 ± 0.24
DELPHI	80.33 ± 0.26
L3	80.75 ± 0.26
OPAL	80.35 ± 0.25
average LEP II	80.48 ± 0.14
world average	80.41 ± 0.07

Table 9.2: *Precision measurements of the W boson mass.*

Corrections to the weak mixing angle in such reactions arising from electromagnetic and electroweak radiative corrections and from the modelling of the quark content of the nucleon are small; therefore the measured weak mixing angle corresponds to the one in the on-shell renormalisation scheme, given by $\sin^2\theta_W = 1 - m_W^2/m_Z^2$. In combination with the very precise Z mass from LEP these measurements therefore are equivalent to a measurement of the mass of the W boson, m_W, and are sensitive to the same type of electroweak radiative corrections as the W mass.

The earlier measurements by the CHARM and CDHS experiments at CERN are now being improved by the CCFR collaboration at Fermilab. The most precise measurement by CCFR has about equal contributions from statistical and systematic errors. The experimental systematic errors are dominated by the uncertainty in the ν_e component in the ν_μ beam. The largest contribution to the total error arises from theoretical uncertainties in the modelling of the quark content in the nucleon, which is dominated by the uncertainty in the effective mass of the charm quark affecting charged current charm production. The CCFR result is

$$\begin{aligned}\sin^2\theta_W &= 0.2236 \pm 0.0028(\text{exp.}) \pm 0.0030(\text{theor.}) \\ &\quad + 0.0006 \times \left(\frac{m_t^2 - (175\text{ GeV})^2}{(100\text{ GeV})^2}\right) \\ &\quad + 0.0002 \times \log_e\left(\frac{m_H}{150\text{ GeV}}\right).\end{aligned}$$

Note that the residual dependence on the top quark and Higgs boson masses is small compared to the experimental errors.

The values quoted by the CERN experiments have to be corrected to a heavy top, since, at the time, they were given for values as low as m_t=45 GeV respectively m_t=60 GeV; this results in

CHARM :	$0.234 \pm 0.005 \pm 0.005(\text{theor.})$
CDHS :	$0.225 \pm 0.005 \pm 0.005(\text{theor.})$
average :	$0.2295 \pm 0.0035 \pm 0.005(\text{theor.})$

The last line was derived assuming that the theoretical errors between these experiments are fully correlated. The residual uncertainty from the top quark and Higgs boson mass, within the Standard Model, is $\lesssim 0.001$, which is small compared to the other errors.

Common errors between the CERN and Tevatron experiments arise from the uncertainty in the charm quark mass, non-isoscalar corrections, the charmed sea or the structure functions of the nucleon and are estimated to be 0.003 for the CERN experiments and 0.002 for CCFR. Taking these correlated errors into account leads to an average of all measurements [114] of $\sin^2\theta_W = 0.2254 \pm 0.0037$. This corresponds to a value of the W boson mass of $m_W = (80.25 \pm 0.19)$ GeV for $m_Z = (91.1867 \pm 0.002)$ GeV.

9.6 Searches for the Higgs boson

The lower mass bound on the Higgs boson mass obtained from the six years of LEP I running at the Z resonance [115] is significantly improved by data taken at higher energies at LEP II. Results from the running up to 1996 at energies between 130 GeV and 172 GeV have recently been presented [116]. The dominant contribution comes from an integrated luminosity of $\sim$20 pb^{-1} per experiment taken at energies of 161 GeV and 172 GeV. No evidence of direct Higgs boson production was reported, and all experiments give lower limits on the Higgs boson mass; these are 70.7 GeV (ALEPH), 66.2 GeV (DELPHI), 69.5 GeV (L3) and 69.4 GeV (OPAL).

Higgs bosons at LEP would be radiated off a virtual Z boson produced in the e^+e^- annihilation. The Higgs boson decays mainly ($\sim$86 %) to $b\bar{b}$ final states, and therefore most searches are restricted to this channel. Some sensitivity is also gained by looking for Higgs boson decays into τ leptons. The result from the search by the OPAL experiment at centre-of-mass energies around m_Z is shown as an example in Figure 9.1 . Three candidates are selected, in the $(H \to q\bar{q})(Z \to \nu\bar{\nu})$ channel with a mass of 39.3 GeV, in the leptonic channel with a mass of 61.2 GeV and in the four jet channel with a mass of 75.6 GeV. The two high-mass candidates are responsible for the bumps of the dashed line shown in Figure 9.1, which represents the upper limit on the the number of produced Higgs bosons at 95 % confidence level. This is compared with the Standard Model expectation for the number of produced Higgs bosons as a function of the Higgs boson mass; the intersection with the full line gives the lower limit on the Higgs boson mass quoted above.

The combination of the individual limits by the experiments is a complex task and has recently been performed by a dedicated working group [117]. The individual experiments use slightly different statistical methods to deal with backgrounds and candidate events in the searches; all of these methods are identical in cases where no candidates are observed. Using each of the proposed methods in turn

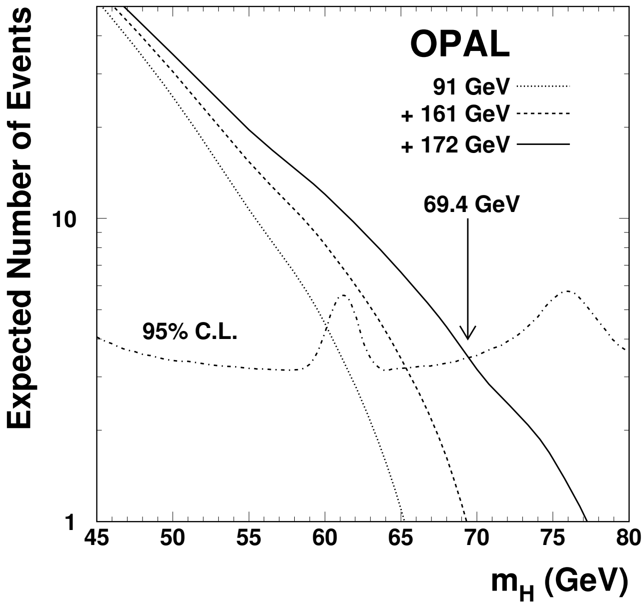

Figure 9.1: *Limit from direct search for the Higgs boson by the OPAL experiment.*

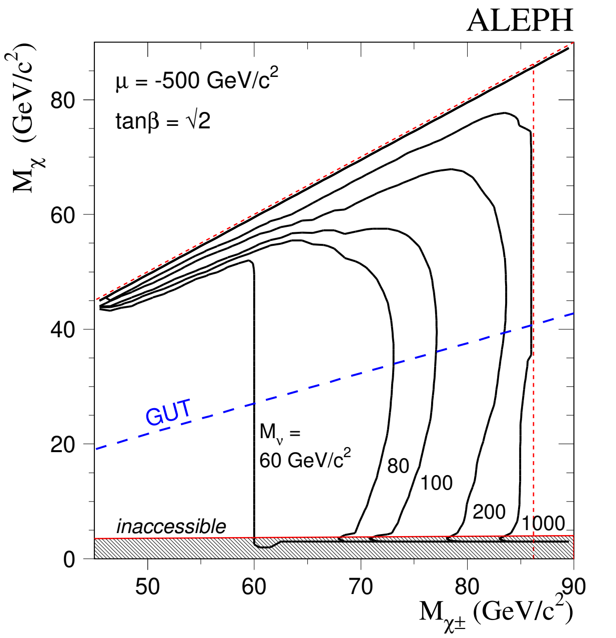

Figure 9.2: *Limit contours in the plane of the masses of the lightest neutral super-symmetric particle and the chargino, the super-symmetric partner of the W boson, from a search performed by the ALEPH experiment. The limit is very sensitive to the assumed mass of the partner of the neutrino; this is shown for different values.*

to determine the combined limit leads to very similar results ranging between 77.5 GeV and 77.9 GeV. The lowest of the obtained combined limits is a conservative estimate of the lower limit on the Higgs boson mass,

$$m_H < 77.5\ \mathrm{GeV}\ @\ 95\,\%C.L.\,.$$

9.7 Searches for physics beyond the Standard Model

The energy of LEP has reached 183 GeV at present and opened a new regime for various searches for new particles not expected within the Standard Model. In particular a "super-symmetric" extension assigning a bosonic partner to each fermion and a fermionic partner to each boson in the Standard Model is very appealing from a theoretical point of view [118] and has attracted appreciable attention in the past.

The signature in most of these searches is missing energy in events carried away by the non-interacting lightest super-symmetric particle, which is believed to be stable, electrically neutral and therefore non-interacting with normal matter. Direct searches for such particles assuming various scenarios all gave negative results. An example of such a search is shown in Figure 9.2 from an analysis of data taken at energies up to 172 GeV. Due to its large expected cross-section, the existence of a super-symmetric parter of the W bosons, the chargino, which can mix with the partner of charged Higgs boson also necessary in the super-symmetric theory, can be ruled out up to the kinematic limit at halve the centre-of-mass energy. Only for very special choices of model parameters the limit is lower; improved statistics will soon allow to access also this region. Searches for super-symmetric partners of the charged leptons were also performed and showed negative results, albeit with still lower mass limits due to the smaller expected cross-sections.

So far, no direct evidence for the existence of super-symmetric particles of any kind has been found at LEP [119].

Super-symmetry has only been chosen as one example of the many searches for new phenomena performed at LEP I and LEP II. No particles outside the Standard Model expectation have been found at presently accessible energy scales. Therefore consistency checks of precision measurements remain the only way to obtain indications for a possible incompleteness of the Standard Model, which would point to physics beyond it.

10 Interpretation within the Standard Model

Numerous precision measurements with high sensitivity to Standard Model parameters have been presented in the previous chapters. These measurements are essentially model-independent and determine corrections to the tree-level values of the Veltman parameter, ρ, the weak mixing angle, $\sin\theta_{\mathrm{W}}$, or the W mass, m_{W}. Provided the Standard Model is valid without modifications at an energy scale $O(100\ \mathrm{GeV})$ these measurements should show good consistency if interpreted within the framework of the Standard Model. Among the input parameters, the Z mass, the Fermi constant, the electromagnetic and strong coupling constants at the scale of the Z mass, the fermion masses and the Higgs boson mass, only the latter is experimentally unknown, apart from the lower limits that could be put on its mass from the non-observation of its production at LEP II energies up to 172 GeV. Imprecise knowledge of some other parameters limits the accuracy of our interpretation within the Standard Model; this is particularly true of the electromagnetic coupling constant. Indirect information on the Higgs boson mass may be obtained from electroweak loops involving the Higgs boson as a virtual particle. However, their contribution is quite small and other uncertainties entering into the Standard Model calculations due to imprecisely measured parameters ("parametric errors") or due to missing higher orders (genuine "theoretical uncertainties") become important.

The internal consistency of the electroweak precision measurements in combination with the question of the Higgs boson mass will be investigated in the following sections.

10.1 Summary of electroweak precision measurements

The electroweak precision measurements described in the previous chapters are summarised in Figures 10.1, 10.2 and 10.3 and in Table 10.1 . The central values and total errors are indicated by the vertical band on each plot; the graphs show the Standard Model expectation, where the different shaded areas indicate the effect of uncertainties in the input parameters: the dark area in the centre represents the variation of the prediction with the Higgs mass for 75 GeV $< m_{\mathrm{H}} <$ 1000 GeV; the second area is the variation with the strong coupling constant for $\alpha_s = 0.118 \pm 0.003$; the light area at the edge gives the variation with the electromagnetic coupling constant at the scale of the Z mass, $1/\alpha(m_{\mathrm{Z}}) = 128.896 \pm 0.090$; the measured value of the mass of the top quark is also indicated as a horizontal band. As can be seen from the plots, all measurements agree well with the Standard Model prediction restricted to the range given by the measurement of the top quark mass.

The table shows the experimental results on all observables considered as well as the Standard Model prediction for each of them. The quantity labelled "Pull" in the last column is the deviation of each observable from the Standard Model prediction divided by its experimental error; the Standard Model parameters are chosen to be the ones of the fit to all precision data with free Higgs boson mass (see Table 10.3).

10.2 $\sin^2\theta_{\mathrm{W}}^{\mathrm{eff},\ell}$ and ρ^{eff}

The asymmetry-type measurements presented in the previous chapters all determine the effective leptonic weak mixing angle, whereas measurements of partial decay widths also depend on the effective leptonic Veltman parameter, ρ^{eff}. These parameters are each sensitive to different types of electroweak corrections at the Z resonance. It is therefore instructive to average the appropriate classes of measurements and extract from these the effective leptonic weak mixing angle and the ρ parameter, and to compare these with the Standard Model.

The asymmetry-type measurements, each averaged over the four LEP experiments, and the left-right cross-section asymmetry by the SLD collaboration are expressed in terms of the effective leptonic weak mixing angle and summarised in Figure 10.4 . The value of χ^2 per degree of freedom from the combination is rather large. The dominant contribution is due to a difference of approximately three standard deviations between the two most precise measurements, the average over measurements of the b quark forward-backward asymmetry, $A_{\mathrm{fb}}^{0,\mathrm{b}}$, by the four LEP experiments on the one hand, and the measurement of the left-right polarised cross-section asymmetry, A_{lr}, by the SLD collaboration at the SLC on the other hand.

The value of χ^2 per degree of freedom of 4.4/5 from the LEP experiments only is good, as can also be seen from Figure 10.4, and the most dramatic difference appears to be the discrepancy between the combined LEP measurements and the SLD value for A_{lr}. However, if the measurements are grouped differently before comparing averages, different conclusions may be drawn. E. g., it is interesting to note that the leptonic forward-backward asymmetries at LEP are in good agreement with the SLC measurement, whereas the τ polarisation measurements at LEP, and to some lesser extent also the quark charge asymmetry, tend to give a higher value closer to the one extracted from the b quark forward-backward asymmetry. It is clear that any such grouping of measurements contains a large degree of arbitrariness. In

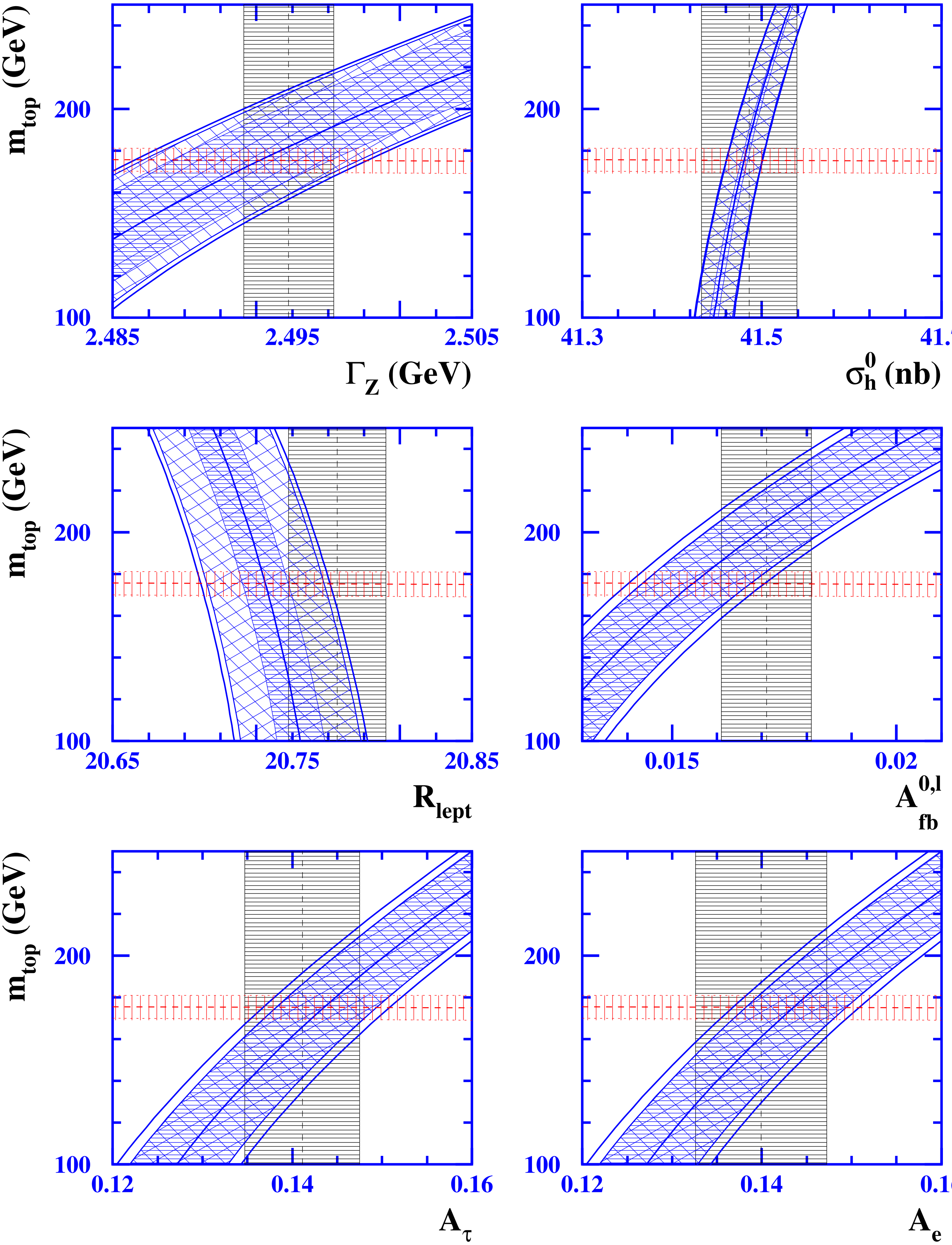

Figure 10.1: *Comparison of measured observables with the Standard Model, for the total Z width, the hadronic pole cross-section, the ratio of leptonic and hadronic decay widths, the leptonic pole forward-backward asymmetry, the average τ polarisation and $\mathcal{A}_e$ determined by the τ polarisation forward-backward asymmetry.*

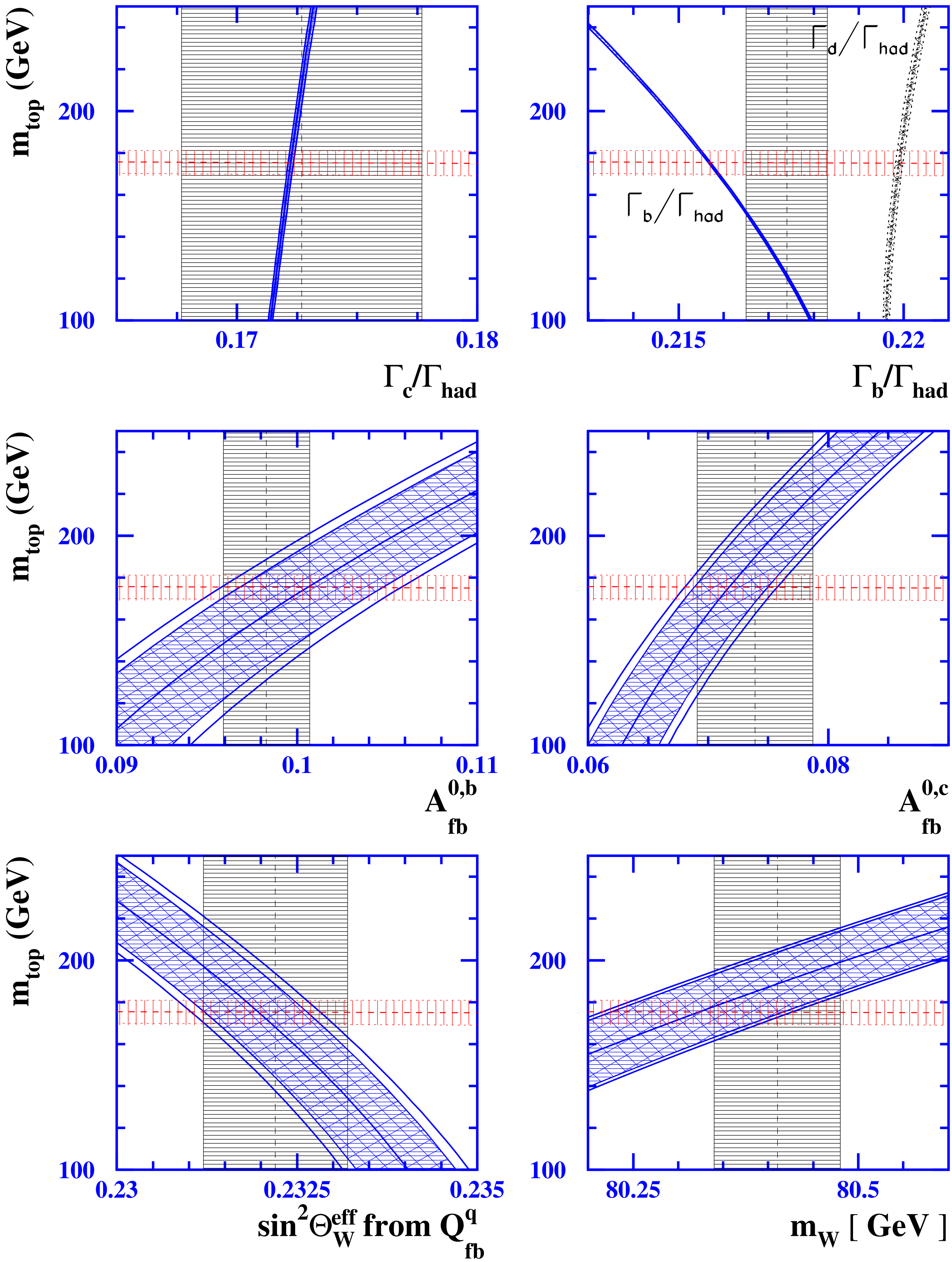

Figure 10.2: *Comparison of measured observables with the Standard Model, for the ratio of c and b quark partial widths to the total hadronic width, the b and c quark pole forward-backward asymmetries, the quark charge asymmetry and the W boson mass. On the second plot also the ratio of the down quark width to the hadronic width is indicated, which clearly shows the importance of the top-dependent* $Z-b\bar{b}$ *vertex corrections.*

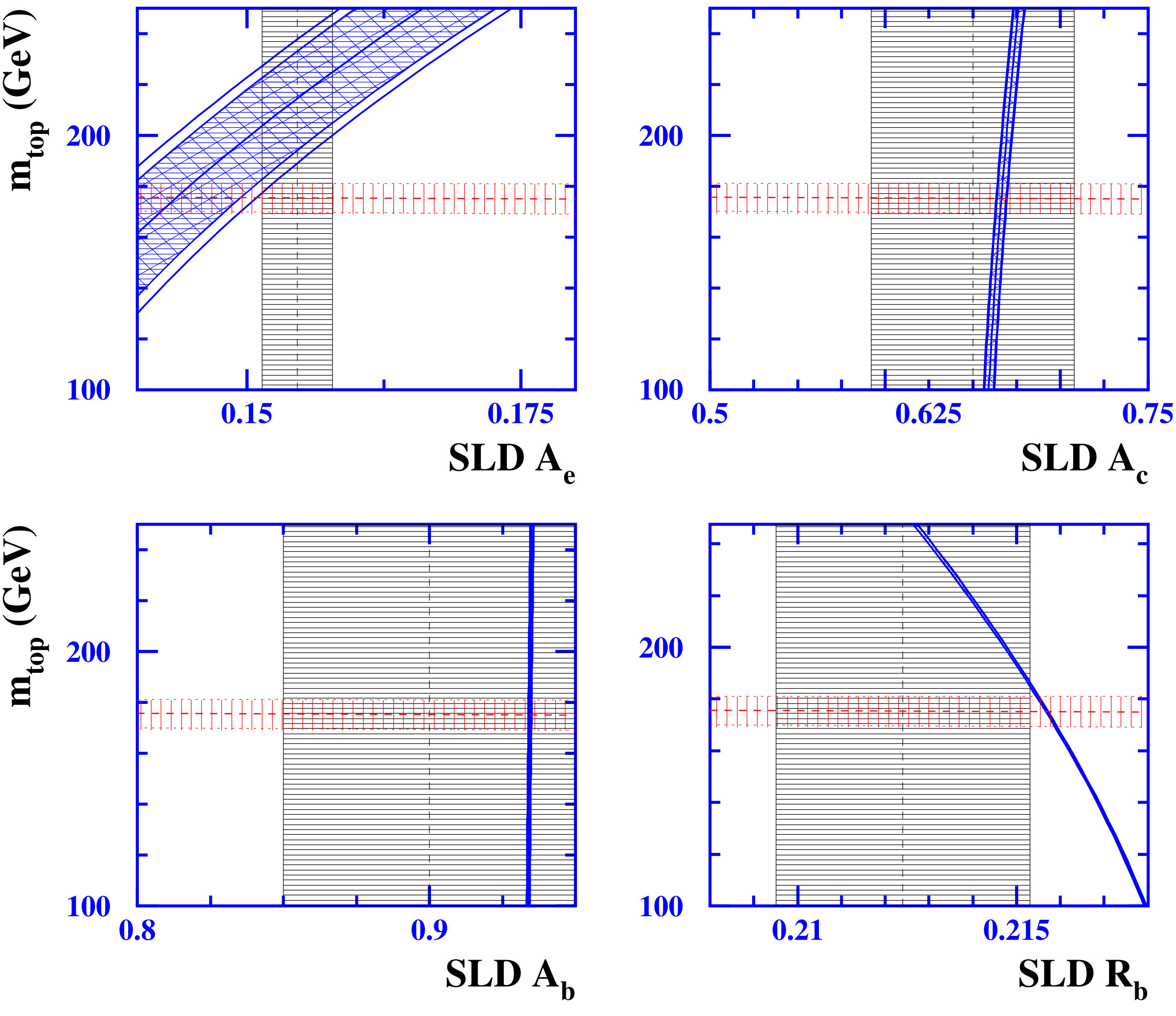

Figure 10.3: *Comparison of measured observables by the SLD collaboration with the Standard Model. Shown are pseudo-observables derived from measurements of the left-right polarisation asymmetry,* A_{lr}*, the c and b quark left-right forward-backward asymmetries,* $\mathcal{A}_{\mathrm{c}}$ *and* $\mathcal{A}_{\mathrm{b}}$*, and the ratio of the b-width to the hadronic width,* R_{b}.

	Measurement with Total Error	Standard Model	Pull
LEP I			
line-shape and lepton asymmetries:			
m_Z [GeV]	91.1867 ± 0.0020	91.1866	0.0
Γ_Z [GeV]	2.4948 ± 0.0025	2.4966	−0.7
σ_h^0 [nb]	41.486 ± 0.053	41.467	0.4
R_ℓ	20.776 ± 0.028	20.756	0.7
$A_{fb}^{0,\ell}$	0.0171 ± 0.0010	0.01622	0.9
+ correlation matrix Table 6.6			
τ polarisation:			
$\mathcal{A}_\tau$	0.1411 ± 0.0064	0.14708	−0.9
$\mathcal{A}_e$	0.1399 ± 0.0073	0.14708	−1.0
b and c quark results:			
R_b^0	0.2174 ± 0.0009	0.21580	1.8
R_c^0	0.1727 ± 0.0050	0.17228	−0.1
$A_{fb}^{0,b}$	0.0983 ± 0.0024	0.10310	−2.0
$A_{fb}^{0,c}$	0.0739 ± 0.0048	0.07366	0.1
+ correlation matrices Table 8.2			
$q\overline{q}$ charge asymmetry:			
$\sin^2\theta_W^{\mathrm{eff},\ell}$ ($\langle Q_{fb}\rangle$)	0.2322 ± 0.0010	0.23151	0.7
LEP II			
m_W [GeV]	80.48 ± 0.14	80.367	0.8
SLD			
$\sin^2\theta_W^{\mathrm{eff},\ell}$ (A_{lr})	0.23055 ± 0.00041	0.23151	−2.3
R_b^0	0.2124 ± 0.0029	0.21580	−1.2
R_c^0	0.1810 ± 0.0145	0.17228	0.6
$\mathcal{A}_b$	0.900 ± 0.050	0.9347	−0.7
$\mathcal{A}_c$	0.650 ± 0.058	0.6678	−0.3
$p\overline{p}$ **colliders**			
m_W [GeV]	80.41 ± 0.09	80.367	0.5
m_t [GeV]	175.6 ± 5.5	173.4	0.4
ν**N scattering**			
$\sin^2\theta_W$	0.2254 ± 0.0037	0.2232	0.6
(or m_W [GeV]	80.25 ± 0.19	80.367	−0.6)
$\alpha(m_Z)^{-1}$	128.896 ± 0.090	128.898	0.0

Table 10.1: *Summary of measurements of electroweak observables. Some or all of them serve as input to the various Standard Model fits presented in this chapter. The parameters used to calculate the Standard Model predictions in column three are taken from full fits to all input data given in this table, see Table 10.3 in subsection 10.4.2 . The numbers in column three are the averages of the three calculations considered in section 10.4; differences between them are in all cases smaller than nine units in the last quoted digit. The deviations of the measurements from this in units of the experimental error, labelled "Pull", are given in column four.*

conclusion there is no justified reason at present to mistrust and exclude certain measurements or classes of measurements from the average. The χ^2-probability derived from the value of χ^2 per degree of freedom of the full combination is still 5 %.

Taking all the measurements into account, the world average value of the effective leptonic weak mixing angle is

$$\sin^2\theta_W^{\mathrm{eff},\ell} = 0.23152 \pm 0.00023 .$$

The experimental error is already small compared to the theoretical uncertainties in the Standard Model prediction. The contribution arising solely from the error in the value of the electromagnetic coupling constant at the Z scale is $\pm$ 0.00023, and other theoretical uncertainties are estimated to be approximately ± 0.0001 [17]. The first one is dominant and limits the interpretation of the measured effective weak mixing angle in the framework of the Standard Model, and therefore improved determinations of $\alpha(m_Z)$ have to complement future improvements on the measured effective weak mixing angle. Important improvements are mainly expected from increased statistics in future running at the SLC; these will help to clarify the present experimental situation.

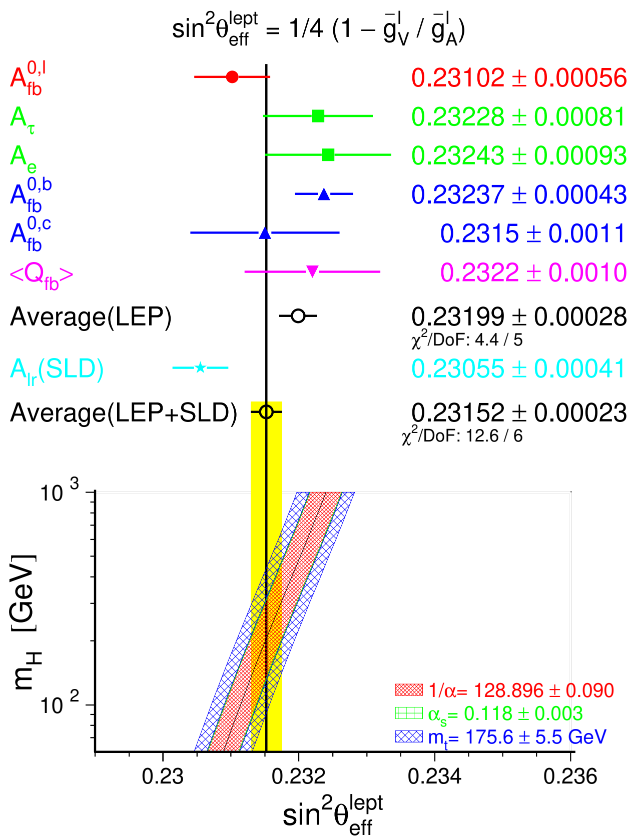

Figure 10.4: *Measurements of the effective leptonic weak mixing angle and comparison with the Standard Model.*

Measurements of the partial decay widths of the Z are sensitive to both the weak mixing angle and the effective ρ parameter through the vector and axial-vector couplings of the initial and final state fermions. In leptonic final states, the sensitivity to the weak mixing angle is very small, because the axial-vector couplings are much larger than the vector couplings (see Table 7.2). In practice, all the sensitivity to ρ^{eff} comes from the measurements of the leptonic decay width at LEP, since QCD effects and the uncertainty in the strong coupling constant lead to a very much reduced precision in ρ^{eff} extracted from hadronic measurements.

The result obtained from Γ_ℓ alone is a value of $\rho^{\mathrm{eff}} = 1.0045 \pm 0.0012$. Using the information contained in the invisible width shifts the central value by -0.0001 with a small reduction of the error. Knowledge on ρ^{eff} can be improved if also the information from the hadronic decay widths is allowed to enter; this requires an external value for the strong coupling constant; if one uses the (optimistic, see section 9.2) world average value of the strong coupling constant, $\alpha_s = 0.118 \pm 0.003$, and measurements of the total hadronic decay width and of the decay width to b quarks, then the error goes down by $\sim$10 % only and the central value shifts by $+0.0008$. In view of this, it is certainly not necessary to introduce complications from QCD, and therefore here the value obtained only from the leptonic measurements is taken.

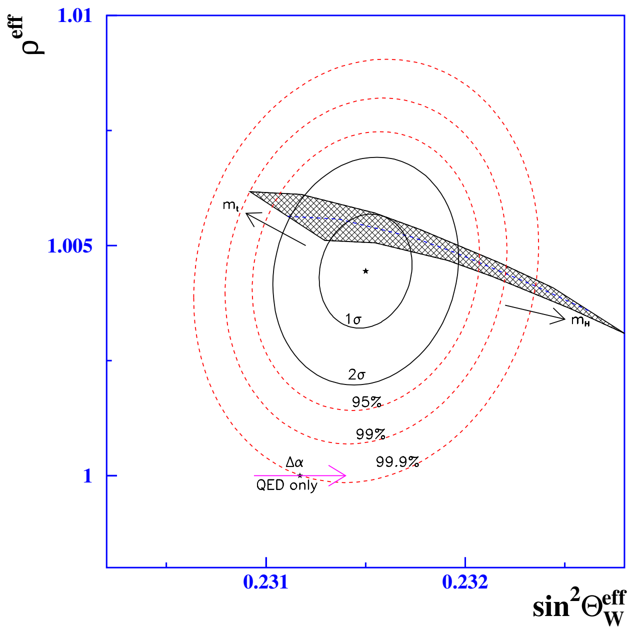

Figure 10.5: *Averages of measurements of the effective leptonic weak mixing angle at LEP/SLD and of the effective leptonic* ρ *parameter at LEP. See the text for an explanation of the figure.*

Contour lines from a fit of $\sin^2\theta_W^{\mathrm{eff},\ell}$ and ρ^{eff} to the leptonic and invisible Z widths and all asymmetry-type measurements are shown in Figure 10.5 . The star in the lower left corner shows the predicted value if only QED corrections from the photon vacuum polarisation are included, *i.e.* taking $(\rho^{\mathrm{eff}})^0 = 1$ and $(\sin^2\theta_W^{\mathrm{eff},\ell})^0$ according to equation 2.7 . This is disfavoured by the measurements at more than 99 % confidence level. The arrow indicates the change

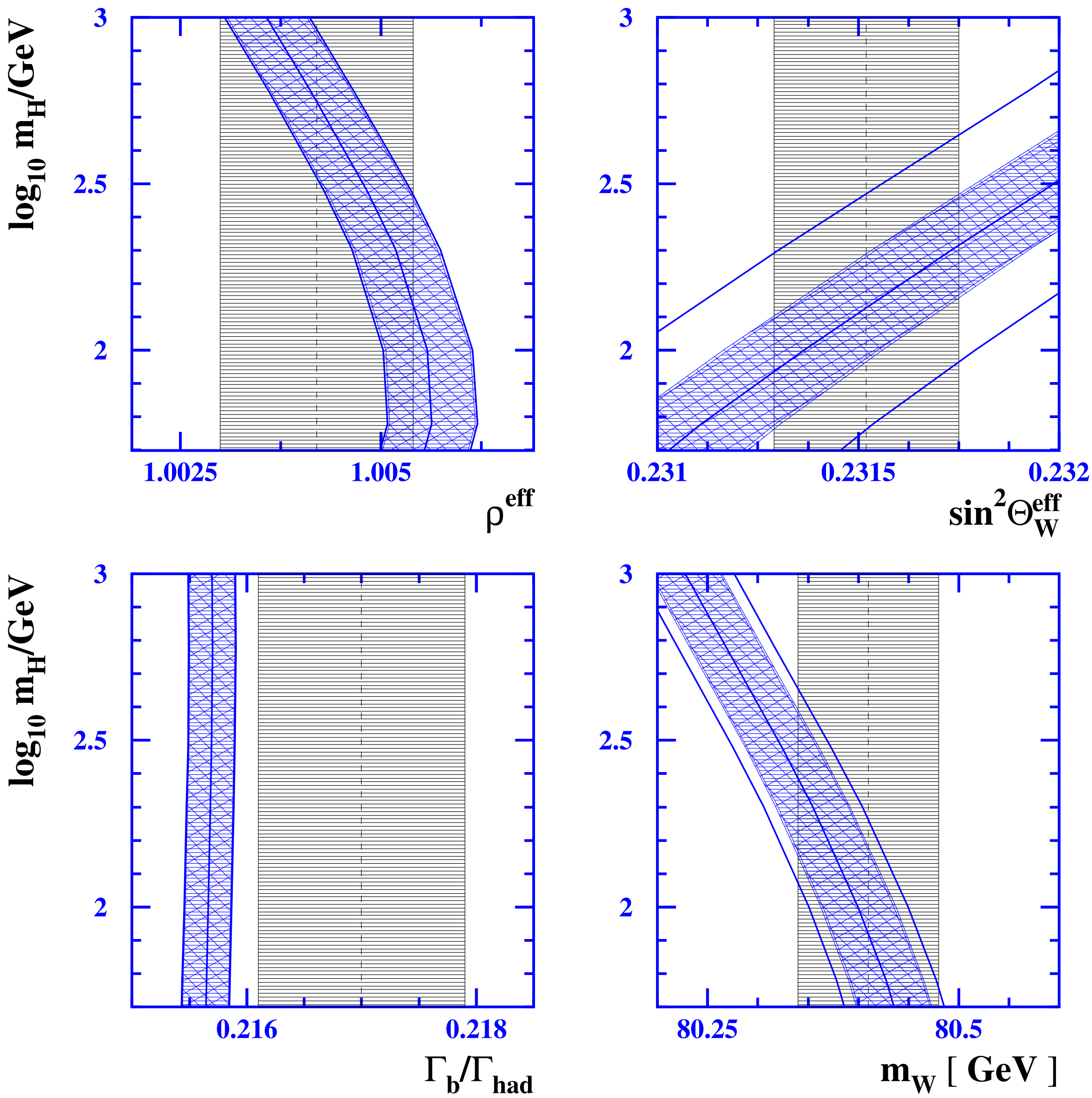

Figure 10.6: *Measurements of radiative electroweak corrections derived from the data by averaging appropriate classes of measurements.*

of this prediction if $\alpha(m_Z)$ is varied within its present errors.

Additional, genuine electroweak corrections are therefore necessary to describe the measurements, and indeed, the full Standard Model calculation agrees well with the measurements. The region allowed by the Standard Model is indicated by the hatched area shown in the figure, for a top quark mass of $m_t = 175.6 \pm 5.5$ GeV and a Higgs mass 75 GeV $< m_H <$ 1000 GeV. The influence of a variation of $\alpha(m_Z)$ is the same as indicated for the star in the lower left corner and not included in the hatched area.

10.3 Dependence of electroweak corrections on the Higgs mass

In order to illustrate the relevance of electroweak higher order effects to the determination of the Higgs boson mass it is interesting to average classes of measurements according to their dependence on electroweak corrections. ρ^{eff}, $R_b = \Gamma_{b\bar{b}}/\Gamma_h$, $\sin^2\theta_W^{\mathrm{eff}}$ and m_W depend on the radiative corrections summarised in the quantities $\Delta\rho^{\mathrm{eff}}$, δ_b, $\Delta\kappa$ and Δr_w, respectively, which were introduced in section 2.4 . These are shown in Figure 10.6 and compared with the Standard Model predictions as functions of the Higgs boson mass. The dark area on each plot indicates the change in the prediction if the top quark mass is varied within its present experimental error, and the light area shows the change with the electromagnetic coupling constant, $\alpha(m_Z)$. No theoretical errors on the predictions other than these parametric ones are included on the plots.

Some of the main features of each of the quantities shown on the plots of Figure 10.6 are worth pointing out:

- By definition, none of the four quantities shows a large dependence on the strong coupling constant. The determination of the strong coupling constant from the line shape measurements will be discussed in section 10.4.2 .
- Measurements contributing to the ρ^{eff} parameter, *i. e.* essentially only the measurements of the leptonic Z width at LEP I, depend mostly on the top quark mass and also show a weak dependence on the mass of the Higgs boson.
- Measurements of the ratio of the b decay width and the hadronic width determine the top quark mass via top-quark dependent vertex corrections to the b final state, since other corrections largely cancel in this ratio.
- The effective leptonic weak mixing angle is determined by asymmetry-type measurements. It is strongly affected by the error in the electromagnetic coupling constant, which contributes as much as the one in the measured top quark mass. $\sin^2\theta_{\mathrm{W}}^{\mathrm{eff}}$ is particularly sensitive to the Higgs boson mass.
- The W boson mass, from direct measurements or from the charged-to-neutral current ratio from neutrino scattering, offers good sensitivity to both the top quark and the Higgs boson masses without suffering from a prominent dependence on the value of the electromagnetic coupling constant.

In addition to parametric errors affecting the theoretical predictions, which are shown in the figure, there are genuine theoretical errors from missing higher orders in the calculations, which are not shown. These can be evaluated from information given in [17]; the relevant results are summarised in Table 10.2 below.

e.w. quantity	theoretical uncertainty
ρ^{eff}	± 0.0004
$\sin^2\theta_{\mathrm{W}}^{\mathrm{eff}}$	± 0.0001
R_{b}	± 0.0002
m_{W}	± 13 MeV

Table 10.2: *Estimated theoretical errors on electroweak radiative corrections.*

10.4 Electroweak fits

The following subsections present fits to the electroweak precision data based on theoretical calculations included in computer codes, namely BHM [23], TOPAZ0 [24] and ZFITTER [25]. These calculations have recently been compared and systematic errors from missing higher orders, different resummation techniques, scale dependencies and different factorisation schemes have been estimated [17]. They are represented by different "running options" implemented in these programs, which were varied in the fits presented below in order to evaluate the effects of theoretical uncertainties on the fitted parameters according to the recommendations described in the above reference. Since the comparison of different calculations was made, one of the programs (TOPAZ0) was updated to include non-factorisable QCD and electroweak corrections [20], resulting in a slightly higher value of the strong coupling constant derived from the LEP line shape data, which also gives rise to small changes in the derived Higgs boson and top quark masses.

The input data to the fits (see Table 10.1) also include the top quark mass and the electromagnetic coupling constant, and the only information on the strong coupling constant used is contained in the measurements of the hadronic line shape; therefore the resulting parametric uncertainties on the predicted values of observables are automatically included and properly propagated into the fit results.

10.4.1 Indirect determination of the top quark mass

In a first step, the consistency of all precision measurements with the direct measurements from the Tevatron are investigated. All observables from Table 10.1 except the direct top mass measurements are used. Since no precise information on the Higgs boson mass can be obtained that way, the Higgs mass was fixed at different values, whereas the Z mass, the top quark mass and the electromagnetic and strong coupling constants at the scale of the Z were allowed to vary. The resulting indirect measurement of the top quark mass obtained from χ^2 minimisation procedures are shown in Figure 10.7, expressed in terms of the change in χ^2 w.r.t. its minimum value. The curves shown refer to the "global χ^2" for m_{t}, *i. e.* at each value of m_{t} the χ^2 function is minimised by varying all other parameters, and the resulting value in $\Delta\chi^2$ is plotted in the figure.

The result of the fit is

$$m_{\mathrm{t\,indirect}} = (181 \pm 6 \pm 16_{\mathrm{Higgs}})\ \mathrm{GeV}\,.$$

The central value is quoted for a Higgs boson mass of 300 GeV, since this results in symmetric errors from the unknown Higgs boson mass. Differences between the three electroweak libraries considered are at most 0.3 GeV (between ZFITTER and TOPAZ0). The indirect result for the top quark mass agrees well with the average value from direct measurements at Fermilab, $m_{\mathrm{t\,direct}} = (175.6 \pm 5.5)$ GeV.

The Higgs boson mass can also be left as a free parameter in the fit; the average of the three calculations then becomes

$$m_{\mathrm{t\,indirect}} = (162^{+11}_{-8})\ \mathrm{GeV}\,.$$

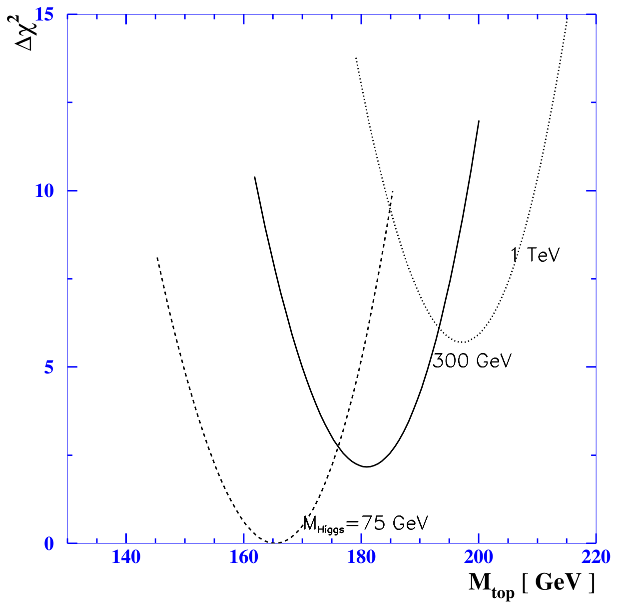

Figure 10.7: χ^2 *curves from fits of the top quark mass using all measurements of Table 10.1 except the direct measurement of the top quark mass.*

The value of the Higgs boson mass preferred by this fit is about 50 GeV, which is below the current lower limit on its mass of 77.5 GeV.

Contours of constant χ^2 from such fits are shown in Figure 10.8 . It is obvious that there is a large positive correlation between the top quark and the Higgs boson masses which amounts to approximately 70 %. The result of the direct measurements of the top quark mass and the lower limit on the Higgs boson mass are also indicated in the figure; the mass region preferred by these is well covered by the the 95 % confidence level contour from the fit. The one-sigma contours in the figure are shown for three different calculations and give an indication of the size of theoretical uncertainties.

The consistency between the value of the top mass from electroweak loops and the one from direct measurements shows that the dominant electroweak corrections within the Standard Model are due to the heavy top quark, as expected.

10.4.2 Fits with measured top quark mass

If the dominant corrections due to the heavy top quark are fixed by using the precise direct measurements of its mass in the fits, more precise information on the Higgs boson mass can be obtained. With all input data of Table 10.1 and m_Z, m_t, m_H, α_s and $\alpha(m_Z)$ as free parameters the results of Table 10.3 are obtained. The agreement of the measurements with the predictions at the best-fit point is illustrated in Figure 10.9, which shows the pull for each input quantity, *i. e.* the difference of the measured value and the prediction normalised to the experimental error. The combination of input measurements into separate averages is according to Figure 10.9, plus m_Z and $\alpha(m_Z)$, which are fit parameters and input at the same time; therefore, the number of degrees of freedom ("N_{df}") in the fit is 18. The dependence on the Higgs boson mass is logarithmic, and $\log_{10}(m_H/\mathrm{GeV})$ was therefore used as the parameter in all fits, which was converted to m_H in the table; the error in $\log_{10}(m_H/\mathrm{GeV})$ is nearly symmetric and ± 0.32 in size.

The most noticeable contribution to the overall χ^2 is caused by the disagreement between the weak mixing angle derived from the b quark forward-backward asymmetry measured at LEP and the left-right cross-section asymmetry

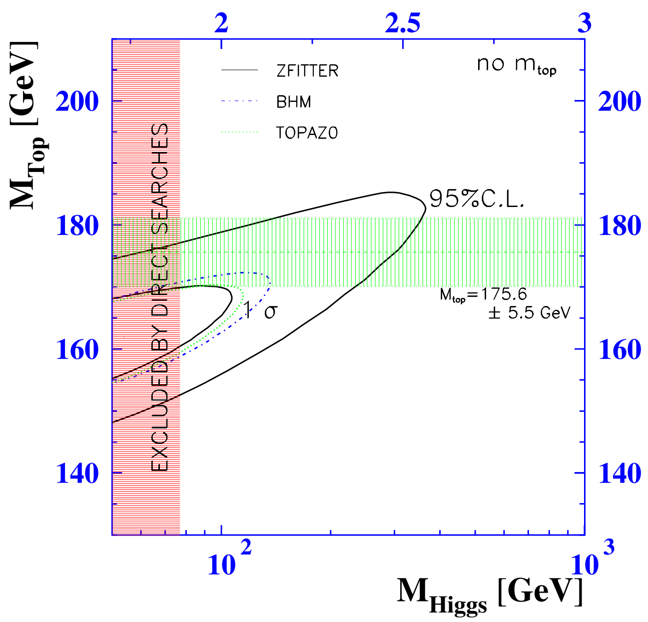

Figure 10.8: *Confidence level contours in the* m_H - m_t *plane.*

BHM $\chi^2/N_{df} = 19.0/18$, prob.=39%	
m_t [GeV]	173.6 ± 5.3
m_H [GeV]	$129\ ^{+120}_{-70}$
α_s	0.120 ± 0.003
TOPAZ0 $\chi^2/N_{df} = 19.7/18$, prob.=35%	
m_t [GeV]	173.4 ± 5.3
m_H [GeV]	$126 \pm\ ^{+120}_{-70}$
α_s	0.120 ± 0.003
ZFITTER $\chi^2/N_{df} = 19.5/18$, prob.=36%	
m_t [GeV]	173.2 ± 5.3
m_H [GeV]	$116\ ^{+120}_{-70}$
α_s	0.120 ± 0.003

Table 10.3: *Results from Standard Model fits to all input data of Table 10.1 using the computer codes BHM, TOPAZ0 and ZFITTER. No systematic errors due to missing higher orders in the calculations are given in the table, but are discussed in the text.*

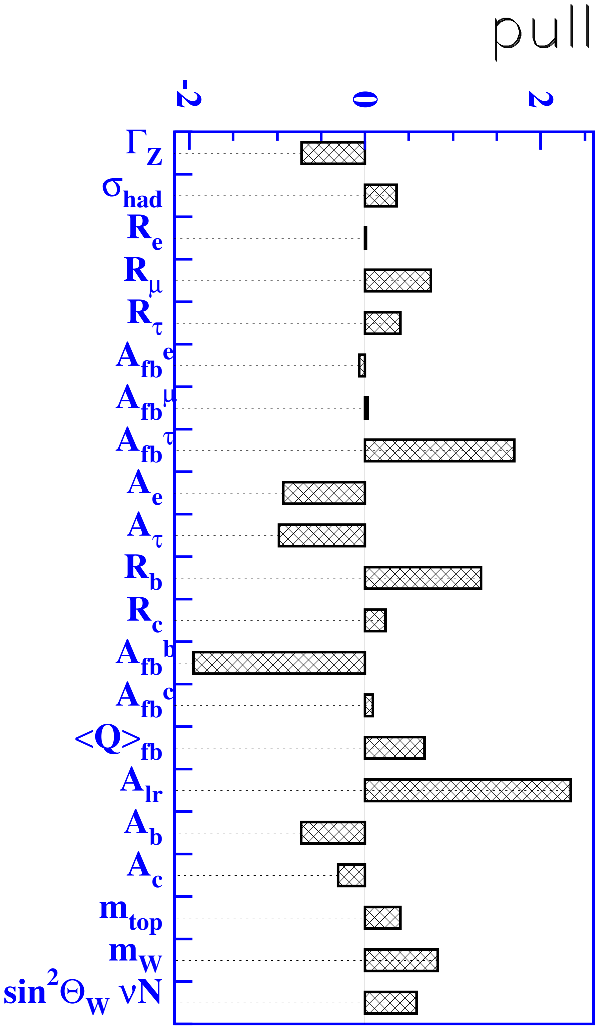

Figure 10.9: *Pull of the various observables w.r.t the best SM fit result of Table 10.3.*

from SLC, as already discussed in section 10.2. Still, the probability to get values of χ^2 larger than the ones given in the table is about 40 %.

It is interesting to note that the use of an external value of the strong coupling constant has a small effect on the resulting Higgs boson mass. If the optimistic world average value of the strong coupling constant as described in section 9.2 is used as an additional input to the fit, the resulting Higgs mass goes down by 7 GeV, and the error on $\log_{10}(m_{\mathrm{H}}/\mathrm{GeV})$ is 0.01 smaller. As expected, the result on the Higgs mass also changes visibly if the most recent evaluation of the electromagnetic coupling constant at the Z scale mentioned in section 9.1 is used, which depends heavily on non-perturbative QCD calculations [107]. With this value of the electromagnetic coupling, $\alpha(m_Z) = 1/(128.923 \pm 0.036)$, the fitted Higgs mass goes up by 15 GeV and the error on $\log_{10}(m_{\mathrm{H}}/\mathrm{GeV})$ goes down by 0.06. In order to separate electroweak physics from QCD these two options will not be considered any further; this is justifiable given the only moderate gains in precision.

The strong coupling constant

The information on α_s in Table 10.3 comes exclusively from the measurements of the hadronic line shape at LEP. A theoretically robust result is obtained by considering only the ratio of the hadronic and leptonic width, R_ℓ, since dependencies on Standard Model parameters like the top and Higgs masses cancel in the ratio. Possible contributions in the loops from particles not contained in the set of particles of the Standard Model may also be expected to cancel out. Using the full Standard Model calculations, as discussed above, the average value of the strong coupling constant for a Higgs boson mass of 300 GeV becomes $\alpha_s = 0.124 \pm 0.004$, where the largest difference among the three calculations of 0.0011 is between BHM and TOPAZ0; this indicates the size of theoretical uncertainties arising from electroweak corrections in the purely electroweak ratio of the hadronic and leptonic width in the absence of QCD corrections. The error in the electromagnetic coupling constant translates into a small error of ± 0.0007 on α_s. The effect of varying the Higgs mass between 75 and 1000 GeV is ± 0.002; other parametric uncertainties are negligible compared to this. Another important effect on the value of α_s is due to the factorisation scheme adopted when considering both pure QED and QCD final state corrections; these contribute an uncertainty of about ± 0.001. QCD uncertainties are dominated by the dependence on the renormalisation scale μ; a variation of $m_Z/4 < \mu < m_Z$ and other smaller contributions lead to a total estimated uncertainty of about ± 0.002 [19]. In summary, this leads to the result for the strong coupling constant from R_ℓ:

$$\begin{aligned} \alpha_s &= 0.124 \quad \pm 0.004 \\ &\qquad \pm 0.002_{ew} \pm 0.002_{Higgs} \pm 0.002_{QCD} \end{aligned}$$

Note that the above result has only a small dependence on the Standard Model of the electroweak interaction and can be considered as a conservative estimate.

The result on α_s from the fit of Table 10.3 to all input data is more precise, since here in addition to R_ℓ information on α_s from the hadronic width, from the hadronic pole cross-section and from the total width enters. The validity of the full Standard Model is assumed, resulting in a constrained value for the Higgs mass, which prefers a value lower than the 300 GeV taken above; this alone causes a difference in α_s of 0.001. The electroweak and QCD uncertainties are obviously the same as described above, leading to a total systematic error on α_s according to Table 10.3 of ± 0.003. Assuming the validity of the Standard Model and the preferred value of the Higgs boson mass as suggested by all electroweak precision data therefore results in

$$\alpha_s = 0.120 \pm 0.003 \pm 0.003_{\mathrm{theory}} = 0.120 \pm 0.004 .$$

Contour lines in the m_{H} vs. α_s plane are shown in Figure 10.10. Good agreement with the world average value of α_s, represented by the horizontal band, is seen. The systematic error discussed above is not included in the figure. The

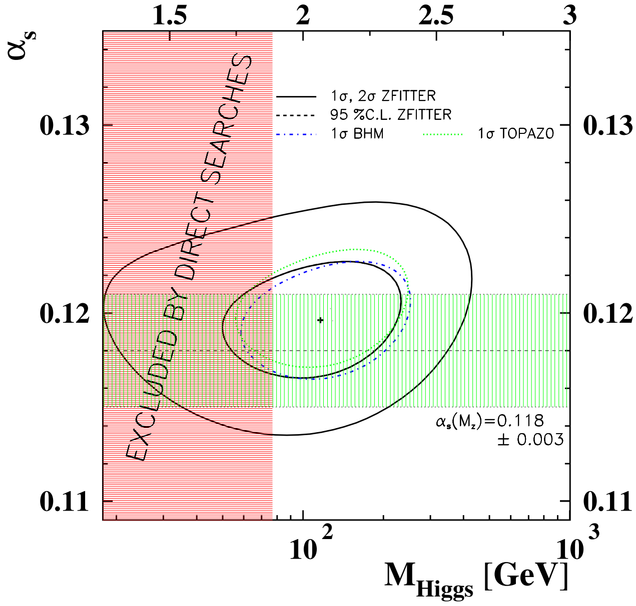

Figure 10.10: *Contours from fit to all electroweak observables in the plane of the Higgs mass vs. α_s. The deviations in the central values only partly reflect the total theoretical uncertainties, see the discussion in the text.*

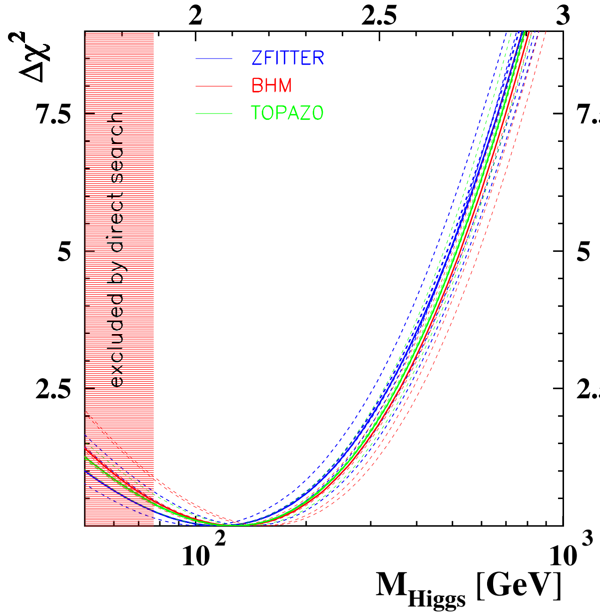

Figure 10.11: *χ^2 curves from fits for the Higgs mass to all electroweak measurements, with different codes (BHM,TOPAZ and ZFITTER) and running options.*

one-sigma contours are shown for each of the three electroweak libraries considered in Table 10.3 and show acceptable agreement compared with the size of the experimental errors.

Mass of the Higgs boson within the Standard Model

The value of the Higgs boson mass obtained from the full Standard Model fit of Table 10.3 deserves some further comments. The central values obtained by the different calculations differ slightly. Since the dependence of electroweak observables on the Higgs mass is only logarithmic, this is best expressed in terms of the difference in $\log_{10}(m_{\rm H}/\mathrm{GeV})$, which amounts to $\Delta\log_{10}(m_{\rm H}/\mathrm{GeV}) = 0.05$. Using the full set of variations in the calculations, as discussed above, leads to a larger error estimate. The running options implemented in each of the programs are changed one at a time, and the fit is repeated. Differences in the fitted Standard Model parameters are below ± 0.001 for α_s and below 0.4 GeV for $m_{\rm t}$, which is small compared with the errors from the fit. The differences are slightly more significant for the value of the Higgs mass.

The resulting global χ^2 curves for the Higgs boson mass are shown in Figure 10.11. The full lines represent the default running options preferred by the authors, whereas the dotted lines give the result obtained when options are changed one at a time from the default.

As can be seen from the figure, the default value of BHM represents well the central line; variations about this central line are approximately ± 0.1 in $\log_{10}(m_{\rm H}/\mathrm{GeV})$; this is considered as an estimate of the theoretical error on the Higgs boson mass, resulting in

$$\log_{10}(m_{\rm H}/\mathrm{GeV}) = 2.11^{+0.29}_{-0.34} \pm 0.1_{\rm theory} \quad \text{or}$$
$$m_{\rm H} = 130^{+130}_{-70}\ \mathrm{GeV}\,.$$

The lower limit on the Higgs boson mass of 77.5 GeV from searches for direct Higgs production is also indicated in the figure; together with the χ^2 curves from the indirect determination within the Standard Model this fixes an allowed region. Neglecting the lower bound and taking conservatively the χ^2 curve giving the largest value in Higgs mass results in a 95 % C.L. one-sided upper limit of $m_{\rm H} <$420 GeV. However, there certainly is some large probability from the indirect measurements alone for a Higgs mass in the region where it is already excluded by the direct searches. Following the prescription of the particle data group [120], values below the lower limit may be considered an unphysical region for the Higgs mass and the integration of probability is only performed beyond this point. In fact, the full likelihood function for the value of the Higgs mass around the lower limit has also been determined [117] and can be transformed into a χ^2 curve; this shows a steep fall at the point where the lower limit is set and is well approximated by a vertical line as suggested above. The 95 % C.L. one-sided upper limit obtained this way increases by 20 GeV and one obtains as a conservative upper limit on the Higgs boson mass

$$m_{\rm H} < 440\ \mathrm{GeV}\ @95\,\%\ \mathrm{C.L.}\,.$$

It is worth remarking that this limit has a strong dependence on individual measurements. This is particularly true for the left-right polarisation cross-section asymmetry, $A_{\rm lr}$, from SLC, which is the most precise among all determinations of the effective weak mixing angle. The $A_{\rm lr}$ measurement prefers a value of the Higgs boson mass that is far below the lower limit on the Higgs mass from direct searches (see Figure 10.4 in section 10.2). However, it is not justified to simply omit this measurement when averaging the determinations of the effective weak mixing angle, as already discussed above. On the other hand, there is a group of measurements preferring Higgs mass values around 1 TeV. Given the present experimental situation and the large uncertainties on the Higgs boson mass resulting from individual measurements the above limit should be taken with extreme care.

Very recent calculations including terms $O(G_F^2 m_t^2/m_W^2)$ [121] reduce the renormalisation scale and scheme dependence, and the theoretical uncertainty on the predicted Higgs boson mass will decrease once these will have been incorporated into the frames of the existing computer codes. The main effects on predicted Standard Model values of observables, for m_H=300 GeV, are a decrease of the $W^\pm$ mass by 15 MeV and an increase of the effective weak mixing angle by 0.0001 .

10.5 Future Expectations

The precision data collected around the Z resonance have now been fully analysed, although many results are still preliminary. Improved measurements of the effective weak mixing angle are expected from future running at the SLC, but, as has been pointed out in section 10.2, the impact of this on Standard Model parameters is limited by the precision of the electromagnetic coupling constant at the scale of the Z mass. The most significant progress will come from improved direct measurements of the top quark at the Tevatron and of the W boson mass at LEP II and the Tevatron. The present direct determinations of these masses are contrasted with the indirect determinations from all precision data of Table 10.1 except the top quark and W boson mass determinations (including the weak mixing angle from neutrino-nucleon scattering experiments). The result is obtained from a fit similar to the one described above, where the W boson mass replaces the Higgs mass as fit parameter. The predicted values of the top quark and W boson masses are summarised in Table 10.4; notice that this prediction of the W and top quark masses is only valid within the framework of the Standard Model.

The results are shown for the three different calculations already used above; their deviations only partly reflect the full theoretical uncertainty on m_W. If all options in the calculations are considered in addition to the deviations in the central value resulting from the default options, a conservative estimate of the theoretical error is obtained. Taking as the error the half-difference between the extreme results of the three codes considered results in

$$m_{W\ \mathrm{indirect}} = (80.325 \pm 0.041 \pm 0.013_{\mathrm{theory}})\ \mathrm{GeV}\,,$$
$$m_{t\ \mathrm{indirect}} = (157^{+11}_{-9} \pm 2_{\mathrm{theory}})\ \mathrm{GeV}\,.$$

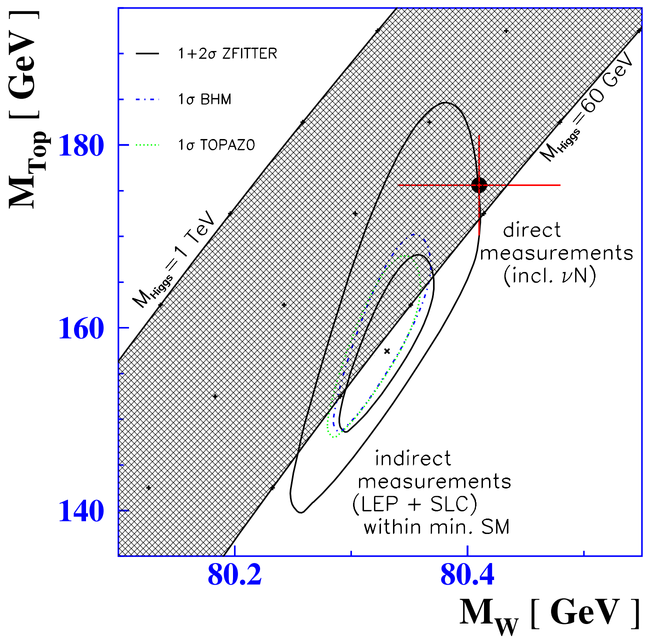

Figure 10.12: *Indirect measurements of the W and top masses compared with direct measurements.*

BHM	
m_t [GeV]	158^{+11}_{-9}
m_W [GeV]	80.328 ± 0.041
TOPAZ0	
m_t [GeV]	157^{+11}_{-9}
m_W [GeV]	80.322 ± 0.041
ZFITTER	
m_t [GeV]	158^{+11}_{-9}
m_W [GeV]	80.332 ± 0.041

Table 10.4: *Result from Standard Model fits to all input data of Table 10.1 except the top quark and W boson mass and the weak mixing angle from neutrino-nucleon scattering. Theoretical errors are not included, but are discussed in the text.*

The present results from direct measurements are

$$m_t = 175.6 \pm 5.5\ \mathrm{GeV}$$
$$m_W = 80.41 \pm 0.07\ \mathrm{GeV}\,.$$

The direct measurements shown in Figure 10.12 are at the two-σ boundary (corresponding to an 86.5 % C.L. contour) of the indirect results from the fit to the precision electroweak data. The level of agreement between the indirect determinations and the directly measured values of the W boson and top quark masses that will finally be observed provides a powerful test of the consistency and completeness of the Standard Model. The error on the top quark mass may come down by a factor two in future running at the Tevatron, and the W mass measurements from LEP II alone will ultimately reach a precision well below 0.05 GeV.

11 Summary

Electroweak precision measurements at LEP, SLC and the Tevatron have verified the tree level structure of the Standard Model with a precision below 10^{-3} and also demonstrated the existence of genuine electroweak corrections. Important improvements in our knowledge of Standard Model parameters were achieved: the number of particle generations, derived from the number of light neutrinos coupling to the Z, is three; the relative precision of the Z mass is as good as that of the Fermi constant; the strong coupling constant measured from the inclusive contribution of QCD diagrams to the hadronic width of the Z is one of the most precise determinations of this parameter and is in good agreement with other QCD studies. The agreement of the top quark mass predicted from virtual loops involving top with the directly measured value is a great success.

Precision results on the effective leptonic weak mixing angle pose one remaining - probably experimental - problem: the two most precise determinations from the left-right cross-section asymmetry at SLC and from the b quark forward-backward asymmetry at LEP disagree at the level of three standard deviations. Finalisation of all LEP results and future measurements at SLC will hopefully clarify this situation.

Together with the precisely measured top quark mass, electroweak precision data shed some light on the last secret of the Standard Model, the Higgs sector; the dependence of observables on the Higgs boson mass is logarithmic, and therefore only weak bounds on its mass can be derived at present. The preferred value of the Higgs mass from all precision measurements is around 130 GeV, whereas the lower bound on its mass from direct searches is 77.5 GeV. Altogether, this translates into a conservative upper limit on the Higgs mass of 440 GeV at 95 % confidence level.

Improvements in the imminent future will come from more precise measurements of the W boson mass at LEP and from future data taking at the Tevatron collider, which will also improve on the precision in the top quark mass. Also needed is a better value for the contribution of light quark loops to the running of the electroweak coupling constant; this requires new measurements of hadron production in e^+e^- collisions at low energies.

Finding the Higgs boson remains the most crucial task in particle physics. LEP II will finally reach energies up to 100 GeV per beam and this will allow searches for the Higgs bosons to be sensitive beyond 90 GeV. The future proton-proton collider, LHC at CERN, will cover all of the remaining range in Higgs boson mass and will be able to discover or to rule out a Standard Model Higgs boson. The actual value at which the Higgs boson is finally found will give an indication of the energy scale at which new physics must exist [122], motivated by arguments concerning vacuum stability or the scale at which the Higgs sector becomes strongly interacting. A Higgs boson more massive than $\sim$500 GeV necessarily requires an extension of the Standard Model at the scale of 1 TeV, whereas it remains internally consistent up to the grand unification scale (10^{16} GeV) if the Higgs boson mass lies between $\sim$100 and $\sim$200 GeV.

LHC also will also provide an enormous discovery potential for physics beyond the Standard Model. In particular sypersymmetric extensions are as well calculable as the Standard Model itself, leading to precise predictions of production cross sections for particles and decay chains. If super-symmetric particles exist at energies below $\sim$1 TeV, experiments at the LHC will be able to find and identify them. The list of other possible discoveries ranges from right-handed weak bosons over sub-structure of presently believed fundamental particles to the totally unexpected. Before LHC comes into operation, precision measurements confronted with the Standard Model of the electromagnetic, weak and strong interaction will remain our only way to probe this energy range.

ACKNOWLEDGEMENTS

I am grateful to the members of the LEP accelerator group and of the four LEP collaborations, and particularly to my colleagues from the OPAL and ALEPH experiments, for helpful discussions and advice in preparing this review. I also wish to thank my colleagues from the "Working group on LEP energy" and from the "LEP electroweak working group" for fruitful collaboration over many years. Special thanks go to A. Feig, H.-G. Sander and I. Giehl for careful proof-reading of the manuscript and many helpful comments. The high energy physics group of the Institut für Physik at the Johannes Gutenberg-Universität Mainz deserves credit for providing a pleasant and efficient working environment, concerning both computational infrastructure and scientific inspiration.

Günter Quast, January 1998

List of Tables

List of Figures

Bibliography

[1] Gargamelle collaboration, F.J. Hasert *et al.*, Phys. Lett. **B46** (1973) 121; 138.

[2] S.L. Glashow, Nucl. Phys. **22** (1961) 579;
S. Weinberg, Phys. Rev. Lett. **19** (1967) 19;
A. Salam, in: N. Svartholm (ed.), *Proc. of the Eighth Nobel Symposium*, Almqvist and Wiksell, Stockholm; Wiley, New York (1968) 367;
S.L. Glashow, J. Iliopoulos and L. Maiani, Phys. Rev. **D6** (1970) 1285;
C. Bouchiat, J. Iliopoulos and P. Meyer, Phys. Lett. **B38** (1972) 519.

[3] C.Y. Prescott *et al.*, Phys. Lett. **B77** (1978) 347; **B84** (1979) 524.

[4] JADE Collaboration, W. Bartel *et al.*, Phys. Lett. **B101** (1981) 361; Phys. Lett. **B108** (1982) 140;
Mark J Collaboration, D. Barber *et al.*, Phys. Rev. Lett. **46** (1981) 1663;
TASSO Collaboration, R. Brandelik *et al.*, Phys. Lett. **B117** (1982) 365;
CELLO Collaboration, H.J. Behrend *et al.*, Z. Phys. **C16** (1983) 301.

[5] MARK II Collaboration, M.E. Levi *et al.*, Phys. Rev. Lett. **51** (1983) 1941;
HRS Collaboration, D. Bender *et al.*, Phys. Rev. **D30** (1984) 515;
MAC Collaboration, W.W. Ash *et al.*, Phys. Rev. Lett. **55** (1985) 1831.

[6] The UA1 collaboration, G. Arnison *et al.*, Phys. Lett. **B122** (1983) 103; **126B** (1983) 398;
The UA2 collaboration, G. Banner *et al.*, Phys. Lett. **B122** (1983) 476; **129B** (1983) 130.

[7] R. Erickson, (ed.), *SLC DESIGN HANDBOOK*, SLAC (Dec 1986);
B. Richter (SLAC) *SLC STATUS AND SLAC FUTURE PLANS*, Invited talk given at 14th Int. Conf. on High Energy Accelerators, Tsukuba, Japan, (Aug. 1989), SLAC-PUB-5075 and Part. Accel. **26** 33;
SLD and SLC Collaborations, M. Breidenbach for the collaboration, *SLC AND SLD: EXPERIMENTAL EXPERIENCE WITH A LINEAR COLLIDER*, SLAC-PUB-6313 (Aug 1993), presented at 2nd International Workshop on Physics and Experiments with Linear e^+e^- Colliders, Waikoloa, Waikoloa Linear Collid. (1993);
M. Woods, AIP conference Proceedings **343**, (1995) 230.

[8] *LEP Design Report*, CERN-LEP/84-01, June 1984;
The main features of LEP have been reviewed by: S. Myers and E. Picasso, Contemp. Phys. **31** (1990) 387.

[9] ALEPH Collaboration, D. Decamp *et al.*, Nucl. Inst. Meth. A294 (1990) 121;
ALEPH Collaboration, D. Buskulic et al., *Performance of the ALEPH Detector at LEP*, Nucl. Inst. Meth. **A360** (1995) 481-506;
Construction ond Performance of the new ALEPH Vertex Detector, Proceedings of the 5th International Conference on Advanced Technology and Particle Physics, Como, Italy, 7-11 Oct 1996;
The ALEPH Handbook 95, Vol. 1 and 2, available from the ALEPH Secretariat, CERN.

[10] DELPHI Collaboration, P. Aarnio *et al.*, Nucl. Inst. Meth. **A303** (1991) 233;
DELPHI Collaboration, P. Abreu *et al.*, *Performance of the DELPHI Detector* Nucl. Inst. Meth. **A378** (1996) 57-100.

[11] OPAL Collaboration, K. Ahmet *et al.*, Nucl. Inst. Meth. A305 (1991) 275;
P. Allport *et al.*, Nucl. Inst. Meth. **A324** (1993) 34;
P. Allport *et al.*, Nucl. Inst. Meth. **A346** (1994) 476;
B.E. Anderson *et al.*, IEEE Trans. Nucl. Sci **41** (1994) 845.

[12] L3 Collaboration, B. Adeva *et al.*, Nucl. Inst. Meth. **A289** (1990) 35;
M. Acciarri *et al.*, Nucl. Inst. Meth **A351** (1994) 300;
M. Chemarin *et al.*, Nucl. Inst. Meth **A349** (1994) 345;
A. Adam *et al.*, Nucl. Inst. Meth **A383** (1996) 342;
I.C. Brock *et al.*, Nucl. Inst. Meth. **A381** (1996) 236.

[13] CDF Collaboration, F. Abe *et al.*, Phys. Rev. Lett. **73** (1994) 225;
CDF Collaboration, F. Abe *et al.*, Phys. Rev. Lett. **74** (1995) 2626;
DØ Collaboration, S. Abachi *et al.*, Phys. Rev. Lett. **74** (1995) 2632.

[14] Particle Data Group, R.M. Barnett *et al.*, Phys. Rev. **D54** (1996) 1.

[15] CDF Collaboration, J. Lys, and DØ Collaboration, S. Protopopescu, talks presented at ICHEP96, Warsaw (July 1996), to appear in the proceedings;
J. Konigsberg, *Top results from CDF*, M. Strovink, *Top results from DØ* and A. Yagil, *Top physics*, talks presented at EPS-HEP-97, Jerusalem (Aug. 1997), to appear in the proceedings.

[16] S. Jadach *et al.*, *Z Physics at LEP1*, CERN 89-08, ed. G. Altarelli *et al.*, Vol. 1–3 (1989) and references therein.

[17] *Reports of the working group on precision calculations for the Z resonance*, eds. D. Bardin, W. Hollik and G. Passarino, CERN Yellow Report 95-03, Geneva, 31 March 1995, and references therein.

[18] F.A. Berends *et al.*, *Z Physics at LEP1*, CERN 89-08, ed. G. Altarelli *et al.*, Vol. 1 (1989) 89;
M. Böhm *et al.*, *Z Physics at LEP1*, CERN 89-08, ed. G. Altarelli *et al.*, Vol. 1 (1989) 203;
D. Bardin *et al.*, QED corrections Phys. **B351** (1991) 1;
S. Jadach, M. Skrzypek and M. Martinez, Phys. Lett. **B280** (1992) 129;
see also reference [17].

[19] T. Hebbeker, M. Martinez, G. Passarino and G. Quast, Phys. Lett. **B331** (1994) 165, and references therein.

[20] A. Czarnecki and J.H. Kühn, *Nonfactorizable QCD and Electroweak Corrections to the Hadronic Z Boson Decay Rate*, hep-ph/9608366 preprint, (Aug. 1996).

[21] see *e. g.* F.A. Berends *et al.*, *Proceedings of the Workshop on Z physics at LEP I*, CERN Report 89-08 Vol. 1, 89;
G. Burgers, W. Hollik and M. Martinez, M. Consoli, W. Hollik and F. Jegerlehner, the same proceedings, 7;
G. Burgers, F. Jegerlehner, B. Kniehl and J. Kühn, the same proceedings, 55.

[22] S. Eidelmann and F. Jegerlehner, Z. Phys. **C67** (1995) 585.

[23] see [21];
W. Hollik, Fortsch. Phys. **38** (1990) 3;
recently updated with results summarized in [17].

[24] G. Montagna, O. Nicrosini, G. Passarino, F. Piccinni and R. Pittau, Nucl. Phys. **B401** (1993) 3;
Comp. Phys. Comm. **76** (1993) 328;
recently updated with results from [17] and [20].

[25] D. Bardin *et al.*, Z. Phys. **C44** (1989) 493; Comp. Phys. Comm. **59** (1990) 303; Nucl. Phys. **B351** (1991) 1; Phys. Lett. **B255** (1991) 290 and CERN-TH 6443/92 (May1992);
recently updated with results summarized in [17].

[26] The working group on LEP energy, R. Billen *et al.*, *Calibration of Centre-of-Mass Energies at LEP1 for Precise Measurements of Z properties*, to be published in Z. Phys. **C**.

[27] The working group on LEP energy, L. Arnaudon *et al.*, *The Energy Calibration of LEP in 1992*, CERN SL/93-21 (DI), April 1993;
L. Arnaudon *et al.*, *Accurate determination of the LEP beam Energy by resonant depolarization*, Z. Phys. **C66** (1995) 45-62;
The working goup on LEP energy, R. Assmann *et al.*, *The energy calibration of LEP in the 1993 scan*, Z. Phys. **C66** (1995) 567-582;
a very complete description is A. Drees, *High Precision Measurements of the LEP Center-of-Mass Energies during the 1993 and 1995 Z Resonance Scans*, PhD thesis, Univ. Wuppertal, Germany, WUB-DIS 97-5 (1997).

[28] L. Arnaudon *et al.*, *Measurement of the LEP beam energy by resonant spin depolarisation*, Phys. Lett. **B284** (1992) 431-493;
L. Arnaudon *et al.*, *Accurate Determination of the LEP Beam Energy by Resonant Depolarization*, Z. Phys. **C66** (1995) 45-62.

[29] L. Knudsen *et al.*, Phys. Lett. **B270** (1991) 97.

[30] M. Placidi and M. Rossmanith, Nucl. Inst. Meth. **A274** (1989) 79.

[31] The working group on LEP energy and the Collaborations ALEPH, DELPHI, L3 and OPAL, *Measurement of the mass of the Z boson and the energy calibration of LEP*, Phys. Lett. **B307** (1993) 187–193.

[32] G. Quast, *Recent Results from LEP*, Mod. Phys. Lett. **A8** (1993) 675-695.

[33] A.A. Sokolov and I.M. Ternov, *On Polarization and Spin Effects in the Theory of Synchrotron Radiation*, Sov. Phys. Dokl. **8** (1964) 1203.

[34] L. Arnaudon *et al.*, *Effects of Terrestrial Tides on the LEP Beam Energy*, Nucl. Inst. Meth. **A357** (1995) 249-252.

[35] DELPHI internal note *DELSIM*, 87-96/PROG 99 and 87-98/PROG 100 (1989);
J. Allison *et al.*, *The Detector Simulation Program for the OPAL experiment at LEP*, Nucl. Inst. Meth. **A317** (1991);
the simulations are all based on [36]; more details may be found in the references on the detectors, [9], [10] and [12].

[36] R. Brun *et al.*, *GEANT 3*, CERN Report DD/EE/84-1 (Revised), 1987.

[37] *FORTRAN program JETSET*, see reference [48];
FORTRAN program HERWIG, see reference [49];
FORTRAN program KORALZ, see reference [50];
FORTRAN program ALIBABA,see reference [53];
FORTRAN program BABAMC, M. Böhm, A. Denner and W. Hollik, Nucl. Phys. **B304** (1988) 687;
F. A. Berends, R Kleiss, W. Hollik, Nucl. Phys. **B304** (1988) 712;
FORTRAN program UNIBAB, see reference [54];
FORTRAN program BHLUMI, see reference [46].

[38] OPAL Collaboration, G. Alexander *et al.*, Z. Phys. **C52** (1991) 175;
OPAL Collaboration, P.D. Acton *et al.*, Z. Phys. **C58** (1993) 219;
OPAL Collaboration, R. Akers *et al.*, Z. Phys. **C61** (1994) 19;
OPAL Collaboration, *The Preliminary OPAL SiW luminosity analysis: Results for the 1994 Summer conferences*, OPAL Physics Note PN142, July 1994;
OPAL Collaboration, *A Preliminary Update of the Z Line Shape and Lepton Asymmetry Measurements with the 1993 and 1994 data*, OPAL Physics Note PN166, Feb. 1995;
OPAL Collaboration, *A preliminary update of the Z Line Shape and Lepton Asymmetry Measurements with a Revised 1993-1994 LEP Energy and 1995 Lepton Asymmetry*, OPAL Physics Note PN242, July 1996;
OPAL Collaboration, *Measurements of Lepton Pair Asymmetries using the 1995 Data*, contributed paper to ICHEP96, Warsaw (July 1996) **PA07-015**;
OPAL Collaboration, *A Preliminary Update of Z Line Shape and Lepton Asymmetry Measurements with the 1995 Data, OPAL Physics Note PN286, March 1997.*

[39] A. Leike, T. Riemann, J. Rose, Phys. Lett. **B273** (1991) 513;
T. Riemann, Phys. Lett. **B293** (1992) 451;
S. Krisch, T. Riemann, Comp. Phys. Comm. **88** (1995) 89.

[40] The TOPAZ Collaboration, K. Miyabayashi *et al.*, Phys. Lett **B347** (1995) 171.

[41] S. Jadach *et al.*, *Z Physics at LEP1*, CERN 89-08, eds. G. Altarelli *et al.*, Vol. 1 (1989) 235.

[42] see references [110, 111, 112].

[43] CDHS Collaboration, H. Abramowicz *et al.*, Phys. Rev. Lett. **57** (1986) 298 and A. Blondel *et al.*, Z. Phys. **C45** (1990) 361;
CHARM Collaboration, J.V. Allaby *et al.*, Phys. Lett. **B177** (1986) 446 and Z. Phys. **C36** (1987) 611;
CCFR Collaboration, K. McFarland *et al.*, *A precision measurement of Electroweak Parameters in Neutrino-Nucleon Scattering*, FNAL-Pub-97/001-E (1997).

[44] The LEP Collaborations, the LEP Electroweak Working Group and the SLD Heavy Flavour Group, *A Combination of Preliminary Electroweak Measurements and Constraints on the Standard Model*, contributed paper to EPS-HEP-97, Jerusalem (Aug. 1997), available on the Internet via http://www.cern.ch/LEPEWWG .

[45] The LEP Collaborations ALEPH, DELPHI, L3, OPAL and the LEP Electroweak Working Group, *A Combination of Preliminary LEP Electroweak Measurements and Constraints on the Standard Model*, CERN-PPE/97-154.

[46] *FORTRAN program BHLUMI*, S. Jadach et al., Comp. Phys. Comm. **70** (1992) 305;
S. Jadach *et al.*, *Reports of the working group on precision calculations for the Z resonance*, eds. D. Bardin, W. Hollik and G. Passarino, CERN Yellow Report 95-03, Geneva, (31 March 1995) 343;
S. Jadach *et al.*, Phys. Lett **B353** (1995) 326;
S. Jadach *et al.*, Phys. Lett **B353** (1995) 349.

[47] S. Jadach, E. Richter-Wąs, Z. Wąs and B.F.L. Ward, Phys. Lett. **B268** (1991) 253;
W. Beenakker and B. Pietrzyk, Phys. Lett. **B304** (1993) 366;
S. Jadach *et al.*, Phys. Lett **B353** (1995) 362.

[48] *FORTRAN program JETSET*, T. Sjöstrand, Comp. Phys. Comm. **39** (1986) 347;
T. Sjöstrand, Comp. Phys. Comm. **82** (1994) 74.

[49] *FORTRAN program HERWIG*, G. Marchesini and B.R. Webber, Nucl. Phys. **B310** (1988) 461;
G. Marchesini *et al.*, Comp. Phys. Comm. **67** (1992) 465.

[50] S. Jadach, B.F.L. Ward, Z. Wąs, Comp. Phys. Comm. **66** (1991) 276; **79** (1994) 503;
S. Jadach, Z. Wąs, R. Decker, M. Jeżabek, J.H. Kühn, Comp. Phys. Comm. **76** (1993) 361.

[51] DELPHI Collaboration, P. Aarnio *et al.*, Nucl. Phys. **B367** (1991) 511;
DELPHI Collaboration, P. Abreu *et al.*, Nucl. Phys. **B417** (1994) 3;
DELPHI Collaboration, P. Abreu *et al.*, Nucl. Phys. **B418** (1994) 403;
DELPHI Collaboration, DELPHI Note 95-62 PHYS 497, July 1995;
DELPHI Collaboration, DELPHI Note 96-118 CONF 65, contributed paper to ICHEP96, Warsaw (July 1996) **PA07-001**;
DELPHI Collaboration, contributed paper to EPS-HEP-97, Jerusalm (Aug. 1997) **EPS 463**.

[52] W. Beenakker and G. Passarino, *Large-Angle Bhabha Scattering at LEP 1*, to be published in Phys. Lett. **B**.

[53] *FORTRAN program ALIBABA*, W. Beenakker et al., Nucl. Phys. **B349** (1991) 323 and Phys. Lett. **B251** (1990) 299.

[54] *FORTRAN program UNIBAB*, H. Anlauf, P. Manakos, T. Ohl, T. Mannel, H. Meinhard, H.D. Dahmen, Comp. Phys. Comm. **79** (1994) 466.

[55] L3 Collaboration, B. Adeva *et al.*, Z. Phys. **C51** (1991) 179;
L3 Collaboration, O. Adriani *et al.*, Phys. Rep. **236** (1993) 1;
L3 Collaboration, M. Acciarri *et al.*, Z. Phys. **C62** (1994) 551;
L3 Collaboration, *Preliminary L3 Results on Electroweak Parameters using 1990-96 Data*, L3 Note 2065, March 1997, available on the Internet via http://hpl3sn02.cern.ch/note/note-2065.ps.gz.

[56] M. Martinez, L. Garrido, R. Miquel, J.L. Harton and R. Tanaka, Z. Phys. **C49** (1991) 645;
M. Martinez and F. Teubert, Z. Phys. **C65** (1995) 267;
recently updated with results summarized in [17].

[57] ALEPH Collaboration, D. Decamp *et al.*, Z. Phys. **C48** (1990) 365;
ALEPH Collaboration, D. Decamp *et al.*, Z. Phys. **C53** (1992) 1;
ALEPH Collaboration, D. Buskulic *et al.*, Z. Phys. **C60** (1993) 71;
ALEPH Collaboration, D. Buskulic *et al.*, Z. Phys. **C62** (1994) 539;
ALEPH Collaboration, *Preliminary Results on Z Production Cross Section and Lepton Forward-Backward Asymmetries using the 1990-1995 Data*, contributed paper to ICHEP96, Warsaw (July 1996) **PA07-069**, updated for EPS-HEP-97, Jerusalem (Aug. 1997).

[58] G. Quast, *Updated Z Parameters and Standard Model fits*, talk presented at EPS-HEP-97 (PA 107), Jerusalem (Aug. 1997), to appear in the proceedings.

[59] C. Paus from L3 collaboration, private communication (Aug. 1997).

[60] ALEPH Collaboration, D. Busculic *et al.*, Phys. Lett. **B378** (1996) 373;
ALEPH Collaboration, contributed paper to EPS-HEP-97, Jerusalem (Aug. 1997) **EPS 602**.

[61] DELPHI Collaboration, DELPHI 97-132 CONF 110, (July 1997).

[62] L3 Collaboration, M. Acciarri *et al.*, Phys. Lett. **B370** (1996) 195;
L3 Collaboration, M. Acciarri *et al.*, CERN-PPE/97-052;
L3 Collaboration, L3 Note 2163 (Sept. 1997).

[63] OPAL Collaboration, G. Alexander *et al.*, CERN-PPE/97-101;
OPAL Collaboration, Physics note PN-319 (Sept. 1997).

[64] P. Ward, *Fermion pair production above the Z and limits on New Physics*, talk presented at EPS-HEP-97 (PA 112), Jerusalem (Aug. 1997), to appear in the proceedings;
see also [45].

[65] A. Olchevsky, *Proceedings of the International Europhysics Conference on High Energy Physics*, EPS-HEP-95, Brussels (July 1995) 905.

[66] ALEPH Collaboration, D. Decamp *et al.*, Phys. Lett. **B259** (1991) 377;
ALEPH Collaboration, D. Buskulic *et al.*, *Determination of* $\sin^2\theta_W^{\rm eff}$ *Using Jet Charge Measurements in Hadronic Z Decays*, Z. Phys. **C71** (1996) 357.

[67] DELPHI Collaboration, P. Abreu *et al.*, Phys. Lett. **B277** (1992) 371;
DELPHI Collaboration, *Measurement of the Inclusive Charge Flow in Hadronic Z Decays,* DELPHI 96-19 PHYS 594.

[68] L3 Collaboration, *Forward-backward charge asymmetry measurement on 91-94 data*, L3 Note 2063 (1996).

[69] OPAL Collaboration, P.D. Acton *et al.*, Phys. Lett. **B294** (1992) 436;
OPAL Collaboration, OPAL Physics Note PN195 (1995).

[70] ALEPH Collaboration, D. Buskulic *et al.*, Z. Phys. **C69** (1996) 183.

[71] DELPHI Collaboration, P. Abreu *et al.*, Z. Phys. **C67** (1995) 183;
DELPHI Collaboration, *An updated measurement of* τ *polarisation*, DELPHI 96-114 CONF 42, contributed paper to ICHEP96, Warsaw (July 1996) **PA07-008**.

[72] L3 Collaboration, O. Acciari *et al.*, Phys. Lett. **B341** (1994) 245;
L3 Collaboration, *Measurement of the* τ *Polarization and the Spin Correlations in* $e^+e^- \to \tau^+\tau^-$, L3 note 2131, contributed paper to EPS-HEP-97, Jerusalem (Aug. 1997) **EPS-481**.

[73] OPAL Collaboration, G. Alexander *et al.*, *A Precise Measurement of the Tau Polarization and its Forward-Backward Asymmetry at LEP*, CERN-PPE/96-078, subm. Z. Phys. **C**.

[74] SLD Collaboration, K. Abe *et al.*, Phys. Rev. Lett. **73** (1994) 25;
SLD Collaboration, K. Abe *et al.*, Phys. Rev. Lett. **74** (1995) 2880;
SLD Collaboration, K. Abe *et al.*, Phys. Rev. Lett. **78** (1997) 2075;
SLD Collaboration, K. Abe *et al.*, Phys. Rev. Lett. **79** (1997) 804;
P. Rowson, talk presented at "Rencontre de Moriond", Moriond, France, (March 1997).

[75] CHARM II Collaboration, P. Vilain *et al.*, Phys. Lett. **B335** (1994) 246.

[76] T. Behnke, D.G. Charlton, *Electroweak Measurements using heavy quarks at LEP*, Phys. Scr. **52** (1995) 133-157.

[77] ALEPH Collaboration, D. Buskulic *et al.*, Z. Phys. **C62** (1994) 179;
ALEPH Collaboration, *Measurement of the b forward-backward asymmetries and of the* $\bar{\chi}$ *mixing parameter using high-*p_t *leptons,* contributed paper to ICHEP96, Warsaw (July 1996) **PA10-002**, CERN-PPE/96-072;
ALEPH Collaboration., D. Buskulic *et al.*, *Measurement of the semileptonic b branching ratios from inclusive leptons in Z decays*, contributed Paper to EPS-HEP-95 Brussels (July 1995) **EPS0404**.

[78] DELPHI Collaboration, P. Abreu et al., Z. Phys. **C66** (1995) 323;
DELPHI Collaboration, *Measurement of semileptonic branching ratios and* $\bar{\chi}_{\rm b}$ *from inclusive leptons in Z decays*, contributed paper to EPS-HEP-97, Jerusalem (Aug. 1997), **EPS-415**.

[79] L3 Collaboration, O. Adriani *et al.*, Phys. Lett. **B292** (1992) 454;
L3 Collaboration, M. Acciarri *et al.*, Phys. Lett. **B335** (1994) 542;
L3 Collaboration, *Measurement of* $R_{\rm b}$ *and BR*$({\rm b} \to \ell X)$ *from b-quark semileptonic decays,* L3 Note 1449, (1993);
L3 Collaboration, *L3 Results on* $A_{\rm fb}^{\rm b\bar{b}}$, $A_{\rm fb}^{\rm c\bar{c}}$*and* χ *for the Glasgow Conference,* L3 Note 1624 (1994);
L3 Collaboration, *L3 Results on* $R_{\rm b}$ *and* ${\rm BR}({\rm b} \to \ell)$ *for the Glasgow Conference,* L3 Note 1625 (1994);
L3 Collaboration, M. Acciarri *et al.*, Z. Phys. **C71** (1996) 379;
L3 Collaboration, *Measurement of the* $e^+e^- \to Z \to b\overline{b}$ *Forward-Backward Asymmetry Using Leptons, L3 Note 2112, contributed paper to EPS-HEP-97, Jerusalem (Aug. 1997)* **EPS-490**;
L3 Collaboration, *Measurement of the* ${\rm B}^0 - \bar{\rm B}^0$ *Mixing Parameter*, Note 2113, contributed paper to EPS-HEP-97, Jerusalem (Aug. 1997) **EPS-490**.

[80] OPAL Collaboration, R. Akers *et al.*, Z. Phys. **C60** (1993) 199;
OPAL Collaboration, *Updated Measurement of the Heavy Quark Forward-Backward Asymmetries and Average B Mixing Using Leptons in Multihadronic Events*, OPAL Physics Note PN226, contributed paper to ICHEP96, Warsaw (July 1996) **PA05-007**;
OPAL Collaboration, G. Alexander *et al.*, Z. Phys. **C70** (1996) 357.

[81] The LEP Experiments, *Combining Heavy Flavour Electroweak Measurements at LEP*, Nucl. Inst. Meth. **A378** (1996) 101.

[82] L3 Collaboration, O. Adriani *et al.*, Phys. Lett **B307** (1993) 237.

[83] ALEPH Collaboration, *Measurement of the partial decay width of the Z into* $c\bar{c}$ *quarks* , contributed paper to ICHEP96, Warsaw (July 1996) **PA10-016** ;
ALEPH Collaboration, *Study of Charmed Hadron Production in Z Decays*, contributed paper to EPS-HEP-97, Jerusalem (Aug. 1997), **EPS-623** .

[84] DELPHI Collaboration, *Summary of* $R_{\rm c}$ *measurements in DELPHI*, contributed paper to ICHEP96, Warsaw (July 1996) **PA01-060**.

[85] OPAL Collaboration, G. Alexander *et al.*, Z. Phys. **C72** (1996) 1;
OPAL Collaboration, K. Ackerstaff *et al.*, CERN-PPE/97-93, subm. Z. Phys. **C**.

[86] ALEPH Collaboration, D. Buskulic *et al.*, Z. Phys. **C62** (1994) 1;
ALEPH Collaboration, D. Buskulic *et al.*, *The Forward–Backward Asymmetry for Charm Quarks at the Z pole: an Update*, contributed Paper to EPS-HEP-95 Brussels (July 1995) **EPS0634**.

[87] OPAL Collaboration, G. Alexander *et al.*, Z. Phys. **C73** (1997) 379.

[88] ALEPH Collaboration, R. Barate *et al.*, Phys. Lett. **B401** (1997) 150;
ALEPH Collaboration, R. Barate *et al.*, Phys. Lett. **B401** (1997) 163.

[89] DELPHI Collaboration, *Measurement of the partial decay width* ${R_{\rm b}}^0 = \Gamma_{\rm b\bar{b}}/\Gamma_{\rm h}$ *with the DELPHI detector at LEP*, contributed paper to EPS-HEP-97 Jerusalem (Aug. 1997) **EPS-419**.

[90] L3 Collaboration, *Measurement of the Z Branching fraction into Bottom Quarks Using Doulbe Tag Methods*, contributed paper to EPS-HEP-97 Jerusalem (Aug. 1997), **EPS-489**.

[91] OPAL Collaboration, K. Ackerstaff *et al.*, Z. Phys. **C74** (1997) 1.

[92] SLD Collaboration, K. Abe *et al.*, Phys. Rev. **D53** (1996) 1023;
SLD Collaboration, K. Abe *et al.*, SLAC-PUB-7481, (Aug 1997), subm. Phys. Rev. Lett;
SLD Collaboration, contributed paper to EPS-HEP-97, Jerusalem (Aug. 1997) **EPS-118**.

[93] DELPHI Collaboration, P. Abreu *et al.*, Z. Phys **C65** (1995) 569;
DELPHI Collaboration, P. Abreu *et al.*, Z. Phys **C66** (1995) 341;
DELPHI Collaboration, *Measurement of the Forward-Backward Asymmetries of* $e^+e^- \to Z \to b\overline{b}$ *and* $e^+e^- \to Z \to c\overline{c}$, contributed Paper to EPS-HEP-95 Brussels (July 1995) **EPS0571**.

[94] L3 Collaboration, $A^{\rm b}_{\rm fb}$ *using a jet-charge technique on 1994 data*, L3 Note 2129.

[95] OPAL Collaboration, R. Akers *et al.*, Z. Phys. **C67** (1995) 365;
OPAL Collaboration, *Measurement of the b quark forward-backward asymmetry around the Z peak unsing jet charge and vertex charge*, CERN-PPE/97-06.

[96] G. Altarelli and B. Lampe, Nucl. Phys. **B391** (1993) 3;
B. Lampe, *A note on QCD corrections to* A^b_{FB} *using thrust to determine the b-quark direction*, MPI-Ph/93-74;
A. Djouadi, B. Lampe and P.M. Zerwas, Z. Phys. **C67** (1995) 123.

[97] The LEP Heavy Flavour Group, *QCD corrections to* $A^{\rm b}_{\rm fb}$ *and* $A^{\rm c}_{\rm fb}$ *at LEP I*, LEPHF/97-01, (Aug 1997), available on the Internet via http://www.cern.ch/LEPEWWG .

[98] The LEP heavy flavour group, *Presentation of LEP Electroweak Heavy Flavour Results for Summer 1996 Conferences*, LEPHF/96-01, available on the Internet via http://www.cern.ch/LEPEWWG .

[99] SLD Collaboration, contributed paper to EPS-HEP-97, Jerusalem (Aug. 1997) **EPS-120**.

[100] SLD Collaboration, K. Abe *et al.*, Phys. Rev. Lett. **74** (1995) 2890 and 2895;
SLD Collaboration, K. Abe *et al.*, Phys. Rev. Lett. **75** (1995) 3609;
SLD Collaboration, contributed papers to EPS-HEP-97, Jerusalem (Aug. 1997) **EPS-122**;**EPS-123**;**EPS-124**;**EPS-126**;
E. Etzion, talk presented at EPS-HEP-97, Jerusalem (Aug. 1997), to appear in the proceedings.

[101] M.L. Swartz, *Reevaluation of the Hadronic Contribution to* $\alpha(M_Z^2)$, SLAC-PUB-6710, November 1994; SLAC-PUB-95-7001, September 1995.

[102] A.D. Martin and D. Zeppenfeld, Phys. Lett. **B345** (1994) 558.

[103] H. Burkhardt and B. Pietrzyk, Phys. Lett. **B356** (1995) 398.

[104] H. Burkhardt, F. Jegerlehner, G. Penso and C. Verzegnassi, Z. Phys. **C43** (1989) 497.

[105] R. Alemany, M. Davier and A. H"øcker, Report LAL 97-02(1997).

[106] N.V. Krasnikov, Mod. Phys. Lett. **A9** (1994) 2825;
N.V. Krasnikov and R. Rodenberg, *Update of the electromagnetic effective coupling constant* $\alpha(m_Z^2)$, PITHA 97/45 and preprint hep-ph/9711367 (Nov. 1997).

[107] M. Davier and A. H"øcker, *Improved Dermination of* $\alpha(m_Z^2)$ *and the Anomalous Magnetic Moment of the Muon*, Report LAL 97-85 (1997), subm. Phys. Lett. **B**.

[108] M. Schmelling, Proc. 28th International Conference on High Energy Physics, Warsaw (July 1996);
S. Catani, talk at EPS-HEP-97, Jerusalem (Aug. 1997), to appear in the proceedings;
S. Bethke, Proceedings of the QCD '97 Conference, Montpellier, France.

[109] UA2 Collaboration, J. Alitti *et al.*, Phys. Lett. **B276** (1992) 354.

[110] CDF Collaboration, F. Abe *et al.*, Phys. Rev. Lett. **75** (1995) 1017;
CDF Collaboration, F. Abe *et al.*, Phys. Rev. Lett. **78** (1997) 4536.

[111] DØ Collaboration, S. Abachi *et al.*, Phys. Rev. Lett. **75** (1995) 1023;
DØ Collaboration, S. Abachi *et al.*, Phys. Rev. Lett. **75** (1995) 1034;
DØ Collaboration, S. Abachi *et al.*, Phys. Rev. Lett. **77** (1996) 3303;
DØ Collaboration, S. Abachi *et al.*, Phys. Rev. Lett. **78** (1997) 3634;
DØ Collaboration, S. Abachi *et al.*, Fermilab-Pub-97/088-E, subm. Phys. Rev. **D**;
DØ Collaboration, S. Abbott *et al.*, Fermilab-Pub-97/136-E, subm. Phys. Rev. Lett.

[112] ALEPH Collaboration, contributed paper to EPS-HEP-97, Jerusalem (Aug. 1997) **EPS/97-601**;
DELPHI Collaboration, contributed paper to EPS-HEP-97, Jerusalem (Aug. 1997) **EPS/97-295**;
L3 Collaboration, M. Acciarri *et al.*, Phys. Lett. **B398** (1997) 223 and CERN-PPE/97-98, subm. Phys. Lett. **B**;
OPAL Collaboration, K. Ackerstaff *et al.*, Phys. Lett. **B397** (1997) 147 and paper in preparation, to be subm. Z. Phys. **C** .

[113] W. Beenacker and F.A. Berends (conveners) *et al.*, *Physics at LEP 2*, ed. G. Altarelli *et al.*, CERN 96-01, Vol. 1.

[114] A. Blondel, private communication (Aug. 1997) and reference [44].

[115] ALEPH Collaboration, R. Barate *et al.*, Phys. Lett. **B384** (1996) 427;
DELPHI Collaboration, P. Abreu *et al.*, Nucl. Phys. **B421** (1994) 3;
L3 Collaboration, M. Acciarri *et al.*, Phys. Lett. **B385** (1996) 454;
OPAL Collaboration, G. Alexander *et al.*, Z. Phys. **C73** (1997) 189.

[116] ALEPH Collaboration, R. Barate *et al.*, CERN-PPE/97-070, subm. Phys. Lett. **B**;
DELPHI Collaboration, P. Abreu *et al.*, CERN-PPE/97-85, subm. Z. Phys. **C**;
L3 Collaboration, M. Acciarri *et al.*, CERN-PPE/97-81, subm. Phys. Lett. **B**;
OPAL Collaboration, K. Ackerstaff *et al.*, CERN-PPE/97-115, subm. Z. Phys. **C**.

[117] see [123];
LEP working group for Higgs boson searches, CERN/LEPC 97-11.

[118] J. Wess, B. Zumino, Nucl. Phys. **B70** (1974) 39;
H.P. Nilles, Phys. Rep. **110** (1984) 1;
H.E. Haber, G.L. Kane, Phys. Rep. **117** (1985) 75.

[119] see reference [123] and LEP SUSY working group, *Preliminary results from the combination of LEP experiments*, available on the Internet via http://www.cern.ch/lepsusy .

[120] Particle Data Group, R.M. Barnett *et al.*, Phys. Rev. **D54** (1996) 165.

[121] G. Degrassi, P. Gambino and A. Vicini, Phys. Lett. **B383** (1996) 219;
G. Degrassi, P. Gambino and A. Sirlin, Phys. Lett. **B394** (1997) 188;
G. Degrassi, P. Gambino, M. Passere and A. Sirlin, *The Role of* m_{W} *in Precision Studies of the Standard Model*, CERN-TH-97-197.

[122] M. Carena and P.M. Zerwas (conveners), *Higgs Physics*, ed. G. Altarelli *et al.*, CERN 96-01, Vol. 1. (1996) 358.

[123] P. Janot, *Searches for New Particles*, talk presented at EPS-HEP-97, Jerusalem (Aug. 1997), to appear in the proceedings.

*

[*] References to conference contributions and internal notes of experiments refer to preliminary material.